Spin dynamics in GaN- and InGaAs-based semiconductor structures

Cong Tu Nguyen

Cong Tu Nguyen. Spin dynamics in GaN- and InGaAs-based semiconductor structures. Micro and nanotechnologies/Microelectronics. INSA de Toulouse, 2014. English. NNT : 2014ISAT0006 . tel-01222170

THÈSE

En vue de l'obtention du

DOCTORAT DE L'UNIVERSITÉ DE TOULOUSE

Délivré par : *l'Institut National des Sciences Appliquées de Toulouse (INSA de Toulouse)*

Présentée et soutenue le *11/04/2014* **par :**

Cong Tu NGUYEN

Spin dynamics in GaN- and InGaAs-based semiconductor structures

---

JURY

Vinh LE THANH	Professeur d'Université	Rapporteur
Mathieu GALLART	Maître de conférences, HDR	Rapporteur
Jean Christophe HARMAND	Directeur de Recherche	Examinateur
Chantal FONTAINE	Directeur de Recherche	Examinateur
Thierry AMAND	Directeur de Recherche	Directeur de thèse
Andrea BALOCCHI	Maître de conférences	Co-Directeur de thèse

École doctorale et spécialité :
GEET : Photonique et Systèmes Optoélectroniques
Unité de Recherche :
Laboratoire de Physique et Chimie de Nano-Objets, INSA-CNRS-UPS, UMR 5215
Directeur(s) de Thèse :
Thierry AMAND et *Andrea BALOCCHI*
Rapporteurs :
Vinh LE THANH et *Mathieu GALLART*

Résumé de Thèse

Spécialité: Photonique et Systèmes Optoélectroniques

Nom: NGUYEN

Prenom: Cong Tu,

INSA de Toulouse, Génie Physique , Laboratoire de Physique et Chimie des nano-objets ,

Titre anglais: Spin dynamics in GaN- and InGaAs-based semiconductor structures

Résumé en Anglais :

This thesis work is a contribution to the investigation by photoluminescence spectroscopy of the spin properties of III-V semiconductors with possible applications to the emerging semiconductor spintronics field. Two approaches have been explored in this work to achieve a long and robust spin polarization: i) Spatial confinement of the carriers in 0D nanostructured systems (quantum dots). ii) Defect engineering of paramagnetic centres in a bulk systems.

Concerning the first approach, we have investigated the polarization properties of excitons in nanowire-embedded GaN/AlN quantum dots. We first evidence a low temperature sizeable linear polarization degree of the photoluminescence (~15 %) under quasi-resonant excitation with no temporal decay during the exciton lifetime. Moreover, we demonstrate that this stable exciton spin polarization is unaffected by the temperature up to 300 K. A detailed theoretical model based on the density matrix approach has also been developed to account for the observed polarization degree and its angular dependence.

Regarding the second approach, we have demonstrated a proof-of-concept of conduction band spin-filtering device based on the implantation of paramagnetic centres in InGaAs epilayers. The principle relies on the creation of Ga interstitial defects as previously demonstrated in our group in dilute nitride GaAsN compounds. The driving force behind this work has been to overcome the limitations inherent to the introduction of N in the compounds: a) The dependence of the photoluminescence energy on the spin-filtering efficiency. b) The lack of spatial patterning of the active regions.

In this work we show how the spin-filtering defects can be created by ion implantation creating a chosen density and spatial distribution of gallium paramagnetic centers in N-free epilayers. We demonstrate by photoluminescence spectroscopy that spin-dependent recombination (SDR) ratios as high as 240 % can be achieved in the implanted areas. The optimum implantation conditions for the most efficient SDR are also determined by the systematic analysis of different ion doses spanning four orders of magnitude. We finally show how the application of a weak external magnetic field leads to a sizable enhancement of the SDR ratio from the spin polarization of the implanted nuclei.

Titre français: Dynamique de spin dans des structures semiconductrices
à base de GaN et de InGaAs

Résumé en Français:

Ce travail de thèse est une contribution à l'étude de la dynamique de spin des porteurs dans des structures semiconductrices III-V en vue d'applications possibles dans le domaine émergent de la spintronique dans les semiconducteurs. Deux approches différentes on été envisagées afin de pouvoir obtenir une polarisation en spin des porteurs longue et robuste : i) le confinement spatial dans des nano-structures 0D (boîtes quantiques), ii) l'ingénierie des centres paramagnétiques dans des couches massives.

Pour la première approche, nous avons étudié les propriétés de polarisation de spin d'excitons confinés dans des boîtes quantiques de GaN/AlN insérées dans des nano-fils. Nous avons d'abord mis en évidence un taux important de polarisation de la photoluminescence (15 %) à basse température sous excitation quasi-résonante et nous avons démontré que cette polarisation est temporellement constante pendant la durée de vie des excitons. Grâce à des mesures en température, nous avons aussi démontré que cette polarisation n'est aucunement affectée jusqu'à 300 K. Nous avons aussi développé un modèle détaillé basé sur la matrice densité pour décrire le dégré de polarisation de la photoluminescence et sa dépendance angulaire.

Pour la deuxième approche, nous avons réalisé un dispositif prototype de filtrage de spin basé sur l'implantation de centres paramagnétiques dans des couches massives de InGaAs. Le principe repose sur la création de défauts interstitiels paramagnétiques comme précédemment démontré dans notre groupe pour les nitrures dilués tels que GaAsN. Le but de ce travail a été le développement d'un procédé de création de ces défauts qui puisse surmonter les inconvénients liés à l'insertion de l'azote dans les semiconducteurs de type GaAs : a) la dépendance de l'efficacité du filtrage de spin avec de l'énergie de photoluminescence, b) l'impossibilité de créer des zones actives avec des motifs spécifiques.

Dans ce travail, nous démontrons que des régions actives de filtre à spin peuvent être créées par implantation ionique de défauts paramagnétiques avec une densité et des motifs spatiaux prédéfinis. Grâce à des études par photoluminescence, nous avons d'une part mis en évidence des taux de recombinaison dépendant en spin pouvant aller jusqu'à 240 % dans les zones implantées. D'autre part, nous avons déterminé la dose d'implantation la plus favorable grâce à une étude systématique sur différents échantillons implantés avec des densités ioniques étendues sur quatre ordres de grandeurs. Nous avons également observé que l'application d'un champ magnétique externe produit une augmentation significative du taux de recombinaison dépendant en spin due à la polarisation en spin des noyaux implantés.

Acknowledgments

After three years of my Ph.D. thesis in Toulouse it is time to conclude that the success of my thesis can not be associated to an individual person. I am very grateful for any support both in word and in deed from everybody who has contributed to my thesis directly and indirectly.

First and foremost, my sincere gratitude to my supervisor Dr. Thierry AMAND, Prof. Xavier MARIE, Prof. PHI Hoa Binh who gave me a chance to practice in and let me accomplish my Ph.D. in quantum optoelectronic group, LPCNO, INSA de Toulouse. Thierry always has good ideas to explain, sometimes entirely new, physical effects. He showed me once again, that one has understood well any physics only when one can explain it the easiest way. I am grateful for a great number of his inputs on results interpretation in general, and this thesis, in particular.

I would like to express my special thanks of gratitude to Dr. Andréa BALOCCHI, my co-supervisor, for his engagement and ambitious experimental ideas that has pushed me forward. With his comprehensive experimental knowledge, he guided me to the successful accomplishment of my thesis. Even in such cases where the difficult problems appeared to be impossible to be solved his advices always helped and motivated to keep trying. I am very grateful for Adrea's support both in research concerning my Ph.D. and in usual life. He helped me a lot in resolving of number of administrative tasks and setting up my new life when I had just arrived in Toulouse.

I wish to thank Delphine LAGARDE, Tiantian ZHANG for three successful years worked together in the lab and for their support. We spent together as well the hard time including non-stop experiments lasting for several weeks, auguring time as more entertaining time.

I would like to thank Philippe BARATE, Simone MAZZUCATO stepping in my path for their inputs. They integrated fast and actively supported me a lot.

I would like also to thank and acknowledge all members of the group "Optoelectronique Quantique" for the professional working atmosphere: DUONG Quang Ha, Héllene CARRERE, Piere RENUCCI, Bernhard URBASZEK, Grégory SALLEN, Sergej KUNZ, Louis BOUET, Maël VIDAL, Gang WANG.

I wish to thank Prof. Vinh LE THANH, Dr. Mathieu GALLART for their willingness to be reporting referees and to co-examining my Ph.D. defense. Also I would like to thank Madame Chantal FONTAINE and Dr. Jean-Christophe HARMAND for being a part of my thesis commission and for co-examining my Ph.D. defense.

I would like also to acknowledge all members of the LPCNO laboratory for a lovely working atmosphere: Mme. Michèle FORTUNÉ, Mr. Francis CHOUZENOUX, Mme. Lise ARNOULD, Mme. Elisabeth LANCE ...

I owe many thanks and appreciation to all my friends for their help and for the unforgettable time we shared together.

Finally, I would like to express my deepest gratitude to my family, especially my parents: NGUYEN Cong Tuan and NGUYEN Thi Hien. It was a very difficult and hard time at the beginning; I could not overcome this without their love and permanent support. I would like to dedicate all my success and lucky to my beloved parents!

Contents

Introduction **1**

1 Introduction to the electronic and optical properties of III-V semiconductors **3**

1.1 Introduction to the electronic properties of semiconductors: from bulk to quantum dots . . . 5
  1.1.1 Bulk semiconductor . . . 5
    1.1.1.1 Crystal structure . . . 5
    1.1.1.2 Band structure . . . 6
    1.1.1.3 The Exciton . . . 8
  1.1.2 Semiconductor heterostructures . . . 13
    1.1.2.1 Quantum Wells . . . 14
    1.1.2.2 Quantum Dot . . . 15
1.2 Optical orientation in semiconductors . . . 16
  1.2.1 Optical transitions and selection rules . . . 17
  1.2.2 3D structures . . . 18
  1.2.3 2D structures . . . 22
  1.2.4 0D structures . . . 23
1.3 Spin relaxation mechanisms . . . 24
  1.3.1 Elliott-Yafet mechanism . . . 24
  1.3.2 D'yakonov-Perel mechanism . . . 24
  1.3.3 Bir-Aronov-Pikus mechanism . . . 26
  1.3.4 Hyperfine-interaction mechanism . . . 27
  1.3.5 Exciton's spin relaxation mechanism . . . 27
Bibliography . . . 31

2 Experimental set-ups **35**

2.1 Time resolved photoluminescence spectroscopy . . . 37
  2.1.1 Excitation source . . . 37
  2.1.2 Frequency doubling and tripling . . . 40

- 2.1.3 Streak camera detection 42
- 2.1.4 Spectral and temporal resolution 44
- 2.1.5 Polarisation resolution 45
- 2.1.6 Cooling system 46
- 2.2 Stationary Photoluminescence set-up 47
- 2.3 Magnetic fields 47
- Bibliography 49

3 Spin dynamics in nanowire-embedded GaN quantum dots 51

- 3.1 Introduction 53
  - 3.1.1 Wide bandgap semiconductor (In)GaN 53
  - 3.1.2 GaN nanowires 53
- 3.2 Spin properties of GaN based structures: state of the arts 55
  - 3.2.1 Bulk GaN 55
  - 3.2.2 Nanostructured GaN 56
- 3.3 Spin dynamics of nanowire-embedded GaN quantum dots 60
  - 3.3.1 Sample and experimental configuration 60
  - 3.3.2 Exciton photoluminescence polarisation of GaN/AlN nanowire QDs: spectral dependence 62
  - 3.3.3 Exciton photoluminescence polarisation of GaN/AlN nanowire QDs: angular dependence 65
    - 3.3.3.1 Experiment A 66
    - 3.3.3.2 Experiment B 68
  - 3.3.4 Exciton photoluminescence polarisation of GaN/AlN nanowire QDs: dynamics 69
    - 3.3.4.1 Non depolarisation 69
    - 3.3.4.2 Temperature insensitivity 70
  - 3.3.5 Theoretical model 72
    - 3.3.5.1 Experiment A 72
    - 3.3.5.2 Experiment B 76
- 3.4 Conclusion 78
- Bibliography 79

4 Spin-dependent recombination effect in Ga implanted InGaAs 85

- 4.1 Spin dependent recombination effect 87
  - 4.1.1 The Spin dependent recombination mechanism 87
  - 4.1.2 Manifestation of Spin Dependent Recombination in (In)GaAsN 90
    - 4.1.2.1 The enhancement of PL Intensity and carrier life time 90

        4.1.2.2 Spin filtering effect 91
        4.1.2.3 Power dependence 92
    4.1.3 Origin of the deep paramagnetic centres 93
4.2 Ion implanted semiconductor InGaAs for SDR-based devices 94
    4.2.1 Why ion implanted InGaAs 94
    4.2.2 Sample 95
4.3 Spin dynamics of InGaAs ion implanted 95
    4.3.1 Evidence of the Spin Dependent Recombination 98
    4.3.2 Ion implantation dose dependence 100
    4.3.3 Magnetic field effects 101
4.4 Conclusion 103
Bibliography 105

Conclusions **109**

Résumé de la thèse en français **111**

List of Figures

1.1 *The zincblende (a) and wurtzite (b) crystal structures [1, 7].* 6

1.2 *Schematic of the band structure at the* Γ *point for ZB and WZ crystals with and without the inclusion of the spin-orbit interaction and, for the WZ structure, the crystal field [7].* 8

1.3 *The variation of the band gap energy versus lattice constant for some common semiconductors at room temperature [2].* 10

1.4 *The exciton binding energies versus band gap for common semiconductors at room temperature [21].* 11

1.5 *The electron-hole pair in (a) the two particle picture and (b) the exciton picture.* 12

1.6 *Schematics and energy diagram of (a) a quantum well and (b) a quantum dot heterostructures.* 14

1.7 *The principle of the optical orientation method. Carriers with a definite spin are excited with polarised light. The analysis of the emitted ligh polarisation is then used to extract the carrier spin properties.* . . . 17

1.8 *The selection rules of the electronic transitions at* $\vec{k} = 0$ *under circular excitation* $\sigma^{\pm}$ *of (a) ZB and (b) WZ bulk semiconductors. The values in the parentheses show the relative intensity of the corresponding transitions. The states in the valence band are presented in the hole formalism.* 20

1.9 *The selection rules of the excitonic transitions at* $\vec{k} = 0$ *corresponding to the circular excitation of bulk WZ semiconductors. The excitation light propagates along the c axis. For the sake of simplicity, we have assumed* $|R_+\rangle = -|X + iY\rangle/\sqrt{2}, |R_-\rangle = |X - iY\rangle/\sqrt{2}$ *and* $\alpha^2 \gg \beta^2$. 21

1.10 *The selection rules at* $\vec{k} = 0$ *in quantum wells corresponding to (a) circular and (b) linear excitations.* 22

1.11 *The selection rules at* $\vec{k} = 0$ *corresponding to (a) an ideal and (b) an asymmetric and/or strained quantum dot.* 23

1.12 *Sketch of the conduction band spin splitting induced by the spin-orbit coupling in a bulk semiconductor.* 25

1.13 *Sketch of the Dyakonov-Perel mechanism [26].* 26

1.14 *Schematic representation of the different spin relaxation processes occurring for a heavy exciton.* τ_e, τ_h *and* τ_{exc} *are the corresponding relaxation times of the electron spin, the hole spin and the heavy-hole exciton spin.* 29

2.1 *The time- and polarisation-resolved photoluminescence setup.* 38

2.2 *The layout of the* $Nd{:}YVO_4$ *laser head optical cavity [4].* 38

2.3 *Ti:Sapphire characteristics: (a) Energy level structure of the* Ti^{3+} *vibrational levels; (b) Absorption and emission spectra of Ti:sapphire* [3]. 39

2.4 *(a) The schematic set-up of the Flexible Harmonic Generator used to double/triple the Ti:sapphire fundamental frequency. (b) The schematic representation of the frequency doubling using the LBO crystal and (c) of the frequency tripling using the BBO crystal.* 42

2.5 *(a) Operating Principle of a Streak Camera (b) Sweeping mechanism responsible for the time resolution.* 43

2.6 *Example of a streak camera image on time range 4 measured with a 80 grooves/mm grating.* 44

2.7 *Spectral sensitivity of different streak tubes.* 45

3.1 *(a) Schematic illustration of typical GaN/AlN inclusions on the top of a GaN nanowire grown on Si (111) substrate. The broken white lines schematically represent the propagation of substrate-induced defects which can relax through the nanowire surface before the dots are grown. (b) HRTEM image of a single GaN/AlN inclusion. The GaN "quantum dot" embedded in nanowire has a disk-like shape* ∼ *1 nm thick and* ∼ *30 nm wide surrounded by an AlN matrix [29].* 54

3.2 *(a) Schematic illustration of the Si (grey) and GaN (black) lattices in the coincidence orientation [55]. (b) Temperature dependence of the photoluminescence decay time and integrated intensity as afunciton of the temperature for an ensemble of GaN/AlN nanowire-embedded quatum dots [28].* 55

3.3 *Temperature dependence of the electron spin relaxation time in (a) wurtzite GaN. The different symbols indicates the spin relaxation time measured with and without an external magnetic field in Voigt geometry. The different values are due to the anisotropic nature of the Dyakonv-Perel spin relaxation mechanism intrinsic to the wurtzite structure [11]. (b) Cubic GaN [12]. The horizontal line corresponds to the calculated electron spin relaxation time based on the Dyakonv-Perel mechanism.* 57

3.4 *The temperature dependence of the PL linear polarisation dynamics measured after a quasi-resonant linear excitation for (a) Zinc-blende GaN/AlN quantum dots [18]; (b) Wurtzite InGaN/GaN quantum dots embedded in a p-i-n structure [19]; (c) Zinc-blende InAs/GaAS quantum dots [46]. (d) Temperature dependence of the spin lifetimes in InGaN/GaN nanodisks [42].* 59

3.5 *(a) Schematic representation of a single nanowire. (b) Top view SEM image of the nanowires. The white dashed circles highlight some of the coalesced nanowires.* 60

3.6 *The time integrated photoluminescence spectrum of the sample under non-resonant excitation. The arrows indicate schematically the condition of quasi-resonant excitation used in this work.* 61

3.7 *Schematic representation of (a) the sample orientation and (b) the relation between frame* $(\vec{e}(\alpha), \vec{e}_{\perp}(\alpha))$ *and frame* $(\vec{e}_X, \vec{e}_Y)$. $\vec{e}_X$, $\vec{e}_Y$ *and* $\vec{e}_Z$ *are respectively taken parallel to the* $[11\bar{2}0]$, $[1\bar{1}00]$ *and* $[0001]$ *crystal directions.* 62

3.8 *The co-* (I^X) *and cross-polarised* (I^Y) *time integrated PL intensities (solid lines) under a* π^X *quasi-resonant excitation* (E_{exc}*=4.24 eV) at T=300 K and the corresponding PL linear polarisation degree (green circles) in both (a) and (b). (a) The orange squares reproduce the PL linear polarisation degrees measured for a higher excitation energy,* E_{exc}*=4.33 eV. (b) The grey downward triangles show the linear polarisation measured with a rotation angle* $\alpha = 45^o$ *of the detection frame. The pink upward triangles reproduce the linear polarisation measured in the same detection frame* ($\alpha = 0^o$) *but under circularly polarised excitation in quasi-resonant conditions. The superscripts in* $I^{X/Y}$ ($I^{X'/Y'}$) *indicate the polarisation directions of the PL intensities used to calculate the PL linear polarisation degree.* 63

3.9 *(a) The co- (I^X) and cross-polarised (I^Y) time integrated PL intensities (solid lines) under a linearly polarised (π^X) quasi-resonant excitation (E_{exc}= 4.36 eV - λ_{exc} = 284 nm) at T= 4 K and the corresponding PL linear polarisation degree (orange circles). (b) The co- (I^X) and cross-polarised (I^Y) time integrated PL intensities (solid lines) following a circularly polarised (σ^+) quasi-resonant excitation (E_{exc}= 4.36 eV - λ_{exc} = 284 nm) at T= 4 K and corresponding PL linear polarisation degree (dark yellow circles).* 64

3.10 *a), b) : Geometry of experiment A and B, respectively. The blue vector presents the linear polarisation of the excitation light. The red orthogonal frame $(\vec{e}(\alpha), \vec{e}_\perp(\alpha))$ is the detection frame which is rotated by an angle α with respect to the laboratory frame $(\vec{e}_X, \vec{e}_Y)$. The orthogonal frame $(\vec{e}(\theta), \vec{e}_\perp(\theta))$ corresponds to the orthogonal eigenstates of a given class of exciton dipoles (see explanation in section 3.3.5).* 66

3.11 *The PL linear polarisation degree measured under quasi-resonant excitation after a simultaneous rotation of both the excitation and detection reference frames with different rotation angles α at (a) 7.5 K and (b) 300 K. (a) $\alpha = 0^o$ - green circles; $\alpha = 18^o$ - pink circles; $\alpha = 42^o$ - orange squares; $\alpha = 66^o$ - dark yellow rhombi; $\alpha = 78^o$ - cyan circles; $\alpha = 90^o$ - blue triangles. (b) $\alpha = 0^o$ - green circles; $\alpha = 45^o$ - orange squares; $\alpha = 90^o$ - blue triangles. $\pi^{X(Y)}$ indicate respectively a linearly (X or Y, with respect to the laboratory frame) polarised excitation. The superscripts in $I^{X/Y}$ ($I^{X'/Y'}$) indicate the polarisation directions of the PL intensities used to calculate the PL linear polarisation degree.* 67

3.12 *The linear polarisation degree of the photoluminescence measured along the $(\vec{e}(\alpha), \vec{e}_\perp(\alpha))$ basis following a linear excitation along the $\vec{e}_X$ axis (experiment B, T=8.5 K). The red line is a fit to the data according to equation 3.31 (section 3.3.5).* 69

3.13 *Time evolution of the PL components co- (I^X) and counter-polarised (I^Y) with the linearly polarised quasi resonant excitation (E_{exc}=4.24 eV) and the corresponding linear polarisation degree measured at two different energies. The grey area represents the temporal region dominated by the laser scattered light. The spectra are spectrally integrated according to the caption in the figure.* 70

3.14 *Dynamics of the low temperature (T=8.5 K) PL components co- (I^X) and cross-polarised (I^Y) with the linearly polarised excitation and the corresponding linear polarisation degree. The grey area represents the temporal region dominated by the laser scattered light. Inset: the measured PL linear polarisation degree for all the temperatures investigated. The energy difference between excitation and detection has been kept constant at ΔE =133 meV, and the excitation energy has been varied according to the temperature variation of the QD gap in order to excite the same nanowires family.* 71

4.1 *Schematic representation of the SDR mechanism under circular (left panel) and linear (right panel) excitations. Figure a (d) correspond to the state at t = 0 just after optical excitation, figure b (e) represent the state after the capture of free electrons on deep paramagnetic centres, and figure c (f) correspond to the state after few circles of capture of free electrons in the CB and recombination of electrons in the centres with holes in the VB. To simplify, we assume here that the polarisation of the photogenerated electrons in the CB under circularly polarised excitation is 100%.* 89

4.2 *(a) The time-integrated total PL intensity of dilute nitride semiconductor $GaAs_{1-y}N_y$ (y = 2.1 %) under circularly (red line)/linearly (blue line) polarised excitations and the corresponding SDR ratio (orange circles) for P_{exc} = 20 mW, T= 300 K. (b) The corresponding time evolution of total PL intensities [17].* 90

4.3 *(a) The schematic mechanism of the spin filtering effect. After being polarised (Fig. 4.1c), the deep paramagnetic centres act as a spin filter which maintains the high CB electron spin polarisation. (b)The time evolution of the co- and counter-polarised components of the PL intensity after a circularly polarised excitation and the corresponding circular polarisation degree in $GaAs_{1-y}N_y$ (y = 2.1 %) at 300 K, P_{exc}= 20 mW. The spin filtering effect is clearly observed [17].* 91

4.4 *The power dependence (a) of the photoluminescence circular polarisation dynamics and (b) of the SDR ratio in $GaAs_{1-y}N_y$ (y = 2.1 %) at T = 20 K [21].* 93

4.5 *The optically detected magnetic resonance (ODMR) spectra obtained by monitoring the total intensity of the band-to-band PL from a* $GaN_{0.021}As_{0.979}$ *epilayer, obtained at 3K under linear* (σ^X) *and circular* (σ^+) *excitation at 850 nm. A simulated ODMR spectrum of the* Ga_i *defect (denoted by* $Ga_i - C$*) is also shown. The excellent correspondence between the experimental and simulated spectra confirms the origin of the paramagnetic centres [23].* 94

4.6 *(a) Side view - the sample structure grown on a GaAs substrate. (b)Top view - the schematic configuration of squares with different implanted ion doses and (c) SEM image of four of the seven squares.* 96

4.7 *(a) The normalised time integrated PL intensities of as-grown (non implanted) and implanted (square 7) samples under a circularly polarised excitation at* $T = 8$ *K and* $P_{exc} = 10$ *mW. The spectra components of GaAs and InGaAs are noted. (b) The normalised time evolution of PL intensities originating from GaAs and InGaAs in as-grown (black line) and implanted (red line) samples at low temperature.* 97

4.8 *The time integrated PL intensities of the sample with ion dose* $4.5 \cdot 10^9$ cm^{-2} *under circular (black line) and linear (grey line) excitation and the corresponding SDR ratios (red circles) at* $T = 25K$ *and* $P_{exc} = 10mW$. *The green squares represent the SDR ratio observed for the as-grown sample.* 99

4.9 *The time evolution of PL intensity under circularly (black line)/linearly (gray line) polarised excitation and the dynamics of the corresponding SDR ratio (red circles).* 99

4.10 *The evolution of the maximum SDR ratio as a function of the implantation dose. For each dose, the error bars are deduced from the inhomogeneity of the measured SDR ratio as observed in the same implanted square regions. The Ga ion dose which produces the highest SDR ratio is* $5 \cdot 10^9$ *ion/cm*$^{-2}$. 100

4.11 *The photoluminescence spectra of square 5 (ion implanted* $4.5.10^9$ */cm*$^{-2}$*) under circular* (σ^+)*/linear(*σ^x*) excitations* ($P_{exc} = 5mW, T = 25K$) *and corresponding SDR ratios with* ($B_\parallel = 230mT$) *and without external magnetic field in Faraday geometry.* 101

4.12 *The evolution of the SDR ratio as a function of the external magnetic field in Faraday geometry at room temperature for a* $GaAs_{0.993}N_{0.007}$ *sample.* 102

List of Tables

1.1 *Lattice parameters for GaN, AlN, GaAs and* $Ga_{0.91}In_{0.09}As$ *at room temperature [2–7].* 5

1.2 *Periodic part* u_n *of the Bloch functions of the conduction and valence bands' eigenstates at the center of the Brillouin zone* ($\vec{k} = 0$) *in zinc-blend semiconductors. The states* (u_1, u_2) *are associated with the electrons in the conduction band, meanwhile the states* (u_3, u_4), (u_5, u_6) *and* (u_7, u_8) *are associated respectively with the heavy holes, light holes and split-off holes in the valence band.* 7

1.3 *Periodic part* u_n *of the Bloch functions of eigenstates in the conduction and valence band at center of the Brillouin zone* ($\vec{k} = 0$) *in wurtzite semiconductors. The states* (u_1, u_2) *are associate with the conduction band electrons, meanwhile the states* (u_3, u_4), (u_5, u_6) *and* (u_7, u_8) *are associated with holes in valence sub-band A, B and C respectively [10]. The constants* α *and* β *satisfy* $\alpha^2 + \beta^2 = 1$. 9

1.4 *Band structure parameters for GaN, GaAs and InAs at 300 K [5–7].* . . 10

1.5 *Fundamental parameters of common semiconductors at room temperature: electron* (m_e^*) *and hole* (m_h^*) *effective mass, relative dielectric constant* (e_r), *exciton binding energy* (E_{ex}) *and exciton Bohr radius* (a_B) *[21].* 12

1.6 *The selection rules for the transition between valence and conduction band at* $\vec{k} = 0$ *with a linearly polarised electromagnetic radiation with polarisation state* $\vec{e}$ *and wave vector* $\vec{q}$ *in (a) ZB and (b) WZ bulk semiconductor.* $\Pi^2 = E_p/(2m_0)$ *where* E_p *is the Kane energy of the considered semiconductor [9, 10].* 30

2.1 *Picosecond Ti:Sapphire laser main characteristics.* 40

2.2 *Characteristics of the GWU-FHG frequency doubler/tripler.* 41

2.3 *Temporal mode and corresponding resolution of the S1 streak camera. This values are practically unchanged for the S20 type one.* 44

2.4 *The characteristics of the Jobin-Yvon Triax 320 and iHR monochromators. The spectral resolution values are given for 200 μm and 80 μm widths of the entrance and exit slit respectively.* 46

4.1 *The Ga^{2+} ion surface doses used to implant the sample.* 95

Abbreviation

ZB	Zinc-Blend
WZ	Wurtzite
3D	Three Directions
2D	Two Directions
0D	Zero Directions
CB	Conduction Band
VB	Valence Band
HH	Heavy Hole
LH	Light hole
SO	Split-off
QW	Quantum Well
QD	Quantum Dot
SK	Stranski-Krastanov
PL	Photoluminescence
EY	Elliott-Yafet
DP	D'yakonov-Perel
BAP	Bir-Aronov-Pikus
TRPL	Time-Resolved Photoluminescence
CCD	Charge Coupled Device
cw	Continuous wave
LBO	Lithium Triborate (LiB_3O_4)
BBO	Barium Borat (BaB_2O_4)
UV	Ultra Violet
FHG	Flexible Harmonic Generator
SEM	Scanning Electron Microscope
HRTEM	High-resolution Transmission Electron Microscope
LO	Longitudinal Optical
SDR	Spin-Dependent Recombination

Introduction

Switching the information-generating and -processing tasks in semiconductors from conventional charge-based electronics to the domain of spintronics could lead to novel devices marrying the technological possibilities of micro- and nano-electronics to the theoretically predicted improved features in data manipulation speed and power consumption of spin-based operations. The possibility of controlling the carriers spins state and charge, of tailoring the fundamental transition energy through band gap engineering or material alloying leading to possible optical control, together with the well established industrial technology ”savoir-faire”, confer the semiconductor materials a key role in the spintronics scenario.

Due to these potentialities, the research in this subject has attracted considerable attention in the last decade. Despite the rapid and extensive advances in the field, considerable effort has still to be done to overcome the existing fundamental and technological issues before ”real” devices could hit the consumer market. For instance, storing and manipulating the spin require the spin orientation to be stable over a sufficiently long period of time at room temperature. Injection and transport of spin polarised carriers together with spin filtering are all so far restricted to a limited efficiency and primarily at low temperatures or under a magnetic field.

Different approaches have been developed and proposed by the scientific community to address these problems. Two of the most successful routes to achieve these goals have been: (i) the confinement of carriers in the three spatial directions in nanometre-sized objects such as (In)GaAs or CdTe quantum dots, or more recently on wide gap (In)GaN materials, the latter allowing for the maintaining of a stable carrier polarisation up to room temperature. Although the nano-objects differ from one another, the possibilities of optically or electrically address a single nanostructure has been proved as an ideal testing ground for the most advanced theories on semiconductor optoelectronics. (ii) The second approach relies instead on the engineering of defects in semiconductors in forms of donors, acceptors, vacancies or deep paramagnetic centres. P atoms in Si, or N vacancies in Diamond and again Ga paramagnetic centres in dilute nitrides are just a few examples. In this second approach, ensemble addressing of spin states is moreover possible thanks to the physical identity of each of the defects, greatly simplifying the experimental task.

This work provides a contribution to both of these approaches. On one side, thanks to the recent advances in the growth of wide gap nano structures and the promising results obtained in these compounds in previous works in the group, we have studied the spin properties of nanowire-embedded GaN/AlN quantum dots by optical spectroscopy. On the other side, taking inspiration from the exceptional spin filtering properties of deep paramagnetic centres in dilute nitrides, we propose here a proof of concept based on the ion implantation of the centres without the need of nitrogen insertion. Spatial resolution and independence of the filtering efficacy from the emission wavelength are some of the advantages put forward by this approach.

The manuscript is organised in four chapters:

The first chapter is dedicated to a concise description of the essential notions necessary for the comprehension of the physical phenomena governing the spin properties in III-V semiconductors. The fundamentals of the band structure theory, the optical orientation rules and the spin relaxation mechanisms are presented.

In Chapter 2 we present the different experimental set-ups used for the realisation of this work. The time-integrated and the time- and polarisation-resolved photoluminescence set-ups are here introduced.

In Chapter 3 we present the results obtained on the exciton spin properties in nanowire-embedded GaN/AlN Quantum Dots. We will show how this material system allows the achievement of a sizable optical alignment of the exciton spin without any degradation up to room temperature. The notable differences with other wide-gap quantum dots systems will also be addressed.

The engineering of the Spin Dependent Recombination (SDR) in nitrogen-free epilayer is the subject of Chapter 4. We show here how the implantation of Ga ions by Focused Ion Beam allows for the selective creation of spin filtering regions in non-magnetic InGaAs layers. In particular, the optimum implantation conditions for the most efficient SDR are here determined. The effect of an external Faraday magnetic field will also be discussed.

Chapter 1

Introduction to the electronic and optical properties of III-V semiconductors

Contents

1.1 Introduction to the electronic properties of semiconductors: from bulk to quantum dots 5

1.1.1 Bulk semiconductor 5

1.1.2 Semiconductor heterostructures 13

1.2 Optical orientation in semiconductors 16

1.2.1 Optical transitions and selection rules 17

1.2.2 3D structures 18

1.2.3 2D structures 22

1.2.4 0D structures 23

1.3 Spin relaxation mechanisms 24

1.3.1 Elliott-Yafet mechanism 24

1.3.2 D'yakonov-Perel mechanism 24

1.3.3 Bir-Aronov-Pikus mechanism 26

1.3.4 Hyperfine-interaction mechanism 27

1.3.5 Exciton's spin relaxation mechanism 27

Bibliography 31

This first chapter concisely presents the fundamentals of band structure, optical orientation rules and spin relaxation mechanisms of III-V zinc blende and wurtzite materials.

This work has been essentially devoted to the study, by photoluminescence experiments, of the spin properties of nanowire-embedded AlN/GaN quantum dots and the spin filtering characteristics of ion implanted InGaAs layers. First we will briefly introduce the properties of the band structure at the centre of the Brillouin zone for III-V zinc blende and wurtzite semiconductors. We will then present how this propertie are affected by the dimensionality going from a 3D bulk structure to a 0D quantum dot.

We will then detail the fundamental principles of optical orientation experiments which are a consequence of the optical selection rules governing the interaction of electromagnetic radiation with the system under study. We will then show how to link these selection rules to the polarisation of the incident or emitted light and the spin polarisation of the photogenerated carriers. These are the principles used in this work to study the spin polarisation properties of semiconductors by photoluminescence experiments.

Finally, the main mechanisms responsible for the spin relaxation of carriers in semiconductors will be concisely reviewed.

1.1 Introduction to the electronic properties of semiconductors: from bulk to quantum dots

1.1.1 Bulk semiconductor

In this section we will briefly present the main parameters characterising single crystal bulk semiconductors both in zinc blend (ZB) and wurtzite (WZ) phases.

1.1.1.1 Crystal structure

Most of the semiconductors used in optoelectronics crystallise in either the zinc blend (ZB) or the hexagonal wurtzite (WZ) structures which are schematically represented in figure 1.1. The ZB and WZ phases differs only in the order of the atomic layers when seen along the [111] and [0001] directions respectively [8]. In the ZB structure, the atomic layers are assembled in a ABCABC sequence following the [111] direction (fig. 1.1a) but in the WZ structure, the atomic layers are put in ABAB order following the [0001] direction (fig 1.1b).

The ZB structure belongs to the symmetry group $F\bar{4}3m$ (T_d) and corresponds to two inter-penetrating face-centred cubic (fcc) systems of equal (Si, Ge, ...) or different (GaAs, InAs, ...) elements. These two fcc systems are separated from each other by a quarter of the diagonal of the conventional cell along the [111] direction. The lattice constant a corresponds to the length of the cube's side (conventional cell side, figure 1.1a). The lattice parameters of the ZB compounds used in these works are given in table 1.1.

The wurtzite structure belongs to symmetry group $P63mc$ (C_{6v}^4) and corresponds to two hexagonal sub-lattices of two elements separated by $3/8c$, c and a being the lattice parameters of the structure (figure 1.1b).

The lattice parameters of the WZ compounds used in these works are also given in table 1.1

Phase	Lattice constant	GaN	AlN	$GaAs$	$Ga_{0.91}In_{0.09}As$
WZ	a(A^o)	3.189	3.11		
	c(A^o)	5.185	4.98		
ZB	a(A^o)	4.5		5.65	6.02

Table 1.1: *Lattice parameters for GaN, AlN, GaAs and* $Ga_{0.91}In_{0.09}As$ *at room temperature [2–7].*

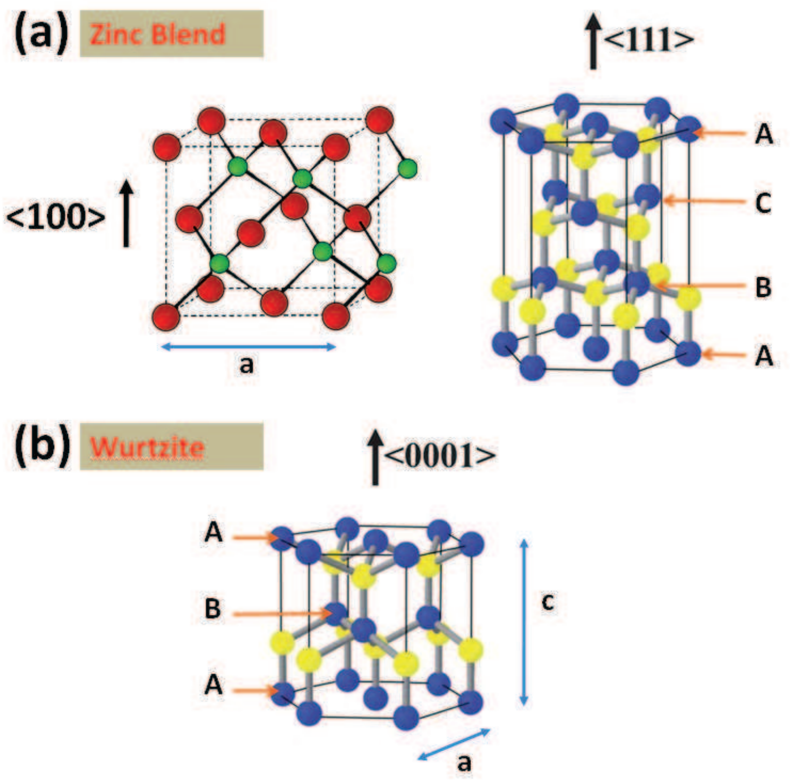

Figure 1.1: *The zincblende (a) and wurtzite (b) crystal structures [1, 7].*

1.1.1.2 Band structure

In a bulk semiconductor, the carriers (electrons, holes) can move freely in both three directions of space (3D). The energies of the allowed states are distributed in bands determined by the crystal potential and its symmetry. The description of the optical properties of the direct gap semiconductors usually requires the knowledge of the electronics states closed to the centre of the Brillouin zone, the Γ point ($\vec{k} = 0$). In this part, we will present the energy band structure of both ZB and WZ-type bulk semiconductors.

Zinc Blend type semiconductors A schematic energy band of the ZB structure (symmetry group T_d) is show in figure 1.2. The electronic states of bulk semiconductor can be described by the Bloch function as:

$$\Phi_{n,\vec{k}}\left(\vec{r}\right) = u_{n,\vec{k}}\left(\vec{r}\right) e^{i\vec{k}\cdot\vec{r}}, \tag{1.1}$$

in which $\vec{k}$ is an allowed wave vector of reciprocal space, $u_{n,\vec{k}}\left(\vec{r}\right)$ is a periodic function of the same period as the crystal lattice and characteristic of the chemical nature and bonding of the described material.

The states of the conduction band (CB) originate from the s anti-binding orbitals of the crystal, meanwhile the states in the valence band (VB) derive from the p bonding states. Each resulting band is twice degenerate due to the two possible states (up and down) of the electron spin. By using the atomic physics notation, the states in the CB at $\vec{k} = 0$ are described in the basis $\left\{\left|\vec{S}, \uparrow\right\rangle, \left|\vec{S}, \downarrow\right\rangle\right\}$; similarly, the states in the VB are described in the basis $\left\{\left|\vec{X}, \uparrow\right\rangle, \left|\vec{X}, \downarrow\right\rangle, \left|\vec{Y}, \uparrow\right\rangle, \left|\vec{Y}, \downarrow\right\rangle, \left|\vec{Z}, \uparrow\right\rangle, \left|\vec{Z}, \downarrow\right\rangle\right\}$, where $\uparrow$ and $\downarrow$ represent the two possible states of the electron spin.

When considering the spin-orbit interaction, the orbital ($\vec{L}$) and spin ($\vec{S}$) angular momenta are not any more good quantum numbers. The electronic states have to be described in the basis constituted by the total angular momentum $\vec{J} = \vec{L} + \vec{S}$ and its projection along the growth direction (Oz): $|J^2, J_z\rangle$. The spin-orbit interaction has little effects on the CB whereas the energy bands in the VB are greatly modified. The situation at the center of the Brillouin zone Γ ($\vec{k} = 0$) is the following. The CB is separated from the topmost of the VB states by an energy E_G. The area between CB and VB is called the forbidden gap. The VB states are composed of three sub-bands: the heavy-hole (HH) and light-hole (LH) bands, degenerated at center of Brillouin zone, and a "split-off" (SO) band separated from the two others by a split-off energy Δ_{SO} (figure 1.2) due to the spin-orbit interaction. The Bloch functions describing the eigenstates in the CB and VB are showed in table 1.2. Here the eigenfunctions (u_1, u_2) correspond to the states in the CB whereas (u_3, u_4), (u_5, u_6) and (u_7, u_8) describe respectively the states in the HH, LH and SO

$Eigenfunction$ $u_i(k=0)$	$Atomic\ notation$ $\|J, m_j\rangle$	$Eigenenergy$ $E_i(k=0)$
$u_1 = \|S, \uparrow\rangle$	$\left\|\frac{1}{2}, +\frac{1}{2}\right\rangle$	$E_{cond} = E_{HH} + E_G$
$u_2 = \|S, \downarrow\rangle$	$\left\|\frac{1}{2}, -\frac{1}{2}\right\rangle$	
$u_3 = -\frac{1}{\sqrt{6}} \|(X+iY), \downarrow\rangle + \sqrt{\frac{2}{3}} \|Z, \uparrow\rangle$	$\left\|\frac{3}{2}, +\frac{1}{2}\right\rangle$	E_{LH}
$u_4 = \frac{1}{\sqrt{6}} \|(X-iY), \uparrow\rangle + \sqrt{\frac{2}{3}} \|Z, \downarrow\rangle$	$\left\|\frac{3}{2}, -\frac{1}{2}\right\rangle$	
$u_5 = -\frac{1}{\sqrt{2}} \|(X+iY), \uparrow\rangle$	$\left\|\frac{3}{2}, +\frac{3}{2}\right\rangle$	$E_{HH} = E_{LH}$
$u_6 = \frac{1}{\sqrt{2}} \|(X-iY), \downarrow\rangle$	$\left\|\frac{3}{2}, -\frac{3}{2}\right\rangle$	
$u_7 = -\frac{1}{\sqrt{3}} \|(X+iY), \downarrow\rangle - \frac{1}{\sqrt{3}} \|Z, \uparrow\rangle$	$\left\|\frac{1}{2}, +\frac{1}{2}\right\rangle$	$E_{SO} = E_{HH} - \Delta_{SO}$
$u_8 = -\frac{1}{\sqrt{3}} \|(X-iY), \uparrow\rangle + \frac{1}{\sqrt{3}} \|Z, \downarrow\rangle$	$\left\|\frac{1}{2}, -\frac{1}{2}\right\rangle$	

Table 1.2: *Periodic part u_n of the Bloch functions of the conduction and valence bands' eigenstates at the center of the Brillouin zone ($\vec{k} = 0$) in zinc-blend semiconductors. The states (u_1, u_2) are associated with the electrons in the conduction band, meanwhile the states (u_3, u_4), (u_5, u_6) and (u_7, u_8) are associated respectively with the heavy holes, light holes and split-off holes in the valence band.*

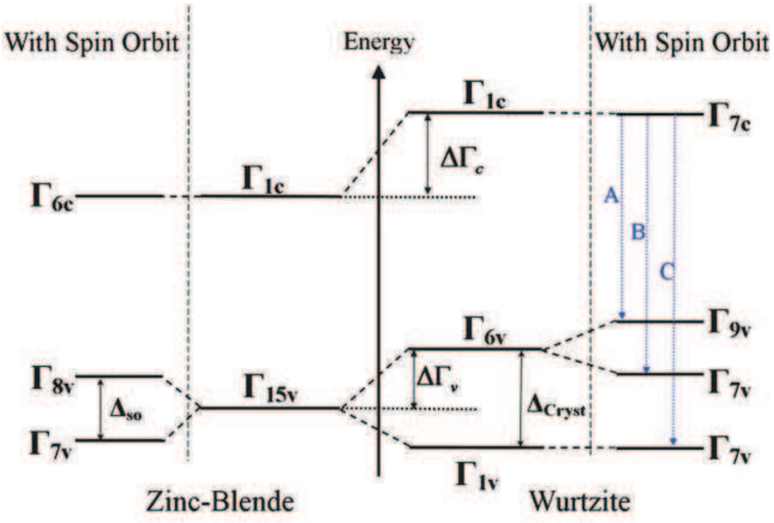

Figure 1.2: *Schematic of the band structure at the* Γ *point for ZB and WZ crystals with and without the inclusion of the spin-orbit interaction and, for the WZ structure, the crystal field [7].*

subbands.

Wurtzite type semiconductors In the case of wurtzite structures (symmetry group C_{6v}), due to the lowering of the symmetry and the presence of a crystal field Δ_{CR}, the degeneracy of the VB is partially lifted as depicted in figure 1.2. Similarly to the zinc blende structure, the spin-orbit interaction strongly affects the valence band structure which is finally split into three doubly degenerate sub-bands A, B and C. The eigenfunctions of the states in WZ semiconductors are reported in table 1.3. The eigenfunctions (u_1, u_2) correspond to the CB states; The (u_3, u_4), (u_5, u_6) and (u_7, u_8) are associated respectively to the A, B and C valence sub-bands.

In figure 1.3, we report the graph of the energy gap versus lattice constant for some familiar semiconductors at room temperature. The parameters concerning the compounds used in this work are reported in detail in table 1.4.

1.1.1.3 The Exciton

In semiconductors, the absorption of a photon whose energy satisfies $E \geq E_G$ provokes an electron transition from the valence band to one vacant state in the conduction band. This transition also creates a vacant state in the VB called a hole, behaving in all aspects as a positive carrier with opposite wavevector, spin and energy as compared to the removed electron. These photo-generated electron and hole pairs are subjected to the Coulomb attractive interaction creating a hydrogen-like complex called the *exciton*.

$Eigenfunction$ $u_i(k=0)$	$Atomic\ notation$ $\lvert J, m_j\rangle$	$Eigenenergy$ $E_i(k=0)$
$u_1 = \lvert S, \uparrow\rangle$ $u_2 = \lvert S, \downarrow\rangle$	$\left\lvert \frac{1}{2}, +\frac{1}{2}\right\rangle$ $\left\lvert \frac{1}{2}, -\frac{1}{2}\right\rangle$	$E_{cond} = E_A + E_G$
$u_3 = -\frac{1}{\sqrt{2}} \lvert (X+iY), \uparrow\rangle$ $u_4 = \frac{1}{\sqrt{2}} \lvert (X-iY), \downarrow\rangle$	$\left\lvert \frac{3}{2}, +\frac{3}{2}\right\rangle$ $\left\lvert \frac{3}{2}, -\frac{3}{2}\right\rangle$	E_A
$u_5 = -\frac{1}{\sqrt{2}}\alpha \lvert (X+iY), \downarrow\rangle + \beta \lvert Z, \uparrow\rangle$ $u_6 = \frac{1}{\sqrt{2}}\alpha \lvert (X-iY), \uparrow\rangle + \beta \lvert Z, \downarrow\rangle$	$\left\lvert \frac{3}{2}, +\frac{1}{2}\right\rangle$ $\left\lvert \frac{3}{2}, -\frac{1}{2}\right\rangle$	$E_B = E_A - \Delta_{SO}/3$
$u_7 = -\frac{1}{\sqrt{2}}\beta \lvert (X+iY), \downarrow\rangle - \alpha \lvert Z, \uparrow\rangle$ $u_8 = -\frac{1}{\sqrt{2}}\beta \lvert (X-iY), \uparrow\rangle + \alpha \lvert Z, \downarrow\rangle$	$\left\lvert \frac{1}{2}, +\frac{1}{2}\right\rangle$ $\left\lvert \frac{1}{2}, -\frac{1}{2}\right\rangle$	$E_C = E_A - \Delta_{SO}/3 - \Delta_{CR}$

Table 1.3: *Periodic part u_n of the Bloch functions of eigenstates in the conduction and valence band at center of the Brillouin zone ($\vec{k} = 0$) in wurtzite semiconductors. The states (u_1, u_2) are associate with the conduction band electrons, meanwhile the states (u_3, u_4), (u_5, u_6) and (u_7, u_8) are associated with holes in valence sub-band A, B and C respectively [10]. The constants α and β satisfy $\alpha^2 + \beta^2 = 1$.*

The first theories about the excitons were given by Frenkel and Wannier in the 30s. In their framework, Frenkel and Wannier described two types of exciton as a function of the electron-hole separation compared to the size of the unit cell of the material. In a Frenkel exciton, the relative distance of an electron-hole pair is smaller than the unit cell, whereas it is larger for Wannier-Mott type excitons [15, 17]. In the exact description, however, an exciton is a N body system, a single electron promoted to the conduction band is less repelled by the Coulomb interaction with the N-1 electrons (or attracted by the single hole) occupying the VB. In this work we will give a simple description of Wannier-Mott excitonic states keeping the electron-hole representation.

In the framework of the effective mass approximation the correlated movement of an electron-hole pair can be split into the movement of a particle linked to the center of mass of position $\vec{R}$ and mass M^* and the relative movement of a reduced mass particle of position $\vec{\rho}$ and mass μ. The change of variables is given by:

$$\begin{aligned} \vec{R} &= \frac{m_e^* \vec{r}_e + m_h^* \vec{r}_h}{M^*}, & \vec{r} &= \vec{r}_e - \vec{r}_h, \\ M^* &= m_e^* + m_h^*, & \frac{1}{\mu} &= \frac{1}{m_e^*} + \frac{1}{m_h^*}, \\ \vec{K} &= \vec{k}_e + \vec{k}_h, & \vec{k} &= \frac{m_h^* \vec{k}_e - m_e^* \vec{k}_h}{M^*} = \mu \dot{\vec{r}}, \end{aligned} \tag{1.2}$$

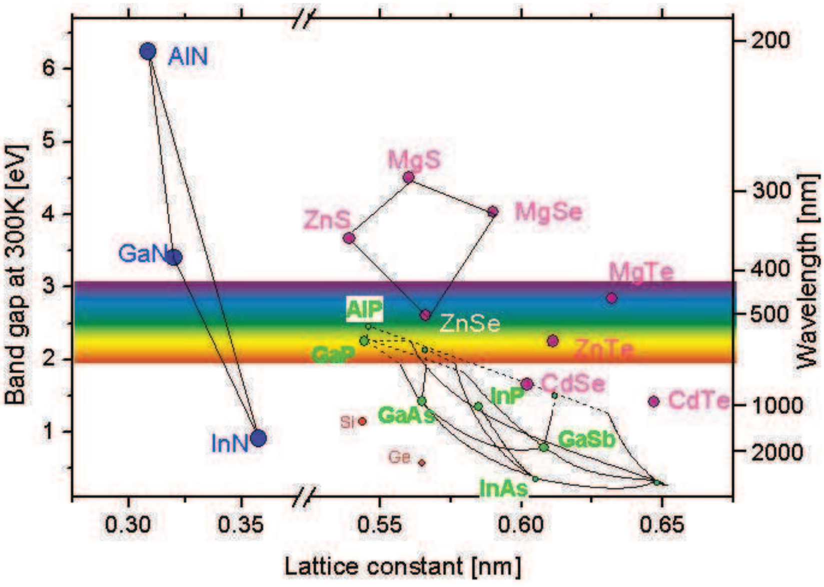

Figure 1.3: *The variation of the band gap energy versus lattice constant for some common semiconductors at room temperature [2].*

Parameter	Phase	GaN	$GaAs$	$InAs$
E_g (eV) at 300 K	WZ	3.39		
	ZB	Γ:3.299 X:4.52	Γ:1.424 X:1.90 L:1.71	Γ:0.35 X:1.37 L:1.08
Δ_{SO} (meV)	WZ	17		
	ZB	17	341	410
Δ_{CR} (meV)	WZ	10		

Table 1.4: *Band structure parameters for GaN, GaAs and InAs at 300 K [5–7].*

where $\vec{r}_{e,h}$, $\vec{k}_{e,h}$ and $m^*_{e,h}$ represent respectively the position, wave vector and effective mass of the electron (index e) and hole (index h). The wave function of an exciton in the case of a bulk semiconductor can be written as:

$$\Phi_{ex}\left(\vec{R},\vec{r}\right) = \frac{1}{\sqrt{V}} e^{i\vec{K}\vec{R}} \Phi_{env}\left(\vec{r}\right) u_{c,o}\left(\vec{r_e}\right) u^*_{v,o}\left(\vec{r_h}\right), \tag{1.3}$$

where V is the crystal volume, $u_{c,o}\left(\vec{r_e}\right), u^*_{v,o}\left(\vec{r_h}\right)$ are the electron and hole Bloch functions. $\Phi_{env}\left(\vec{r}\right)$ is the envelope function describing the movement of the reduced mass particle. This last function is formally identical to the 1s hydrogen orbital (for the lowest exciton state) and is written:

$$\Phi_{env}\left(\vec{r}\right) = \frac{1}{\sqrt{\pi a_B^3}} e^{-\frac{|\vec{r}|}{a_B}}, \tag{1.4}$$

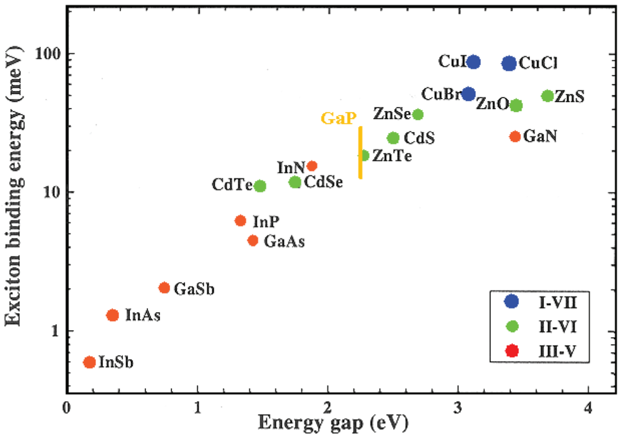

Figure 1.4: *The exciton binding energies versus band gap for common semiconductors at room temperature [21].*

in which a_B is the Bohr radius of the exciton. Relations (1.3) and (1.4) mean that the wave function of exciton is delocalised in the whole crystal but the electron and hole are separated from each other by an average distance of the order of the Bohr radius. The Bohr radius depends on the nature of the materials and is given by the relation:

$$a_B = a_0 \epsilon_r \frac{m_0}{\mu}, \tag{1.5}$$

where a_0 is the Bohr radius of the hydrogen atom, ϵ_r is the relative dielectric constant of the material, m_0 is the free electron mass, and μ is the reduced effective mass.

The energy of an exciton of wavevector $\vec{K}$ writes:

$$E_{ex}^{3D}\left(\vec{K}, n\right) = E_G - \frac{E_{ex}^b}{n^2} + \frac{\hbar^2 \vec{K}^2}{2M^*}, \tag{1.6}$$

where n is the principal quantum number of the exciton and E_{ex}^b is the 1s exciton binding energy. As showed in figure 1.5, the exciton binding energy is defined as the energy difference between the band gap energy E_G and the energy of the exciton on the fundamental state ($\vec{K} = \vec{0}$) :

$$E_{ex,n}^b = R_y^* \frac{1}{n^2} = 13.6(eV) \frac{\mu}{m_0} \frac{1}{\epsilon_r^2} \frac{1}{n^2}, \tag{1.7}$$

where R_y^* is the effective Rydberg constant which takes into account the material environment through the effective mass and the relative dielectric constant. Figure 1.4 and table 1.5 report the exciton binding energies and exciton Bohr radii of some common semiconductors.

The excitons constitute fundamental electronic excitations of the crystal. They introduce important modifications to the optical properties of semiconductors, appearing as resonances in reflectivity (absorption, transmission) and peaks in photoluminescence spectra at an energy lower than the band gap energy E_G. We note

Material	m_e^*	m_h^*	e_r	$E_{ex}[meV]$	$a_B[nm]$
BN	0.752	0.38	5.1	131	1.1
GaN	0.20	0.80	9.3	25.2	3.1
InN	0.12	0.50	9.3	15.2	5.1
GaAs	0.063	0.50	13.2	4.4	12.5
InP	0.079	0.60	12.6	6.0	9.5
GaSb	0.041	0.28	15.7	2.0	23.2
InAs	0.024	0.41	15.2	1.3	35.5
InSb	0.014	0.42	17.3	0.6	67.5
ZnS	0.34	1.76	8.9	49.0	1.7
ZnO	0.28	0.59	7.8	42.5	2.2
ZnSe	0.16	0.78	7.1	35.9	2.8
CdS	0.21	0.68	9.4	24.7	3.1
ZnTe	0.12	0.6	8.7	18.0	4.6
CdSe	0.11	0.45	10.2	11.6	6.1
CdTe	0.096	0.63	10.2	10.9	6.5
HgTe	0.031	0.32	21.0	0.87	39.3

Table 1.5: *Fundamental parameters of common semiconductors at room temperature: electron* (m_e^*) *and hole* (m_h^*) *effective mass, relative dielectric constant* (e_r)*, exciton binding energy* (E_{ex}) *and exciton Bohr radius* (a_B) *[21].*

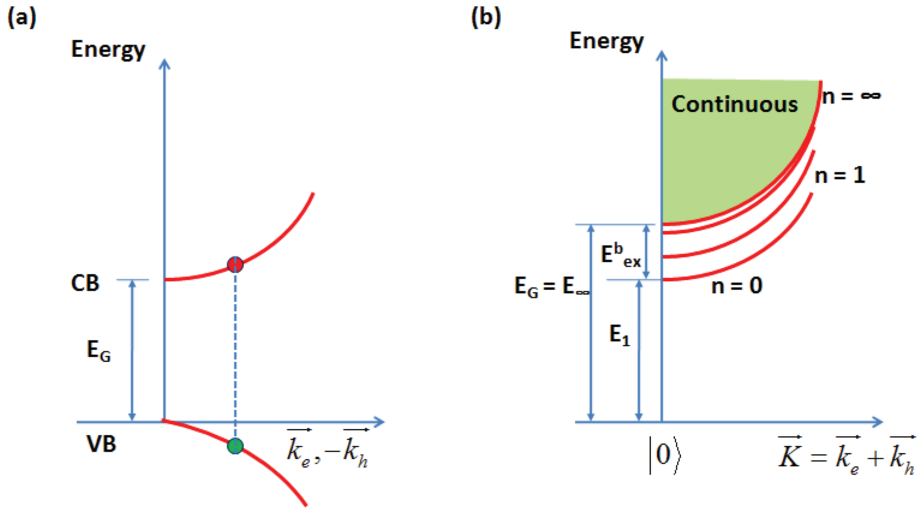

Figure 1.5: *The electron-hole pair in (a) the two particle picture and (b) the exciton picture.*

that when $n \to \infty$ the exciton states converge to the ionization continuum in which the transition of the exciton turns into the band to band transition at an energy equal to the band gap E_G (figure 1.5).

The fine structure of excitons in 3D structures The fine structure of excitons arises from the different combination possibilities of the electron's and hole's angular momenta. The exciton states at $\vec{K} = 0$ for ZB and WZ type semiconductors are respectively formed by the tensor product of the electron and hole states according to the expressions given in tables 1.2 and 1.3. The electron spin is described by the angular momenta projection on the z quantization axis: $s_z = \pm 1/2$ (in $\hbar$ units). The holes are characterized by the angular momenta projection $j_z = \pm 3/2$ or $j_z = \pm 1/2$. The angular momentum projection of exciton is then $J_z = j_z + s_z$. In the case the exciton is formed by the combination of a CB electron and a heavy hole state ($j_z = \pm 3/2$), two possible compositions may arise:

$$|1, \pm 1\rangle = \left|\frac{3}{2}, \pm\frac{3}{2}\right\rangle \otimes \left|\frac{1}{2}, \mp\frac{1}{2}\right\rangle \text{ and } |2, \pm 2\rangle = \left|\frac{3}{2}, \pm\frac{3}{2}\right\rangle \otimes \left|\frac{1}{2}, \pm\frac{1}{2}\right\rangle. \tag{1.8}$$

Similar compositions can be performed for the other valence sub-band states.

The Coulomb exchange interaction between an electron and a hole plays an important role in the determination of the exciton fine structure [12]. This interaction consists of two contributions:

- The short-range interaction: This contribution can be defined as a contact interaction. It depends on the angular momentum of the carriers and the symmetry of the system. It contributes to the lift of the degeneracy between dark and bright exciton states. In GaAs, this contribution is small ($\Delta_0^{GaAs} = 0.02$ meV) [22], whereas in GaN it is much larger ($\Delta_0^{GaN} = 0.69$ meV) [23].

- The long-range interaction: This term is responsible to the longitudinal-transverse splitting of exciton energies. This interaction only appears for bright states $|1, \pm 1\rangle$. In contrast to GaAs in which this interaction is relatively weak ($\Delta_{LT}^{GaAs} = 0.08 \pm 0.02$ meV [22, 28]) in GaN WZ the long-range term is very strong: $\Delta_{LT}^{A} = 1.5$ meV and $\Delta_{LT}^{B} = 11$ meV [23].

We will come back to the exciton fine structure when treating the optical selection rules in section 1.2.

1.1.2 Semiconductor heterostructures

A heterostructure is composed of different layers of dissimilar crystalline semiconductors with unequal bandgap energies. In practice, advanced epitaxial techniques such as Molecular Beam Epitaxy (MBE) or Metal-Organic Chemical Vapor Deposition (MOCVD) allow the growth of layers as thin as a few atomic layers. In

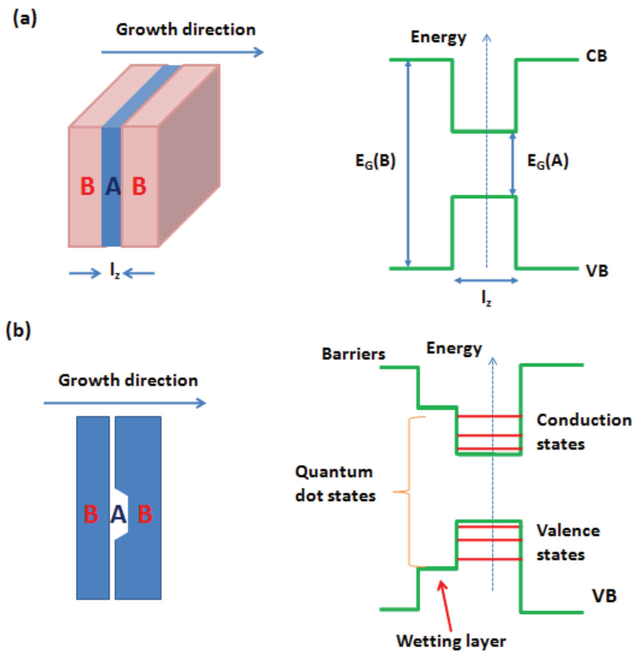

Figure 1.6: *Schematics and energy diagram of (a) a quantum well and (b) a quantum dot heterostructures.*

these layers the motion of carriers is quantized. The heterostructural interfaces play a critical role in semiconductor heterostructure devices such as field-effect transistor (FET), bipolar transistor, light-emitting diode (LED), laser, etc... This section will briefly present two basic semiconductor heterostructures: quantum wells and quantum dots (figure 1.6).

1.1.2.1 Quantum Wells

A quantum well (QW) structure (figure 1.6 (a)) is fabricated by embedding a thin film of material A between two layer of barrier material B possessing a larger energy band gap compared to material A. In this structure, carriers are free to move in the plane (2D) normal to the growth direction (Oz) but are confined along the growth direction. Because of this confinement, the energy states of the carriers are quantized in the confined direction. It results that the carrier's energy can be separated into two parts, one due to the quantum confinement along Oz, the other in the plane perpendicular to that direction (xOy plane). The dispersion relation writes:

$$E\left(\vec{k}\right) = E_{n_z} + \frac{\hbar^2\left(k_x^2 + k_y^2\right)}{2m_{e,h}}. \tag{1.9}$$

In the infinite barrier approximation ($E_G(B) = \infty$), for a QW of width l_z the confinement energy is given by:

$$E_{n_z}^{e,h} = \frac{\hbar^2\pi^2}{2m_{e,h}l_z^2}n_z^2, \;\; n_z = 1, 2, 3\ldots, \tag{1.10}$$

in which n_z is the principal quantum number for electrons or holes.

In the case of ZB semiconductors, this confinement energy is responsible for the lift of the degeneracy of the heavy- and light-hole bands due to their different effective masses $m_{hh} \neq m_{lh}$.

2D excitons The configuration and dimensions of the nanostructure affect not only the density of states but also the energies of the excitons. In the case of 2D excitons, the movement of electrons and holes are restrained in the Oz direction. The corresponding wave functions can be respectively described as $u_{co}(\vec{r})$ and $u_{vo}(\vec{r})$. In the plane, the movement of the exciton is described by considering separately the movement of the centre of mass of the electron-hole pair and the movement of the reduced-mass particle. The centre-of-mass movement is characterised by a plane wave while the movement of the reduced-mass particle is represented by a 2D $1s$ hydrogenoid function as:

$$\Phi_{env}^{2D}\left(\vec{r}_{\parallel}\right) = \sqrt{\frac{1}{\pi a_{2D}^2}} exp\left(-\frac{|\vec{r}_{\parallel}|}{2a_{2D}}\right), \tag{1.11}$$

where the 2D Bohr radius a_{2D} describes the mean distance between the electron and hole in the plane.

The dispersion relation of a 2D exciton is then given by:

$$E_{ex}^{2D}\left(\vec{K}, n\right) = E_g + E_{n_z}^{e} + E_{n_z}^{h} - E_{ex}^{b}(3D)\frac{1}{\left(n-\frac{1}{2}\right)^2} + \frac{\hbar^2\left(K_x^2+K_y^2\right)}{2M^*}, \tag{1.12}$$

where $E_{n_z}^{e(h)}$ corresponds to the quantized energy of electron (hole) in the QW given by equation 1.10 in the infinite barrier approximation. The $1s$ exciton binding energy is therefore increased in the 2D case according to $E_{ex}^{b}(2D) = 4E_{ex}^{b}(3D)$ together with its oscillator strength. Indeed, the quantisation along the Oz direction increases the electron-hole wave functions overlap and thus reduces the exciton Bohr radius a_{2D}.

1.1.2.2 Quantum Dot

The typical configuration of a quantum dot (QD) system is presented in figure 1.6(b). In these structures the confinement occurs along all three directions of space resulting in the discretisation of the energy states. This characteristic is at the origin of the terminology "artificial atom" often used to denoted quantum dots.

QDs are usually grown by the "Stranski-Krastanov" technique. This consists in the spontaneous nucleation, under particular and controlled conditions, of nanometre-sized structures in molecular beam epitaxy when a material is grown on top of another one with a different lattice constant. In these "self-assembled" QDs, the in-plane dimensions are generally larger than the height $(L_x, L_y) \gg (L_z \sim a_B)$. As a consequence, the exciton trapped in a QD is more strongly confined in the growth (vertical) direction compared to the lateral ones. For this reason, the exciton movement can be separately described by an in-plane function plus a strongly confined vertical component along Oz.

Along the Oz direction the confinement energy is greater than the Coulomb interaction. By modelling the z confinement as an infinite potential well of l_z width, the electron and hole energies are respectively given by $n_e^2\pi^2\hbar^2/2m_e^* l_z^2$ and $n_h^2\pi^2\hbar^2/2m_h^* l_z^2$, where n_e and n_h are the principal quantum numbers of the confined electrons and holes.

For the in-plane confinement, two distinct possibilities may arise depending on the relative strength of the electrostatic and confinement energies. In the case of the GaN/AlN heterostructures studied in this work, due to the relatively large in-plane dimensions of the quantum dots the carriers are only weakly confined in the dot plane. A description in terms of "exciton" is therefore the more adapted one compared to the InAs/GaAs case where the electrostatic interaction is only taken into account as a perturbation.

In the weak in-plane confinement case of GaN/AlN dots, the correlation between the electron and hole is only weakly perturbed by the localization of the center of mass. This is very similar to the 2D case in quantum wells (in section 1.1.2.1) where, however, the centre-of-mass movement is described by a localised envelope function $\Psi(X,Y)$ instead of a plane wave. Finally, the wavefunction of an exciton in a "flat" quantum dot is given by:

$$\Phi\Big(X, Y, \vec{\rho_\parallel}, n_{z_e}, n_{z_h}\Big) = \Phi_{e,n_{z_e}}(z_e)\, \Phi_{h,n_{z_h}}(z_h)\, \Phi_{env}^{2D}\left(\vec{\rho_\parallel}\right) \Psi(X,Y) u_{c,0}(\vec{r_e})\, u_{h,0}(\vec{r_h}), \tag{1.13}$$

where $\Phi_{e,n_{z_e}}(z_e)$ and $\Phi_{h,n_{z_h}}(z_h)$ are respectively the electron and hole wavefunctions along Oz and $\Phi_{env}^{2D}\left(\vec{\rho_\parallel}\right)$ is the 2D hydrogenoid envelope wavefunction as in equation (1.11).

1.2 Optical orientation in semiconductors

Photoluminescence (PL) is a powerful technique to investigate the optical properties of semiconductors. PL provides very rich information not only on exciton, phonon, and donor binding energies but also on the intrinsic and various recom-

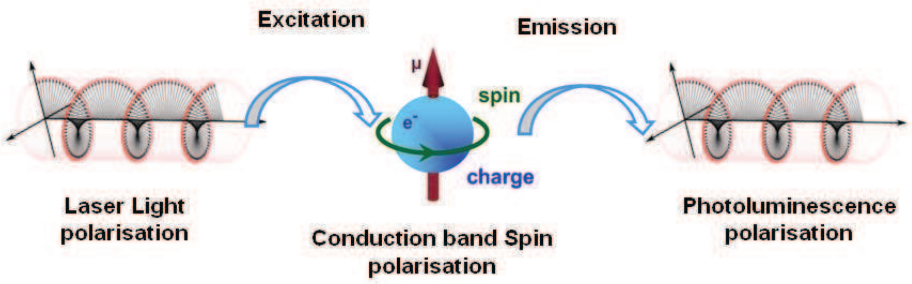

Figure 1.7: *The principle of the optical orientation method. Carriers with a definite spin are excited with polarised light. The analysis of the emitted ligh polarisation is then used to extract the carrier spin properties.*

bination processes which occur in a sample. In this section, we will briefly review the optical orientation technique applied to PL used in this work to investigate the dynamical spin properties of semiconductors (figure 1.7).

When a photon interacts with a direct-bandgap material whose energy gap is smaller than photon's energy, the photon will transfer its energy and angular momentum to an electron in the valence band. Such electron can be transferred to a vacant state in the conduction band leaving a hole in the valence band: a photo-generated electron hole pair is thus created. After a certain time (typically in the range of ps - ns), this electron will recombine with a hole in the valence band and gives off its excess energy in a photon by spontaneous emission. In optical orientation experiments, polarised light is used to impose a definite spin polarisation to the photo-generated electron according to the optical selection rules. By analysing the polarisation of the emitted photon upon recombination, it is possible to infer the spin polarisation state of the emitting carriers and possibly (in time resolved experiments) the corresponding dynamics.

1.2.1 Optical transitions and selection rules

The Hamiltonian of an electron in the presence of electromagnetic field is written in the Coulomb Gauge as :

$$H = \frac{1}{2m_0}(\vec{\boldsymbol{p}} - \frac{e\vec{\boldsymbol{A}}}{c})^2 + V(\vec{\boldsymbol{r}}), \tag{1.14}$$

where $\vec{\boldsymbol{A}}$ is the vector potential.

This Hamiltonian can be developed as :

$$H = H_0 - \frac{e}{m_0 c}\vec{\boldsymbol{A}} \cdot \vec{\boldsymbol{p}} + \frac{e^2}{2m_0 c}\vec{A}^2,$$

where $H_0 = \frac{p^2}{2m_0} + V(\vec{r})$. By neglecting the second order term in $\vec{\boldsymbol{A}}$, the interaction Hamiltonian between an electron and electromagnetic field can be simplified as :

$$H_{int} = -\frac{e}{m_0 c}\vec{\boldsymbol{A}} \cdot \vec{\boldsymbol{p}}, \tag{1.15}$$

where e is the electron charge, m_0 the electron mass, c is the speed of light.

Using the first-order time-dependent perturbation theory the Fermi Golden Rule states that the transition rate of an electron from an initial state $|i\rangle$ with an energy E_i to a final state $|f\rangle$ with an energy E_f upon absorption of a photon of energy $\hbar\omega$ is given by:

$$W_{if} = \frac{2\pi}{\hbar} \left|\langle i|H_{int}|f\rangle\right|^2 \delta(E_f - E_i - \hbar\omega). \tag{1.16}$$

The Dirac function δ ensures energy conservation while the values of the transition matrix elements $\left|\langle i|H_{int}|f\rangle\right|^2$ [16] determine the allowed transitions and their relative strength: this defines the optical selection rules.

For a monochromatic plane wave characterized by an electric field:

$$\vec{E}(r,t) = \frac{E_0}{2}\vec{e}\left(e^{i(\omega t - \vec{q}\cdot\vec{r})} + c.c.\right),$$

the transition matrix elements can be written in the dipole approximation as:

$$\left|\langle f\left|H_{int}\right| i\rangle\right|^2 = \left(\frac{eE_0}{2m_0\omega}\right)^2 \left|\langle f\left|\vec{e}\cdot\vec{p}\right| i\rangle\right|^2, \tag{1.17}$$

where $\vec{e}$ represents the polarisation vector of the electromagnetic field, $\vec{q}$ its wave vector, and e, $\vec{p}$ and m_0 are the charge, momentum and mass of the electron.

1.2.2 3D structures

In bulk semiconductors, the wave function of an electronic state can be described in the Bloch form as: $\Phi_{i,\vec{k}}(\vec{r}) = \frac{1}{\sqrt{V}}e^{i\vec{k}.\vec{r}}u_{i,\vec{k}}(\vec{r})$ with V the crystal volume, $\vec{k}$ the wave vector of the electron or hole and $u_{i,\vec{k}}$ the periodic part of the Bloch function.

The calculation of the matrix elements for an electron transition from the valence band to the conduction band writes:

$$\left|\left\langle \Phi_{c,\vec{k}}(\vec{r})\left|H_{int}\right|\Phi_{v,\vec{k'}}(\vec{r})\right\rangle\right|^2 = \left(\frac{eE_0}{2m_0\omega}\right)^2 \left|\left\langle u_{c,\vec{k}}\left|\vec{e}.\vec{p}\right| u_{v,\vec{k'}}\right\rangle\right|^2 \delta_{(\vec{k'},\vec{k}+\vec{q})}. \tag{1.18}$$

The Kronecker delta $\delta(\vec{k'}, \vec{k}+\vec{q})$ ensures the conservation of the wave vector. A summary of the transition matrix elements for both ZB and WZ materials for different polarisation states of the exciting radiation are reported in table 1.6 (at the end of this chapter).

In all the experiments presented here the excitation light propagates parallel to the growth direction ($\vec{k} \| Oz$) which in the case of WZ semiconductors it corresponds to the crystal c axis. Taking into account the conservation of the angular momentum, the allowed optical transitions under right-circularly or left-circularly polarised light (σ^+,σ^-) in ZB and WZ bulk semiconductors are summarised in figures 1.8 (a) and (b) respectively.

Figure 1.8 (a) shows that at $\vec{k}$=0 under a right-circularly polarised excitation (σ^+) of energy equal to the band gap $E_{exc} = E_G$ the possible optical transitions consist of 3 electrons from the heavy hole sub-band ($|3/2\rangle$) to the CB state $|-1/2\rangle$ and 1 electron from the light hole sub-band ($|1/2\rangle$) to state $|1/2\rangle$. The resulting CB electron polarisation is defined as:

$$P_e = \frac{n_+ - n_-}{n_+ + n_-},$$

where n_+ and n_- are respectively the CB electron densities of spin-up (+1/2) and spin-down (-1/2) electron. The maximum achievable spin polarisation is therefore P_e=50%. In a simplified picture, when the excitation energy is larger than $E_G+\Delta_{SO}$, two more electron transitions to the CB state $|-1/2\rangle$ can arise from the split-off band. The total CB spin polarisation in now reduced to 0% [1]. We can therefore state that in order to efficiently create a CB spin polarisation in ZB-type semiconductors the light excitation energy must be chosen in the range $E_G \leqslant E_{exc} \leqslant E_G+\Delta_{SO}$. As an example, in GaAs the spin orbit interaction energy is $\Delta_{SO} = 340$ meV [13] whereas in ZB GaN it is relatively small $\Delta_{SO} \sim 17$ meV [6]. This leaves a narrow energy window to efficiently create a CB spin polarisation in ZB nitride compounds.

For WZ-type bulk semiconductors (figure 1.8 (b)), the two highest valence sub-bands are not degenerated at $\vec{k} = \vec{0}$. A CB spin polarisation can be created by selectively exciting the A sub-band with circularly polarised light ($\sigma^\pm$). Concerning the B and C bands, the relative weight for the optical transition are given by the coefficient α^2 and β^2 which vary from material to material and depend on the lattice crystal field and constraint. From the diagram reported in figure 1.8, we can infer that the available excitation range for obtaining a sizeable CB spin polarisation is $E_G \leqslant E_{exc} \leqslant E_G + \Delta_{AB}$.

These selection rules are equally applicable for the emission process: the spin properties of the recombining carriers can be deduced from the analysis of the photoluminescence polarisation.

3D exciton selection rules: The selection rules described above present the

---

[1] This simple description does not take into account the $\vec{k}$ dispersion of the valence sub-bands which makes the variation of the photo created CB spin polarisation a complicated function of the excitation energy in which the joint density of states of the transitions between conduction-valence band pairs take part [12].

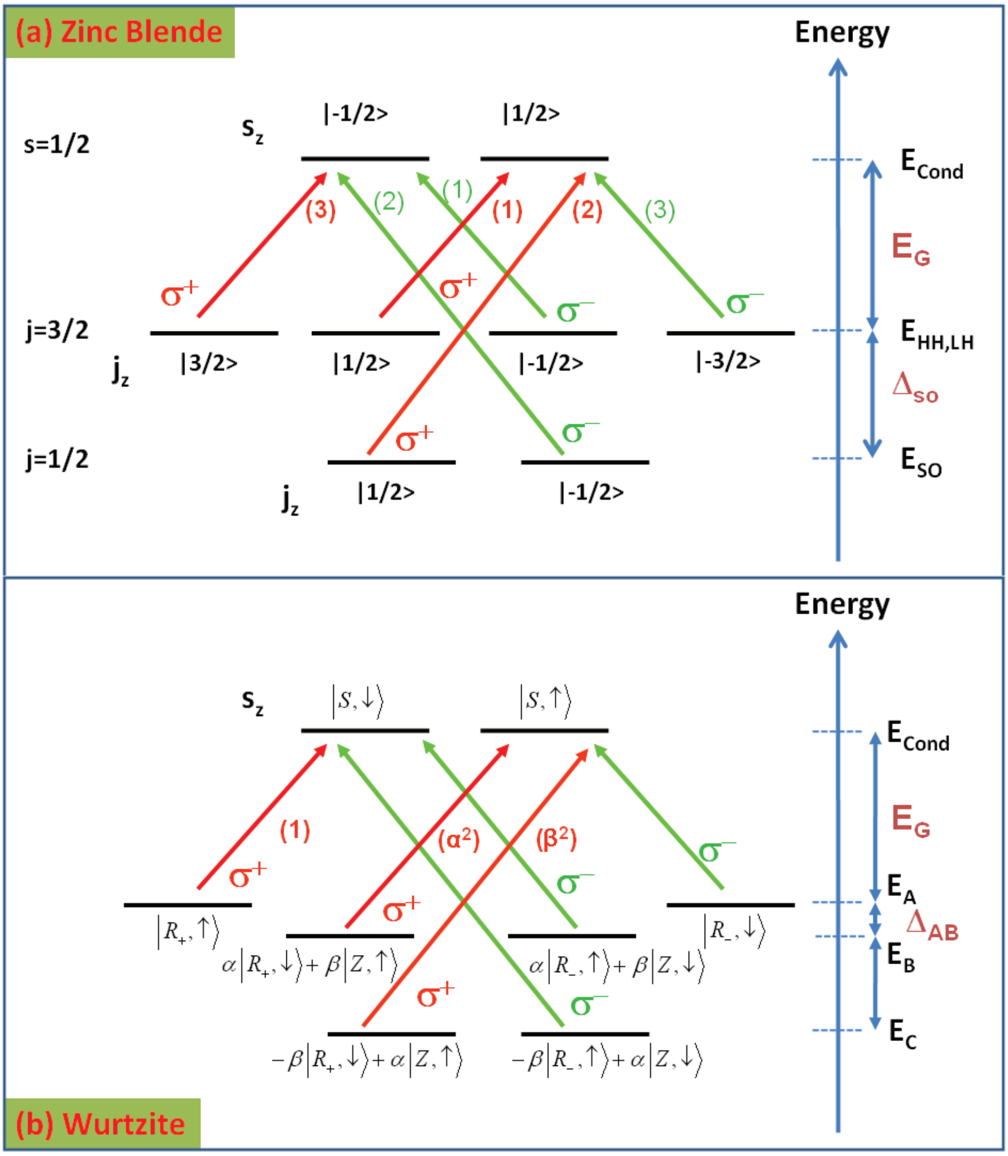

Figure 1.8: *The selection rules of the electronic transitions at $\vec{k} = 0$ under circular excitation $\sigma^{\pm}$ of (a) ZB and (b) WZ bulk semiconductors. The values in the parentheses show the relative intensity of the corresponding transitions. The states in the valence band are presented in the hole formalism.*

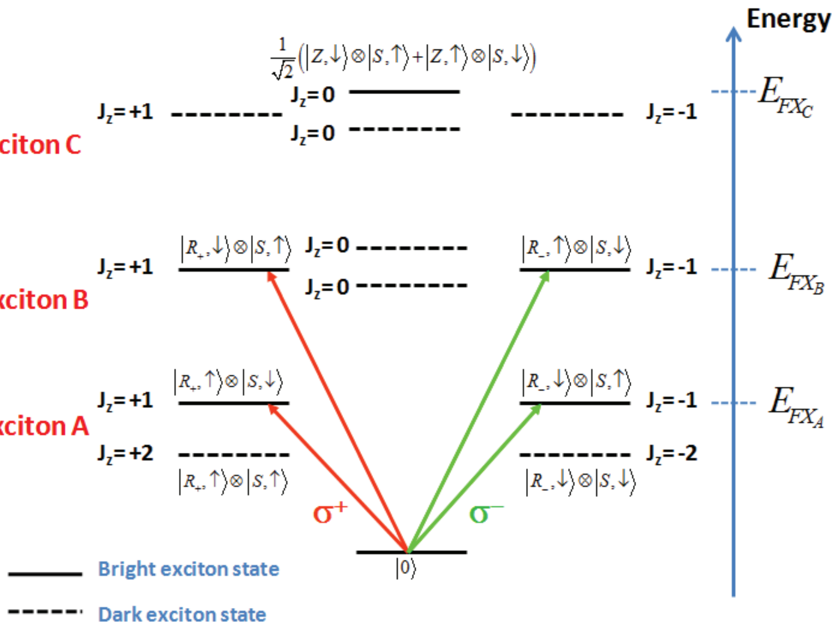

Figure 1.9: *The selection rules of the excitonic transitions at* $\vec{k} = 0$ *corresponding to the circular excitation of bulk WZ semiconductors. The excitation light propagates along the c axis. For the sake of simplicity, we have assumed* $|R_+\rangle = -|X+iY\rangle/\sqrt{2}, |R_-\rangle = |X-iY\rangle/\sqrt{2}$ *and* $\alpha^2 \gg \beta^2$.

simple picture of a band-to-band recombination. Due to the importance of excitonic effects in wide-gap nitride materials, the exciton selection rules have to be considered. Figure 1.9 presents the exciton optical selection rules in the case of a WZ semiconductor such as GaN.

Due to the presence of excitonic effects, the absorption in a semiconductor can begin at energies below the band gap, notably in the range $(E_G - E^b_{ex,n}) < E_{photon} < E_G$. If the exciting light is circularly polarised ($\sigma^\pm$) the photons carry a momentum ±1 directed along the propagation direction. Due to the angular momentum conservation rules, only the excitonic states which have a projection of the total angular momentum $J_z = s_{z,e} + j_{z,h} = \pm 1$ can couple to light. It results that heavy-hole excitons or A excitons (for ZB or WZ materials respectively) characterised by an angular momentum $J_z = \pm 1$ are optically active or bright excitons while the states of total angular momentum $J_z = \pm 2$ are inactive or dark excitons. Similarly, the states of light-hole exciton (ZB) or exciton B (WZ) with $J_z = \pm 1$ are active while the states with $J_z = 0$ are inactive.

In a simple description, the oscillator strength of the transition is proportional to $|\rho_{n,l,m}(0)|^2$, the square of the wave function of the relative motion between the electron and the hole.

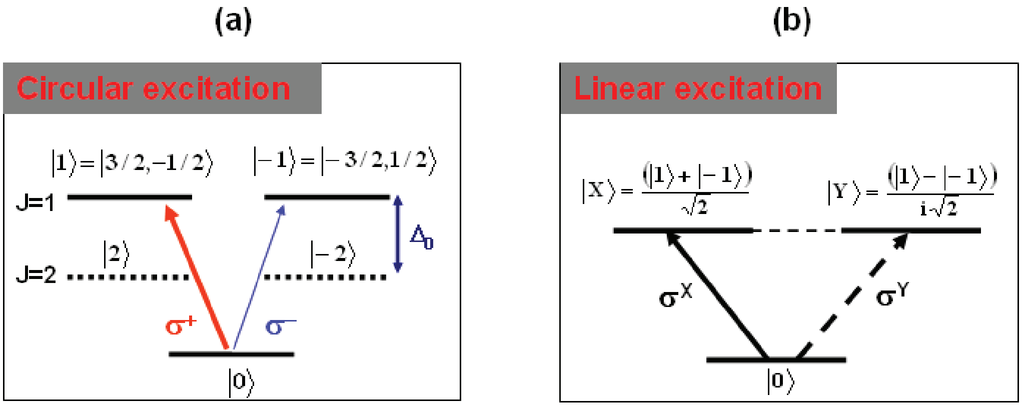

Figure 1.10: *The selection rules at* $\vec{k} = 0$ *in quantum wells corresponding to (a) circular and (b) linear excitations.*

1.2.3 2D structures

The transition probabilities in quantum wells can be calculated similarly to the bulk case. In the 2D case, however, the wavefunctions are more conveniently described in the framework of the envelope function formalism. The resulting electric-dipole matrix elements give similar selection rules as presented in figure 1.8 for bulk materials.

In a ZB quantum well, the confinement lifts the degeneracy between the heavy and light holes at the center of the Brillouin zone ($\vec{k}_\perp = 0$). By exciting the system with circularly polarised light ($\sigma^\pm$) of proper energy, we can selectively excite excitonic states with a definite total angular momentum projection $|1,+1\rangle$, $|1,-1\rangle$ (figure 1.10 (a)).

It is obviously possible to excite heavy hole excitons with linearly polarised light (σ^X or σ^Y): being the excitation of two circularly polarised lights with opposite helicity, a coherent superposition of $J_z = \pm 1$ excitons is created according to the direction of the linear polarisation of the excitation:

$$|X\rangle = \frac{|+1\rangle + |-1\rangle}{\sqrt{2}} \text{ or } |Y\rangle = \frac{|+1\rangle - |-1\rangle}{i\sqrt{2}}.$$

The selection rules applicable in this situation are presented in figure 1.10 (b). The resulting photo-generated excitons are *aligned* to the direction of the electric field of the excitation light: this phenomenon is accordingly denoted *the optical alignment of excitons*.

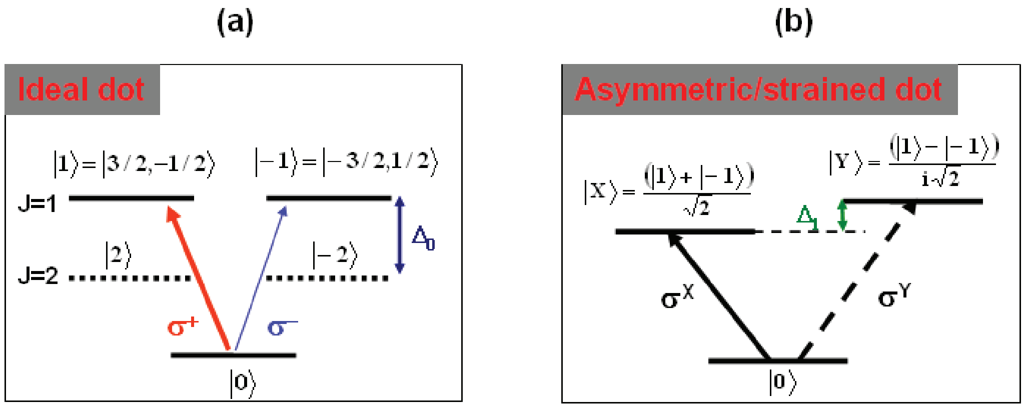

Figure 1.11: *The selection rules at* $\vec{k} = 0$ *corresponding to (a) an ideal and (b) an asymmetric and/or strained quantum dot.*

1.2.4 0D structures

The calculation of the transition probabilities for excitons in quantum dots presents several additional difficulties compared to bulk and 2D systems. On one hand, the actual exciton fine structure depends on the real potential confining the carriers in the dot. On the other hand the potential itself depends on the shape, interface and constraint of the dots, which may vary sensibly from dot to dot.

The exciton fine structure in the QDs depends thus from the symmetry of the considered system [18]. A symmetry reduction causes an anisotropic exchange interaction for the electron-hole pair which in a quantum dot results in the mixing of the degenerate $|+1\rangle$ and $|-1\rangle$ eigenstates. The resulting eigenstates, separated in energy by the anisotropic exchange interaction energy Δ_1 writes:

$$|X\rangle = -\frac{|+1\rangle + |-1\rangle}{\sqrt{2}} \text{ or } |Y\rangle = -\frac{|+1\rangle - |-1\rangle}{i\sqrt{2}}.$$

The optical transitions engendered by these new exciton eigenstates are therefore linearly polarised, usually along the [110] and [1$\bar{1}$0] in ZB semiconductors. Figure 1.11 schematically presents the exciton fine structure and optical selection rules occurring in an "ideal" and "real" quantum dot.

The origins of the anisotropic exchange interaction is still debated. Two main factors have been anyway identified despite their respective weigh on Δ_1 is unknown. The first one is the spatial elongation of QDs in one given direction [19]. The second is the reduction of the symmetry due to the interfaces which breaks the roto-inversion symmetry operation [19, 34].

In the GaAs/AlGaAs or InAs/GaAs QD systems, the values of the anisotropic electron-hole exchange interaction (Δ_1) are relatively small, ranging from 50 to 100

μeV [19,33,45]. In contrast, in GaN/AlN single QD, Kindel *et. al* observed very large anisotropic electron-hole exchange interaction energies $\Delta_1 = 1 - 7$ meV depending on the size of the QDs [35]. This originates mainly from the stronger exciton binding energy and stronger overlap of electrons and holes in WZ structures.

1.3 Spin relaxation mechanisms

The spin relaxation is the process that brings back to the equilibrium condition a non-equilibrium spin population [12, 13]. In this section we will briefly present the main spin relaxation mechanisms occurring in semiconductors: Elliott-Yafet (EY), Dyakonov-Perel (DP), Bir-Aronov-Pikus (BAP) and hyperfine interaction.

1.3.1 Elliott-Yafet mechanism

The Elliott-Yafet (EY) mechanism is due to the mixing of the opposite electron spins' states in the conduction band for $\vec{k} \neq 0$ induced by the spin-orbit interaction. The electronic states therefore are not pure spin states and consequently any process causing the scattering of a CB electron from a wave vector $\vec{k}$ to a different $\vec{k'}$ state can also lead to spin relaxation. The spin relaxation time (τ_s) is in this case proportional to the scattering time τ_p of the electron momentum according to:

$$\frac{1}{\tau_s(E_k)} \cong \left(\frac{\Delta_{SO}}{E_g + \Delta_{SO}}\right)^2 \left(\frac{E_k}{E_g}\right)^2 \frac{1}{\tau_p(E_k)}. \tag{1.19}$$

This equation shows that the EY mechanism is important for small-gap semiconductors with large spin-orbit splitting (GaAs, InSb), whereas it is strongly reduced for wide-gap materials such as GaN.

1.3.2 D'yakonov-Perel mechanism

The D'yakonov-Perel (DP) mechanism is an efficient spin relaxation process for III-V and II-VI semiconductors proposed by Dyaknov and Perel in 1971 [24]. Due to the lack of inversion symmetry in III-V and II-VI type semiconductors (the elementary cell contains 2 different atoms in these compounds), the conduction band degeneracy for spin $|+1/2\rangle$ and $|-1/2\rangle$ electronic states is lifted. As a consequence, the spin splitting induced by this inversion asymmetry can be described by an intrinsic $\vec{k}$-dependent effective magnetic field $\vec{B}(\vec{k})$ induced by the spin-orbit coupling (see figure 1.12 for a 3D system).

The corresponding Hamiltonian of an electron in the conduction band can be

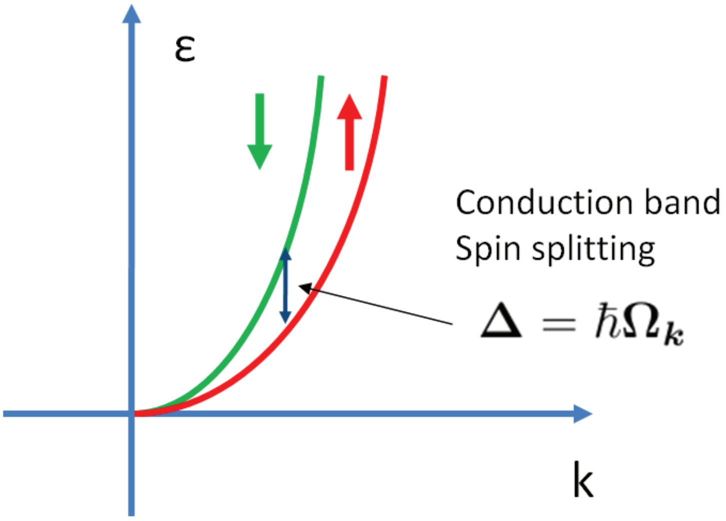

Figure 1.12: *Sketch of the conduction band spin splitting induced by the spin-orbit coupling in a bulk semiconductor.*

cast in the form :

$$H(k) = \frac{\hbar}{2}\boldsymbol{\vec{\sigma}} \cdot \boldsymbol{\vec{\Omega}(\vec{k})}, \tag{1.20}$$

where $\vec{\sigma}$ are the Pauli matrices and $\vec{\Omega}(\vec{k})$ is the Larmor frequency of the electron spin precession around the effective magnetic field which is defined as $\vec{\Omega}(\vec{k}) = g_e^* \frac{|e|}{m} \vec{B}(\vec{k})$. Figure 1.13 illustrates the precession of electron spin around the effective spin-orbit field $\vec{\Omega}(\vec{k})$. A scattering event modifying the electron wave vector from $\vec{k}$ to $\vec{k'}$ leads the electron spin to precess around a different effective field $\vec{\Omega}(\vec{k'})$.

It is intuitive to see that the momentum scattering time influences the spin relaxation in the DP mechanism. In particular, two regimes can be distinguished by the interplay between the average precession frequency $\overline{\Omega}$ and the momentum scattering time τ_p:

1. Weak scattering regime ($\overline{\Omega} \cdot \tau_p > 1$) : the electron spin precesses more than one full cycle about the effective field before the scattering event occurs. In this case, the spin relaxation time is proportional to the momentum scattering time:

$$T_{s1} \sim \tau_p. \tag{1.21}$$

2. Strong scattering regime ($\overline{\Omega} \cdot \tau_p < 1$) : the electron scatters faster than a full precession of the spin. In this case, the spin-orbit field is characterized by rapid fluctuations and contrary to the previous regime, the spin relaxation time is now inversely proportional to the momentum scattering time:

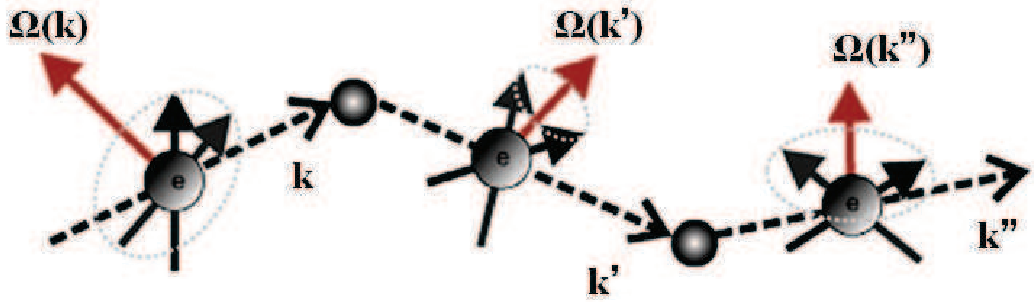

Figure 1.13: *Sketch of the Dyakonov-Perel mechanism [26].*

$$\frac{1}{T_{s1}} \sim \overline{\Omega}_{\perp}^{2} \cdot \tau_p, \tag{1.22}$$

in which, $\overline{\Omega}_{\perp}$ is the average of the projection of Ω on the plane orthogonal to the observed average spin component. This regime is also referred to as "motional-narrowing" regime. This regime is the most common situation encountered in III-V and II-VI bulk or nano-structured semiconductors.

The EY and DP mechanisms usually coexist in systems lacking inversion symmetry, their relative strengths depending on many factors. In general, the DP mechanism becomes more relevant with increasing the band-gap energy and with the temperature. This mechanism often dominates in III-V semiconductors and 2D structures.

1.3.3 Bir-Aronov-Pikus mechanism

In addition to the previous spin relaxation mechanisms, the Bir-Aronov-Pikus (BAP) [25] process is an electron spin relaxation mechanism induced by the exchange interaction between electrons and holes. The associated Hamiltonian is given by :

$$H_{BAP} = A\vec{\boldsymbol{S}} \cdot \vec{\boldsymbol{J}}\delta(\vec{\boldsymbol{r}}), \tag{1.23}$$

where A is a factor proportional to exchange integral between electrons and holes, $\vec{J}$ is total angular momentum operator for holes, $\vec{S}$ is the electron spin operator and $\vec{r}$ is the relative position of electron and hole. The BAP-type mechanism is important for excitons [28] as well as for p-doped semiconductors with a large hole concentration at low temperatures. In p-doped semiconductor heterostructures, the resident holes are unpolarised in thermal equilibrium and the exchange interaction simultaneously flips the electron and hole spin states. The spin relaxation time can be calculated as follow [27]:

$$\frac{1}{T_{s1}} = \frac{2}{\tau_0} N_a a_B^3 \frac{v_k}{v_B}[\frac{p}{N_a}|\psi(0)|^4 + \frac{5}{3}\frac{N_a - p}{N_a}], \tag{1.24}$$

for non degenerated holes. In the above equation, a_B is the exciton Bohr radius, p is the density of free holes and τ_0 is an exchange splitting parameter defined as $\hbar/\tau_0 = (3\pi/64)\Delta_{ex}^2/E_B$ in which Δ_{ex} is the exchange splitting of the excitonic ground state, E_B is Bohr exciton energy; $v_B = \hbar/m_c a_B$, v_k is the electron velocity, and $|\psi(0)|^2$ is the Sommefeld factor.

If holes are degenerate, the spin relaxation time is given by :

$$\frac{1}{T_{s1}} = \frac{3}{\tau_0} p a_B^3 \frac{v_k}{v_B} \frac{k_B T}{E_{Fh}}, \tag{1.25}$$

where E_{Fh} is the hole Fermi energy and v_k is the electron velocity.

1.3.4 Hyperfine-interaction mechanism

The hyperfine interaction is a mutual interaction between the magnetic momenta of electron and nuclei. It is a mechanism characterized by the fact that both electron and nuclear spins relax through their mutual magnetic field. The spins of the lattice nuclei, normally randomly oriented, create a correspondingly random effective magnetic field that impacts on the electron spins causing their relaxation. Usually this interaction is quite weak for free electrons in bulk materials and quantum wells but it plays an important role for localised electrons (for example in quantum dots).

For s-type electrons, the Hamiltonian describing the interaction between an electron spin $\vec{S}$ and a nuclear spins $\vec{I}$ is mainly due to the Fermi-contact contribution which is written as [27]:

$$H_{hf} = \frac{\mu_0}{4\pi} \frac{8}{3} \pi g_0 \mu_B \sum_i \gamma_{n,i} \hbar \vec{I}_i \cdot \vec{S} \delta(\boldsymbol{r} - \boldsymbol{R_i}),$$

where μ_0 is the vacuum permeability, $g_0 = 2.0023$ is the g-factor of free electrons, μ_B is Bohr magnetron, $\gamma_{n,i}$ is the nuclear gyro-magnetic ratio, $\mathbf{r}$ is the relative coordinate related to the nucleus, $\mathbf{i}$ is the label for nuclei at positions $\boldsymbol{R_i}$, $\boldsymbol{S}$ and $\boldsymbol{I_i}$ the electron and nuclear spin operators respectively. The spin relaxation time caused by this interaction is calculated through the rate of mutual spin flips between two spin systems: electron state $|k\uparrow\rangle$ and nuclear state $|I,\mu\rangle$ to respectively $|k\downarrow\rangle$ and $|I,\mu+1\rangle$ [13].

1.3.5 Exciton's spin relaxation mechanism

The exciton spin relaxation mechanism has been described by Maialle *et al.* [28] while investigating III-V quantum wells. In this mechanism, both electron spin and hole spin relax simultaneously (relaxation of two particles) instead of the relaxation of only one particle at a time. The Hamiltonian for the exciton writes:

$$H_{exciton} = H_0 + H_{exch},$$

in which $H_{exciton}, H_0, H_{exch}$ correspond respectively to the Hamiltonians of the heavy-hole exciton, of the exciton at ground state, and of the long-range exchange interaction [26, 28, 29]. We have:

$$H_0 = \begin{pmatrix} E(K_G) & 0 \\ 0 & E(K_G) \end{pmatrix}$$

and

$$H_{exch} = \vec{\Omega}(K_G).\vec{S}^{exciton} = \begin{pmatrix} 0 & \alpha(K_x - iK_y)^2 \\ \alpha(K_x + iK_y)^2 & 0 \end{pmatrix},$$

in which $K_G(K_x, K_y)$ is the in plane wave vector which is perpendicular to the observed average spin component (z axis). The Larmor frequency which corresponds to the long-range contribution to the electron-hole exchange is written as:

$$|\vec{\Omega}| = \alpha K_G^2, \tag{1.26}$$

in which, for $1s$ exciton:

$$\alpha = \frac{\hbar\Gamma_0}{2K_G q}, \qquad \Gamma_0 = \frac{2\pi q e^2 |\hat{\vec{v_{cv}}}|^2}{\hbar\varepsilon_\infty {\omega_0}^2} |\rho_{1s}(0)|^2 = \frac{1}{2\tau_r},$$
$$q \approx \sqrt{\varepsilon_\infty}\frac{\omega_0}{c}, \qquad \vec{v_{cv}} = \frac{\vec{p_{cv}}}{m_0}, \qquad \vec{p_{cv}} = \langle c|\vec{p}|v\rangle,$$

with τ_r the radiative 2D-exciton recombination time, $\hbar\omega_0$ the $1s$ exciton energy with respect to crystal ground state, $\vec{p_{cv}}$ the interband matrix element of the electron linear momentum.

From the previous expressions, we deduce the exciton spin relaxation time:

$$\begin{aligned} \frac{dS_z}{dt} &= -\frac{1}{T_z^{exciton}} S_z \\ \Rightarrow \qquad \frac{1}{T_z^{exciton}} &= \langle \Omega^2(K_G)\tau_2 \rangle. \end{aligned} \tag{1.27}$$

This equation has the same form as equation (1.22) for the DP mechanism. This mechanism is similar to DP mechanism by considering the electron-hole Coulomb exchange interaction as an effective magnetic field. This process involves the long-range interaction between electrons and holes.

Figure 1.14 illustrates the spin relaxation mechanism occurring for a heavy hole exciton [31]. Two processes are evidenced. The first one is the spin relaxation of one particle indicated by the relaxation time of an electron (τ_e) or hole spin (τ_h). In this process, the exciton changes from bright exciton states ($|\pm1\rangle$) to dark exciton states ($|\pm2\rangle$) and vice-versa. The second process is the exciton spin relaxation (τ_{exc}) in which an exciton is transformed from one bright state ($|\pm1\rangle$) to the other ($|\mp1\rangle$).

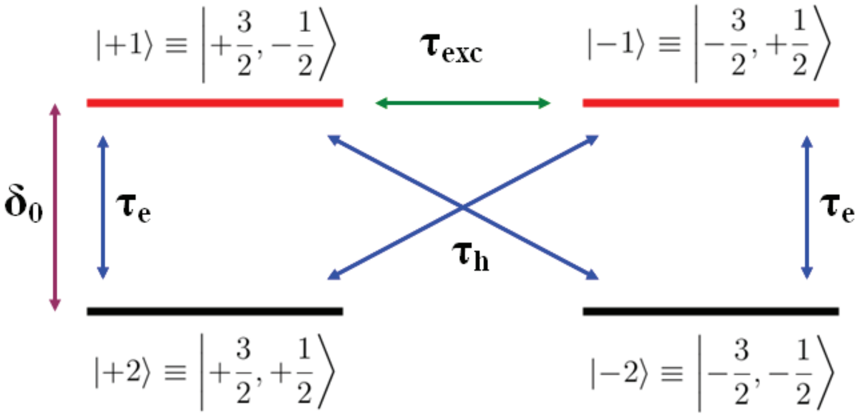

Figure 1.14: *Schematic representation of the different spin relaxation processes occurring for a heavy exciton.* τ_e, τ_h *and* τ_{exc} *are the corresponding relaxation times of the electron spin, the hole spin and the heavy-hole exciton spin.*

(a) Zince-blende				**(b) Wurtzite**			
$e - h_{HH}$	e//Ox	e//Oy	e//Oz	$e - h_A$	e//Ox	e//Oy	e//Oz
q//Ox	impossible	$1/2\Pi^2$	0	q//Ox	impossible	$1/2\Pi^2$	0
q//Oy	$1/2\Pi^2$	impossible	0	q//Oy	$1/2\Pi^2$	impossible	0
q//Oz	$1/2\Pi^2$	$1/2\Pi^2$	impossible	q//Oz	$1/2\Pi^2$	$1/2\Pi^2$	impossible
$e - h_{LH}$	e//Ox	e//Oy	e//Oz	$e - h_B$	e//Ox	e//Oy	e//Oz
q//Ox	impossible	$1/6\Pi^2$	$2/3\Pi^2$	q//Ox	impossible	$\alpha^2/2\Pi^2$	$\beta^2\Pi^2$
q//Oy	$1/6\Pi^2$	impossible	$2/3\Pi^2$	q//Oy	$\alpha^2/2\Pi^2$	impossible	$\beta^2\Pi^2$
q//Oz	$1/6\Pi^2$	$1/6\Pi^2$	impossible	q//Oz	$\alpha^2/2\Pi^2$	$\alpha^2/2\Pi^2$	impossible
$e - h_{SO}$	e//Ox	e//Oy	e//Oz	$e - h_C$	e//Ox	e//Oy	e//Oz
q//Ox	impossible	$1/3\Pi^2$	$1/3\Pi^2$	q//Ox	impossible	$\beta^2/2\Pi^2$	$\alpha^2\Pi^2$
q//Oy	$1/3\Pi^2$	impossible	$1/3\Pi^2$	q//Oy	$\beta^2/2\Pi^2$	impossible	$\alpha^2\Pi^2$
q//Oz	$1/3\Pi^2$	$1/3\Pi^2$	impossible	q//Oz	$\beta^2/2\Pi^2$	$\beta^2/2\Pi^2$	impossible

Table 1.6: *The selection rules for the transition between valence and conduction band at $\vec{k} = 0$ with a linearly polarised electromagnetic radiation with polarisation state $\vec{e}$ and wave vector $\vec{q}$ in (a) ZB and (b) WZ bulk semiconductor.* $\Pi^2 = E_p/(2m_0)$ *where E_p is the Kane energy of the considered semiconductor [9, 10].*

Bibliography

[1] Chin-Yu Yeh, Z. W. Lu, S. Froyen, and Alex Zunger, *Zinc-blend - Wurtzite polytympism in semiconductors*, Physical Review B **46**, 10086 (1992).

[2] Ya-Hong Xie et. al, *Towards Dislocation-free III-nitrides: Selective epitacy of GaN*, Semiconductor Materials Research Lab, UCLA.
http://www.seas.ucla.edu/smrl/GaN.html

[3] D. Strauch, *GaAs: Lattice parameters*, Landolt-Börnstein - Group III Condensed Matter Volume **44D**, pp 169-172 (2011).

[4] Electronic archive: *New semiconductor materials Characteristic and Properties*, Copyright 1998-2001 by Ioffe Institute.
http://www.ioffe.ru/SVA/NSM/Semicond/GaAs/basic.html

[5] Electronic archive: *New semiconductor materials Characteristic and Properties*, Copyright 1998-2001 by Ioffe Institute.
http://www.ioffe.ru/SVA/NSM/Semicond/GaAs/bandstr.html

[6] I. Vurgaftman and J. R. Meyer, *Band parameters for nitrogen-containing semiconductors*, Journal of Applied Physics **94**, 3675 (2003).

[7] Christophe Wilhelm, Alexandre Larrue, Xing Dai, Dmitri Migas and Cesare Soci, *Anisotropic photonic properties of III–V nanowires in the zinc-blende and wurtzite phase*, Nanoscale **4**, 1446 (2012).

[8] Grank Glas, Jean-Christophe Harmand, and Gilles Patriarche, *Why does wurtzite form in nanowires of III-V zinc-blend semiconductors*, Physical Review Letters **99**, 146101 (2007).

[9] G. Bastard, *Wave mechanics applied to semiconductor heterostructures*, Physical version (1992).

[10] Richard Planel, *Pumpage optique des polaritons excitoniques dans CdS et CdSe: Contribution à l'étude du biexciton dans CdS*, PhD thesis, University of Paris VII, Paris (1977).

[11] Delphine Largarde, *Dynamique de spin dans des structures semiconductrices à base de ZnO et de GaN*, PhD thesis, INSA, Toulouse (2008).

[12] F.Meier and B.O. Zakharchenya, *Optical orientation*, North Holland, Amsterdam, (1984).

[13] Mikhail I. Dyakonov, *Spin Physics in Semiconductors*, Springer series in Solid State Sciences **157** (2008).

[14] G. Lampel, *Nuclear Dynamic Polarization by Optical Electronic Saturation and Optical Pumping in Semiconductors*, Physical Review Letters **20**, 491, (1968).

[15] J. Frenkel, *On the transformation of light into heat in solids. II*, Physical Review **37**, 1276 (1931).

[16] Benjamin Lax, Laura M.Roth and Solomon Zwerdling, *Theory of optical magneto absorption effects in semiconductors*. Physical Review, **114**, 90 (1959).

[17] G. H. Wannier, *The structure of electronic excitation levels in insulating crystals*, Physical Review **52**, 191 (1937).

[18] E. L. Ivchenko, *Fine Structure of Excitonic Levels in SC Nanostructures*, Physica Status Solidi (a) **164**, 487 (1997).

[19] D. Gammon, E. S. Snow, B. V. Shanabrook, D. S. Katzer, and D. Park, *Fine Structure Splitting in the Optical Spectra of Single GaAs Quantum Dots*, Physical Review Letters **76**, 3005 (1996).

[20] M. Bayer, A. Kuther, A. Forchel, A. Gorbunov, V. B. Timofeev, F. Schafer, J. O. Reithmaier, T. L. Reinecke, and S. N. Walck, *Electron and hole g-factors and exchange interaction from studies of the exciton fine structure in* $In_{0.60}Ga_{0.40}As$ *quantum dots*. Physical Review Letters **82**, 1748 (1999).

[21] Helmut Foll, *Semiconductors I*, © Prof. Dr. Helmut Foll, AMAT, Faculty of Engineering, University of Kiel.
http://www.tf.uni-kiel.de/matwis/amat/semi_en/kap_5/advanced/t5_1_3.html.

[22] W. Ekardt, K. Losch, and D. Bimberg, *Determination of the analytical and the nonanalytical part of the exchange interaction of InP and GaAs from polariton spectra in intermediate magnetic fields*, Physical Review B **20**, 3303 (1979).

[23] M. Julier, J. Campo, B. Gil, J. P. Lascaray, and S. Nakamura, *Determination of the spin-exchange interaction constant in wurtzite GaN*, Physical Review B **57**, R6791 (1998).

[24] M.I. Dyakonov and V.I. Perel, *Possibility of orienting electron spins with current*, Journal of Experimental and Theoretical Physics Letters **13**, 657 (1971).

[25] G. L. Bir, A. G. Aronov, and G. E. Pikus, *Spin relaxation of electrons due to scattering by holes*, Journal of Experimental and Theoretical Physics **42**, 705 (1975).

[26] T.Kohn, *Time-resolved studies of electron and hole spin dynamics in modulation-doped GaAs/AlGaAs quantum wells*, Physic Reports **494**, 415 (2010).

[27] Jaroslav Fabian, Igor Zutic and S.Das Sarma, *Spintronics : Fundamentals and applications*, Review of Modern Physics, **76**, 323 (2004).

[28] M. J. Maialle, E. A. de Andrada e Silva, and L. J. Sham, *Exciton spin dynamics in quantum wells*, Physical Review B **47**, 15776 (1993).

[29] F. Tassone, F. Bassani, and L. C. Andreani, *Quantum-well reflectivity and exciton-polariton dispersion*, Physical Review B **45**, 6023 (1992).

[30] S. V. Gupalov, E. L. Ivchenko, and A. V. Kavokin, *Fine structure of localized exciton levels in quantum wells* Journal of Experimental and Theoretical Physics **86**, 388 (1998).

[31] A. Vinattieri, Jagdeep Shah, T. C. Damen, D. S. Kim, L. N. Pfeiffer, M. Z. Maialle and L. J. Sham, *Exciton dynamics in GaAs quantum wells under resonant excitation*, Physical Review B, **50**, 10868 (1994).

[32] J. Tersoff, *Theory of semiconductor heterojunctions: the role of quantum dipoles*, Physical Review B **30**, 8 (1984).

[33] Mathieu Paillard, *Dynamics of spin relaxation in the self-assembled InAs/GaAs quantum dots*, PhD Thesis, INSA, Toulouse (2001).

[34] Mathieu Senes, *Dynamique de spin des excitons neutres ou chargés dans les boites quantiques InAs/GaAs*, PhD Thesis, INSA, Toulouse (2004).

[35] C. Kindel, S. Kako, T. Kawano, H. Oishi, Y. Arakawa, G. Hönig, M. Winkelnkemper, A. Schliwa, A. Hoffmann, and D. Bimberg, *Exciton fine-structure splitting in GaN/AlN quantum dots*, Physical Review B **81**, R241309 (2010).

Chapter 2

Experimental set-ups

Contents

2.1 Time resolved photoluminescence spectroscopy 37
  2.1.1 Excitation source 37
  2.1.2 Frequency doubling and tripling 40
  2.1.3 Streak camera detection 42
  2.1.4 Spectral and temporal resolution 44
  2.1.5 Polarisation resolution 45
  2.1.6 Cooling system 46
2.2 Stationary Photoluminescence set-up 47
2.3 Magnetic fields 47
Bibliography 49

The invention of laser in 1960 [1] made photoluminescence (PL) spectroscopy become a powerful technique for material characterization and the investigation of the electronic and optical processes occurring in semiconductors [2]. The use of pulsed sources makes it possible to monitor photoluminescence intensity as a function of time. Thanks to the advent of ultrafast laser sources, time-resolved photoluminescence has became one of the most widely used technique to probe phenomena occurring on the picosecond or femtosecond time scale [2]. The purpose of this chapter is to introduce the photoluminescence spectroscopy set-ups used in this work. First, we introduce the picosecond time- and polarisation-resolved experiment. Then, a description of the continuous wave photoluminescence set-up used to demonstrate some of the the spin dependent recombination phenomena in ion implanted InGaAs layers and dilute nitride, will follow.

2.1 Time resolved photoluminescence spectroscopy

The principle of the Time Resolved PhotoLuminescence (TRPL) experimental set-up is shown in figure 2.1.

A picosecond pulse coming from the Ti:Sapphire laser, whose polarisation can be adjusted by optical waveplate elements, is used to excite the sample. A polarising cube sets the reference linear polarisation. A $\lambda/4$ is subsequently used to modify the polarisation into circular right or left. Alternatively, a $\lambda/2$ waveplate is employed in order to generate a linearly polarised beam rotated by a definite angle with respect to the reference one. A 10 cm plano-convex lens focuses afterwards the laser light to a $\approx$ 50 μm spot diameter onto the sample surface previously mounted onto the cold finger of a closed-cycle helium cryostat. The luminescence signal emitted from the sample is collimated, then its polarisation analysed before being dispersed by an imaging spectrometer. A streak camera finally performs the temporal resolution and the final spectrum of the chosen polarisation, resolved both in time and in energy, is recorded by a charge coupled device (CCD camera) interfaced to a computer. The different elements composing the experimental set-up will be described in detail below.

2.1.1 Excitation source

The main excitation source in our experiment is a mode-locked Titanium-Sapphire (Ti:Sa) laser pumped by a continuous wave (CW) Coherent VERDI-V10 laser.

The Coherent Verdi V-10 laser (the pump-laser Nd:YVO_4 in figure 2.1) is a solid-state diode-pumped frequency-doubled laser system which can generate up to 10 W CW optical power at 532 nm. The scheme of the pump laser is shown in figure 2.2. This pump laser uses a Nd:YVO_4 (Neodymium Doped Yttrium Orthvanadate) crystal as an amplifying medium with an absorption at 809 nm and emission at 1064 nm. This crystal is pumped by two laser diode arrays placed in a mono-mode cavity. The emission wavelength at 532 nm used to pump the Ti:Sapphire laser is achieved by doubling the fundamental frequency (1064 nm) thanks to the presence of an intra-cavity LBO (Lithium Triborate LiB_3O_5) crystal. The stability of the VERDI laser output power is controlled by feedback circuitry acting on the crystal temperature and output power.

The Ti:Sapphire laser (figure 2.1) active medium is a titanium ion-doped sapphire crystal with the characteristics of both being wavelength tunable (between 680 to 1050 nm) and working in the pulsed regime. The crystal is produced by introducing Ti_2O_3 into a melt of Al_2O_3 [8] which causes the substitution of a small percentage

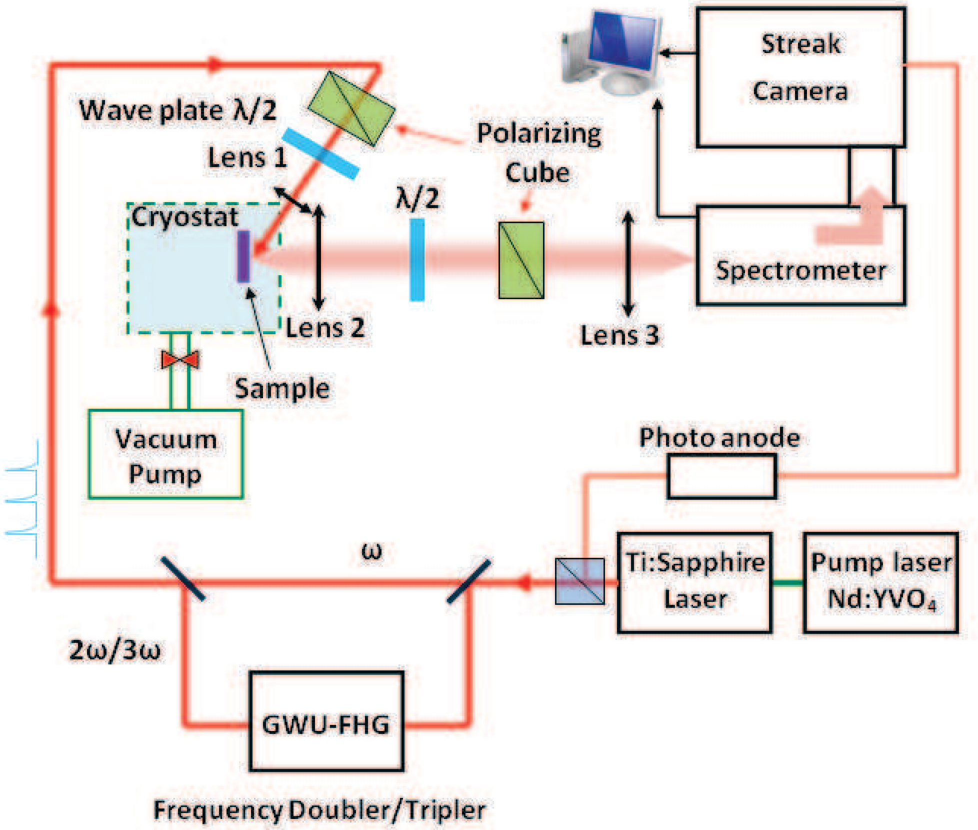

Figure 2.1: *The time- and polarisation-resolved photoluminescence setup.*

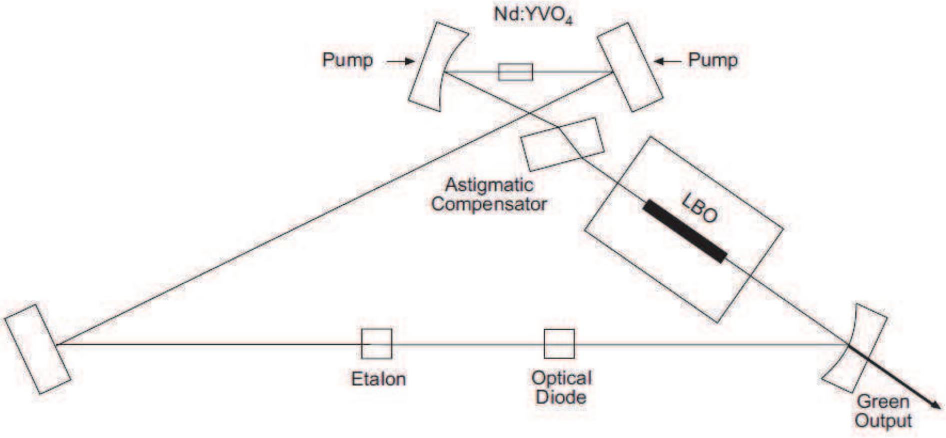

Figure 2.2: *The layout of the Nd:YVO_4 laser head optical cavity [4].*

of Al^{3+} ions by Ti^{3+}. The electronic ground state of Ti^{3+} ions is then split into a pair of vibrationally broadened levels making possible the wide tuning range of this laser [3] as shown in figure 2.3(a). The absorption and fluorescence spectra of a typical Ti:Sapphire crystal are shown in figure 2.3 (b).

Although the fluorescence band extends from wavelengths in the range from 600 to 1050 nm, the lasing action is only possible at wavelengths longer than 680 nm because the long-wavelength part of the absorption band overlaps the short-wavelength part of the fluorescence spectrum. The tuning range is further reduced by an additional weak absorption band that overlaps the fluorescence spectrum. This band is accounted for by the presence of Ti^{4+} ions, but it is also dependent on material growth techniques and Ti^{3+} concentration. Additionally, the tuning range is affected also by mirror coatings, tuning element losses, pump power, environmental absorption (both oxygen and water vapours) and pump mode quality.

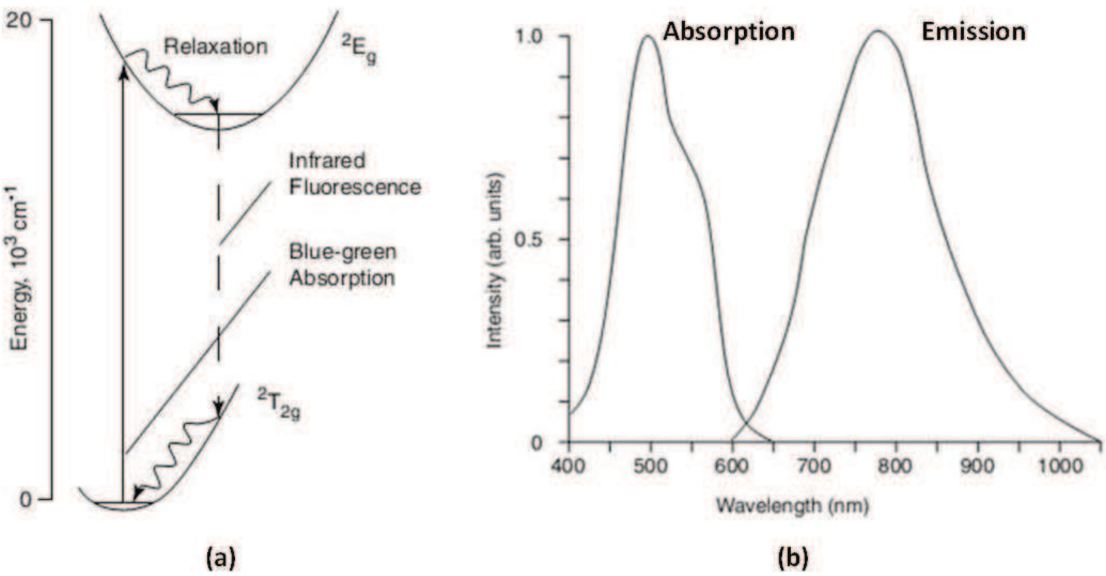

Figure 2.3: *Ti:Sapphire characteristics: (a) Energy level structure of the Ti^{3+} vibrational levels; (b) Absorption and emission spectra of Ti:sapphire* [3].

The Ti:Sa laser can operate in pulsed regime with the repetition rate of 80 Mhz in two modes : (i) femtosecond mode generating 100 fs long pulses; (ii) picosecond mode generating a pulse duration of about 1.5 ps. In our experiment, the picosecond mode is utilised due to the good compromise between two required parameters : spectral width and time resolution. For our experiments the picosecond pulse spectral width ≈ 1.2 meV ensures a good selectivity in quasi-resonant excitation while the pulse width (1.5 ps) is sufficient for the analysis of the dynamical phenomena studied in this work.

The mode-locking technique used to achieve pulsed laser operation relies on self-phase modulation and Kerr effects in the Ti:Sapphire crystal. The longitudinal optical modes in the laser cavity are synchronised by optical Kerr effect in the crystal. Due to non-uniform power density distribution of the laser beam characterised by a Gaussian distribution, the refractive index of the crystal changes across the transverse beam profile; this makes the crystal act as a converging lens. This refractive index variation is responsible for the nonlinear optical effects of self-focusing and self-phase modulation. As a result, the pulse length is further shrunk to attain higher field strength at the center of the optical pulse and the modes of the cavity are locked. In order to start the pulsed operation, an acousto-optical modulator synchronised with the laser pulse is placed in the cavity. While the beam travels along the cavity, the dispersion of group velocity needs to be compensated in order to maintain the desired pulsed operation. This compensation is obtained by a Gires-Tournois Interferometer (GTI) installed in the totally reflecting mirror plate of the cavity. The GTI provides the necessary wavelength dispersion variation to ensure that different modes composing the output laser pulse are put back into phase at each cavity round-trip. Finally, the lasing wavelength is selected by a narrow tunable bandpass birefringence optical filter (Lyot filter). The main characteristics of Ti:Sa laser are summarised in table 2.1.

Repetition Frequency	Spectral Range	Average Power	Pulse Energy	Pulse Duration	Spectral Width
80 MHz	680-1050 nm	0.4-2 W	5-25 nJ	1.2-1.8 ps	$\approx$ 1.2 meV

Table 2.1: *Picosecond Ti:Sapphire laser main characteristics.*

2.1.2 Frequency doubling and tripling

As mentioned in section 2.1.1, the wavelength range covered by the Ti:Sa laser is limited to 680-1050 nm. To investigate the dynamics of the interband transitions of wide bandgap semiconductors such as the AlGaN/GaN heterostructures used in this work, a pulsed light source in the UV range (300-380 nm) is necessary. Moreover, the ability to finely tune the excitation wavelength is a crucial point in our optical orientation experiments. To this purpose, a Spectra Physics GWU-FHG Flexible Harmonic Generator has been installed after the Ti:Sa laser in order to double or triple its frequency to reach the desired UV spectral region (figure 2.4a). In particular, for frequency doubling, a LBO (Lithium triborate - LiB_3O_4) crystal is used, whereas a β-BBO (Barium Borat - β-BaB_2O_4) one is installed for frequency

	Wavelength range	Average power	Pulse duration
Doubler	340-470 nm	40-200 mW	< 2 ps
Tripler	260-310 nm	0.2-10 mW	< 2 ps

Table 2.2: *Characteristics of the GWU-FHG frequency doubler/tripler.*

tripling. The characteristics of the laser pulses typically generated are listed in table 2.2.

Frequency doubling: The principle is presented in figure 2.4 (b). The frequency doubling, or second harmonic generation, is a nonlinear optical process exploiting the second order term of the LBO susceptibility $\chi^{(2)}$ to generate the second harmonics of the incident laser. In non centro-symmetric crystals, the incident beam at frequency ω polarises the system. The polarisation presents high order harmonic terms which in turn radiate a coherent light particularly at frequency 2ω provided that phase matching condition is full filled. This process requires both the energy and wave vector conservation conditions to be satisfied. The latter writes:

$$\vec{k}_{2\omega} = 2\vec{k}_{\omega} \tag{2.1}$$

in which $k_{\omega} = n(\omega)\omega/c$ and $k_{2\omega} = n(2\omega)2\omega/c$ where $n(\omega)/n(2\omega)$ are the refractive indexes of the non linear crystal at respectively the fundamental/double frequency and c is the speed of light. This condition can be therefore restated as:

$$n(2\omega) = n(\omega). \tag{2.2}$$

This particular condition is achieved by taking advantage of the birefringence of the LBO crystal. The pump beam (ω) coming from the Ti:Sa laser is focused with the appropriate linear polarisation direction onto the LBO crystal as the ”ordinary” beam. The frequency-doubled signal will then emerges as the ”extraordinary” beam at frequency 2ω. This is a special case of the frequency sum generation [7]. Finally, the efficiency of the frequency doubling critically depends also on the crystal thickness.

Frequency tripling: The principle of frequency tripling (3ω) performed by the β-BBO crystal is shown in figure 2.4 (c). In this case, the fundamental frequency (ω) is mixed with the the second harmonic one (2ω). To obtain a third harmonic signal, in addition to the energy and momentum conservation rules, the fundamental and second harmonic beams must strictly overlap both in space and time. This last condition is achieved by acting on the mechanical delay line (retarder line - figure 2.4 (a)) which adjust the optical path of the frequency-doubled beam to match the

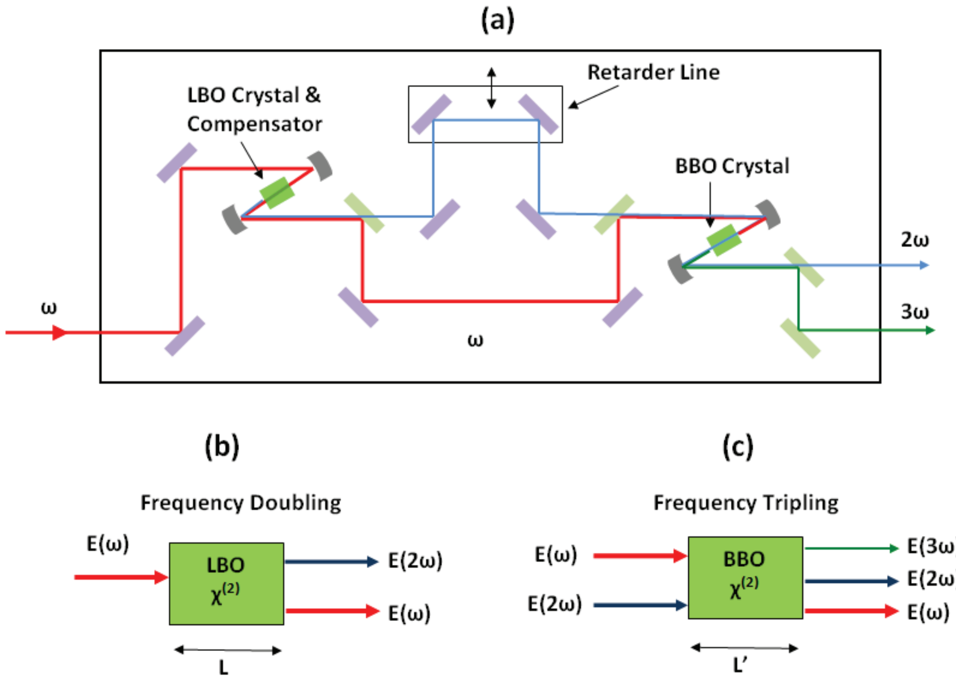

Figure 2.4: *(a) The schematic set-up of the Flexible Harmonic Generator used to double/triple the Ti:sapphire fundamental frequency. (b) The schematic representation of the frequency doubling using the LBO crystal and (c) of the frequency tripling using the BBO crystal.*

fundamental's one to ensure the simultaneity of the two beams in the non-linear crystal.

2.1.3 Streak camera detection

The streak camera is a device to measure ultra-fast light radiation phenomena delivering simultaneous information on the intensity as a function of time and spectral emission (or spatial position) [6]. The working principle of a streak camera is shown in figure 2.5(a) and can be summarised as follows: the train of emitted light pulses to be analysed is imaged with an optical system onto a photocathode where a slit defines the vertical extension of the beam. Light is converted, by photoelectric effect, into electrons which are ejected in a vacuum tube spatially and temporally separated according to the arrival time and horizontal (spectral) position of the light pulses striking the photocathode. The resulting flux of electrons replicates in time and position the original light pulse. After being accelerated, the electrons are sent into a deflection region constituted by two conductive plates. A very fast sweeping voltage is applied in this region, vertically deflecting the traversing electrons proportionally to their arrival time (figure 2.5b). A temporal light sequence is therefore converted into an electronic spatial one. The horizontal profile is however left unchanged. The final process consists in the impact of the time-resolved electron flux onto a phosphorous screen where the signal is converted back to photons and then recorded by a CCD camera. After the temporal resolution, an electron amplifier, a micro-channel plate, is inserted before the phosphorous screen to increase the brightness of the recorded image. The information stored in the measurement is therefore threefold: the horizontal axis represents the space coordinate (wavelength or position), the vertical axis the time coordinate, and the signal intensity is recovered from the phosphorous screen intensity (usually converted into a color code by the CCD software, figure 2.6).

The efficiency of the photo-conversion of light into electrons of a streak camera

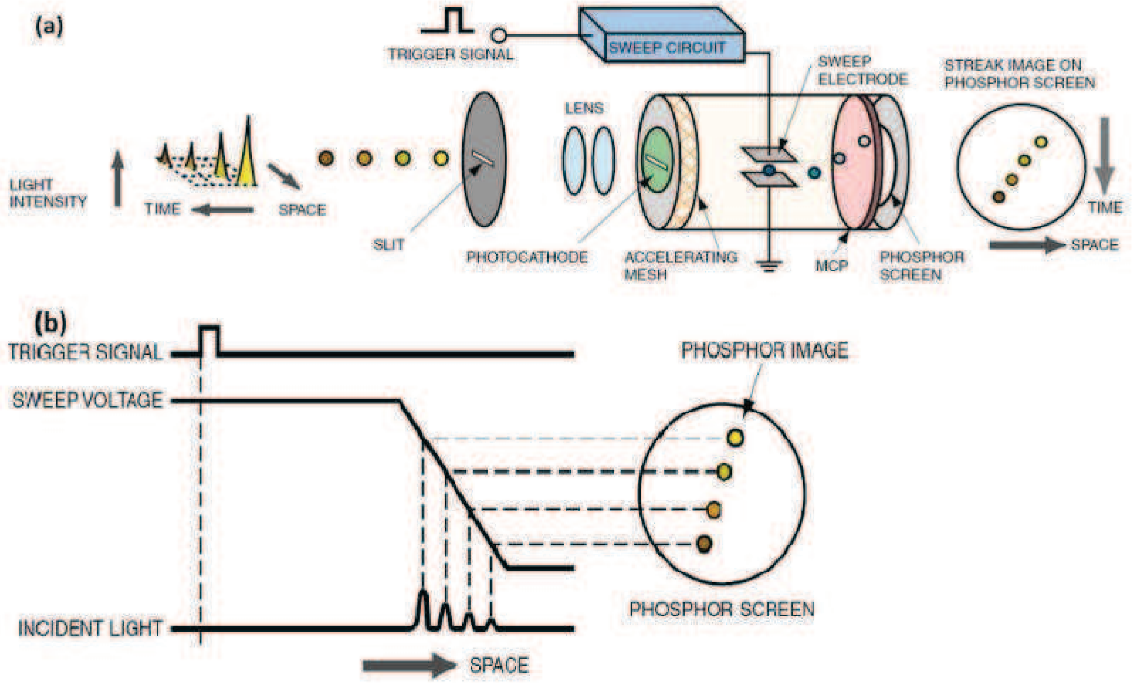

Figure 2.5: *(a) Operating Principle of a Streak Camera (b) Sweeping mechanism responsible for the time resolution.*

is a strongly variable function of the signal wavelength. Photocathodes optimised to the experiment wavelength range have to be properly chosen although the spectral band covered by each type of photo-cathode is relatively large (see figure 2.7). The spectral response of different photo-cathodes is usually identified by the S convention, S1 being the system of choice for near infrared detection and S20-25 the most widely used photo-cathode types for the UV to visible spectral range. In this work, two different and very distant spectral regions where addressed. The photoluminescence in the UV region (≈300 nm) emitted by the nitride quantum dots have been analysed with a S20 type photocathode synchroscan streak camera, whereas, the much longer wavelengths (850 to 1000 nm) relevant for the implanted InGaAs has been studied thanks to a synchroscan streak camera with an S1 type photocathode. The temporal operations modes of the streak cameras are listed in table 2.3.

Time range index	Temporal span (ps)	Time resolution (ps) using the 80 grooves/mm grating
1	157	5
2	809	8
3	1542	12
4	2263	17

Table 2.3: *Temporal mode and corresponding resolution of the S1 streak camera. This values are practically unchanged for the S20 type one.*

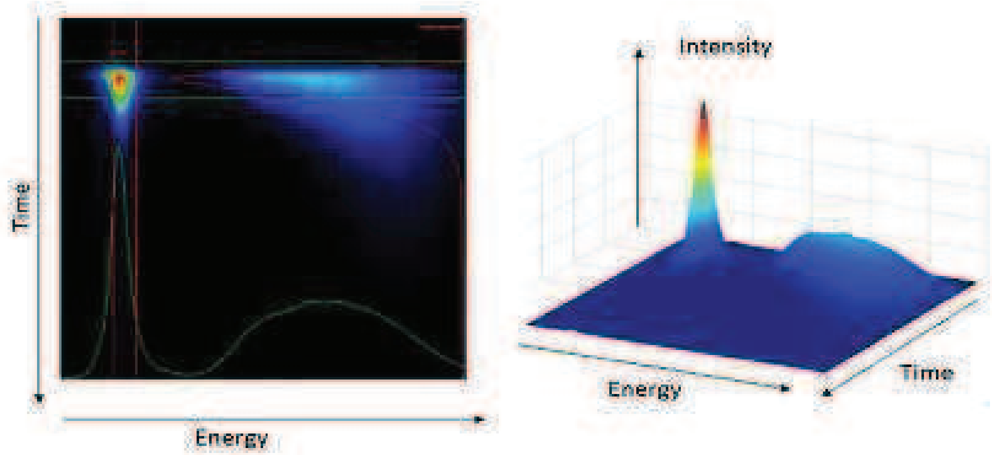

Figure 2.6: *Example of a streak camera image on time range 4 measured with a 80 grooves/mm grating.*

2.1.4 Spectral and temporal resolution

The spectral resolution for the infrared region is obtained thanks to a Jobin-Yvon Triax 320 imaging monochromator, placed in front of the streak camera and equipped with 3 gratings. For the UV region, the set-up is instead equipped with a triple grating iHR spectrometer. The characteristics of both systems are reported in table 2.4.

The intrinsic time resolution of the streak camera is about 2 ps. However, the effective time resolution depends on the whole detection system and in particular on

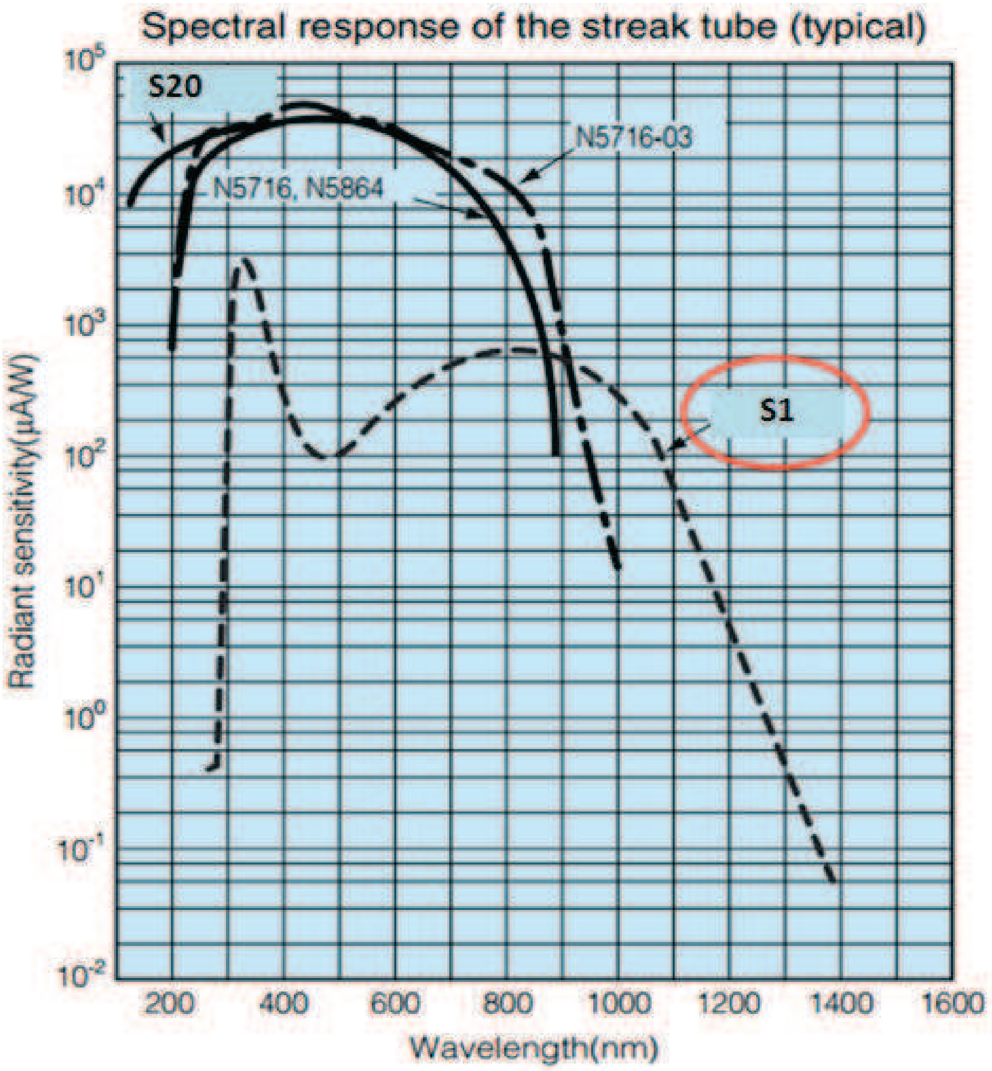

Figure 2.7: *Spectral sensitivity of different streak tubes.*

the wavelength dispersion of the monochromator. A larger dispersion will produce a correspondingly larger optical path difference between the portion of light traveling on the side and on the central optical axis of the grating. A correspondingly temporal dispersion is generated. This can be minimised by placing a vertical slit inside the monochromator to reduce the lateral dimension of the beam with the drawback however of a reduced spectral resolution and sensitivity.

The synchroscan streak camera can be operated in 4 different time ranges whose characteristics (for the S1 type) are presented in table 2.3.

2.1.5 Polarisation resolution

In order to study the temporal evolution of the spin orientation of carriers in our structures, time and polarisation resolved photoluminescence experiments have been utilised. These consist in the detection of the degree of circular (or linear)

Spectrometer	Grating (grooves/nm)	Blaze (nm)	Spectral width (nm)	Dispersion (nm/nm)	Resolution (nm)
Triax 320	80	870	188.0	39.6	0.6
	300	1000	46.2	10.56	0.3
	600	400-1300	22.2	5.28	0.1
iHR320	100	450	170	28.2	0.7
	600	300	28	4.7	0.12
	1200	330	14	2.35	0.06

Table 2.4: *The characteristics of the Jobin-Yvon Triax 320 and iHR monochromators. The spectral resolution values are given for 200 μm and 80 μm widths of the entrance and exit slit respectively.*

polarisation of the photoluminescence emitted by a sample after a light excitation of a definite polarisation. The exciting laser polarisation can be adjusted from linear ($\sigma^{X,Y}$) to elliptical or circular ($\sigma^{+,-}$) by a Glan-Taylor polarising cube together with a quarter-waveplate whose neutral axis can be rotated (see figure 2.1). In order to excite the sample with a linear polarisation excitation rotated by an arbitrary angle, a $\lambda/2$ waveplate replaces the quarter-wave plate. The photoluminescence emitted from the sample is then analysed into its fundamental components (linear or circular) thanks to the use of an appropriate waveplate for the polarisation state chosen, together with a polarising cube, both placed in the optical path of the collimated photoluminescence beam. This polarisation-resolved signal is then focused onto the entrance slit of the monochromator.

The circular polarisation P_{circ} and linear polarisation P_{lin} degrees are respectively defined as :

$$P_{circ} = \frac{I^+ - I^-}{I^+ + I^-} \quad \text{and} \quad P_{lin} = \frac{I^X - I^Y}{I^X + I^Y} \tag{2.3}$$

where I^+,I^- (I^X,I^Y) are the components of the photoluminescence intensities co- and counter-polarised with the circular (linear) excitation σ^+ (σ^X).

2.1.6 Cooling system

To perform measurements at low temperatures, the samples are placed into a closed-cycle Helium cryostat. The sample is mounted at the end of a cold finger fixed inside a vacuum chamber with a typical pressure of 10^{-6} Torr. The chamber is fitted with glass windows for optical access. The temperature in the cryostat can be continuously varied from 4K to 300K and it is stabilised by a PID controller.

2.2 Stationary Photoluminescence set-up

In order to highlight some of the specific features of the spin dependent recombination in dilute nitrides, no PL time resolution is needed. Namely, the much stronger PL total intensity emitted under a circular polarisation excitation compared to a linear one and the PL intensity increase under an appropriate external magnetic field have been measured with a stationary PL set-up. In order to speed-up the data acquisition, a silicon photodiode (Thorlabs FDS1010) coupled to a long-pass filter has replaced the system composed by the monochromator and the streak camera. In order to improve the sensitivity of the system a standard lock-in technique has been employed.

2.3 Magnetic fields

Some of the measurements performed in this work require the application of weak magnetic fields (< 500 mT) in Farady geometry (magnetic field direction parallel to the photo-created electron spins). A permanent magnet delivering up to 650 mT and placed behind the sample has been used to provide the necessary field.

Bibliography

[1] Anthony E. Siegman, *Lasers*, University Science Books, *page 1* (1986).

[2] Jagdeep Shah, *Ultrafast spectroscopy of Semiconductors and Nanostructures*, Springer series in Solid State Sciences, 2^{nd} edtion, 1999.

[3] Spectra Physics, *Tsunami: Mode-locked Ti:Sapphire Laser User's Manual*, page 3-2, Spectra Physics, 2002.

[4] COHERENT Inc., *Operator's manula* $Verdi^{TM}$ *V-8/V-10 Diode-Pumped Lasers*, page 2-3, COHERENT Inc., 51400 Parick Henry Drive, Santa Clara, CA 95054.

[5] Spectra-Physics, GWU-FHG Flexcible Harmonic Generator *Preliminary User's Manual*, Spectra-Physics 1335 Terra Bella Avenue, Mountain View, CA 94043, June 1998.

[6] HAMAMATSU, *Guide to Streak Camera*, page 3, HAMAMATSU PHOTONICS K.K., Systems Division, Cat.No.SHSS0006E01, APR/2008 (2008.2) IP, Printed in Japan.

[7] Frits Zernike and John E. Midwinter, *Applied Nonlinear Optics*, Wiley-Interscience Publication (1973).

[8] P. F. Moulton, Journal of the Optical Society of Ameria B **3**, No. 1, 125 (January 1986).

Chapter 3

Spin dynamics in nanowire-embedded GaN quantum dots

Contents

3.1 Introduction 53

3.1.1 Wide bandgap semiconductor (In)GaN 53

3.1.2 GaN nanowires 53

3.2 Spin properties of GaN based structures: state of the arts 55

3.2.1 Bulk GaN 55

3.2.2 Nanostructured GaN 56

3.3 Spin dynamics of nanowire-embedded GaN quantum dots 60

3.3.1 Sample and experimental configuration 60

3.3.2 Exciton photoluminescence polarisation of GaN/AlN nanowire QDs: spectral dependence 62

3.3.3 Exciton photoluminescence polarisation of GaN/AlN nanowire QDs: angular dependence 65

3.3.4 Exciton photoluminescence polarisation of GaN/AlN nanowire QDs: dynamics 69

3.3.5 Theoretical model 72

3.4 Conclusion 78

Bibliography 79

GaN-based nanostructures have proved to be an interesting semiconductor system for spin related applications due to their weak spin-orbit coupling, large exciton binding energy and tri-dimensional spatial confinement. These nanostructures have also showed a high potential [18, 19] to be a very a robust system for storing the information by means of exciton spin polarisation. Despite these demonstrations, the high density of defects and dislocations due to the lack of proper substrates still affect the growth of (Al)GaN materials, hampering both their optical and spin properties as the temperature increases.

Recently, nanowires embedded GaN/AlN Quantum Dots (QDs) has provided with a valid alternative to more common self assembled nanostructures [27–29], allowing for the investigation of the exciton spin properties in a novel system with fewer dislocations, or other defects, near the dot site. The better optical properties and the enhanced exciton polarisation characteristics expected for this material system have been the main motivations behind this work.

This chapter focuses on the polarisation properties of nanowire-embedded GaN/AlN quantum dots and is organised as follows. We will first make an overview of recently published results on the spin properties of GaN-based compounds. We will then present the experimental results obtained during this work. By means of detailed time-resolved optical orientation experiments we evidence the quenching of the exciton spin relaxation process from cryogenic up to room temperatures. We will demonstrate that the spin relaxation properties originate from the optical alignment of the exciton and that these properties can be conserved unaltered up to room temperature. This temperature insensitivity of the exciton linear polarisation markedly contrasts with previous observations in nitride-based self-assembled Stranski-Krastanov (SK) Quantum Dots and constitutes the principal result of this chapter. Finally, we will present the density matrix approach developed to account for the experimental observations.

3.1 Introduction

3.1.1 Wide bandgap semiconductor (In)GaN

Wide gap (In)GaN and its alloys are considered to be a very successful and versatile system for a variety of optoelectronics applications ranging from light emission (lasers or light-emitting diodes) [1–6] to photovoltaic conversion devices [7]. More recently GaN has emerged as well as a suitable material system for controlling and manipulating the electron spin up to room temperature [8–11, 14] thanks to its very low spin-orbit coupling (17 meV for wutzite GaN compared to 340 meV for GaAs - table 1.4) and wide band-gap (3.475 eV 10K compared to 1.519 ev for GaAs) [15–17]. In addition, thanks to its strong exciton binding energy GaN could also be considered as a suitable candidate for investigating the exciton spin properties up to room temperature. The tri-dimensional confinement obtained in nanostructures like quantum dots or nanoparticles is expected to further improve the stability of the carriers' spin memory by reducing the effectiveness of the wave vector dependent spin scattering mechanisms [15].

Nevertheless, the lack of a suitable natural substrate causes a high density of defects and dislocations in the epitaxial layers affecting both the optical and spin properties of the structures as showed by Brimont *et al.* [22]. Most of GaN-based devices are made from multiple epitaxial layers grown on either sapphire, SiC or diamond. These substrate are not only expensive but also hard to process. Another growth technique based on silicon wafers, readily available at relatively low cost, represents only a partial solution to the problem due to the lattice mismatch and the thermal expansion coefficient difference. Extensive defects and even dense microcracks may be generated in GaN layers grown on silicon substrates. These defects and cracks act as nonradiative and scattering centers for light propagation and electron transport. Nevertheless, this approach is the subject of an intense research due to the importance of developing future mixed photonic-electronic devices for integration in silicon based microelectronics circuits.

3.1.2 GaN nanowires

An effective solution to decrease the substrate-related defect density has been provided by the growth of GaN nanowires on (111) silicon or sapphire substrates [30–34]. Different growth techniques are today employed to fabricate GaN nanowires. Thanks to a collaboration with B. Gayral of the Néel institute in Grenoble, in this work we investigated AlN/GaN nanostructures grown on GaN nanowires by plasma assisted molecular beam epitaxy (PAMBE) without catalyst [30,31]. This technique

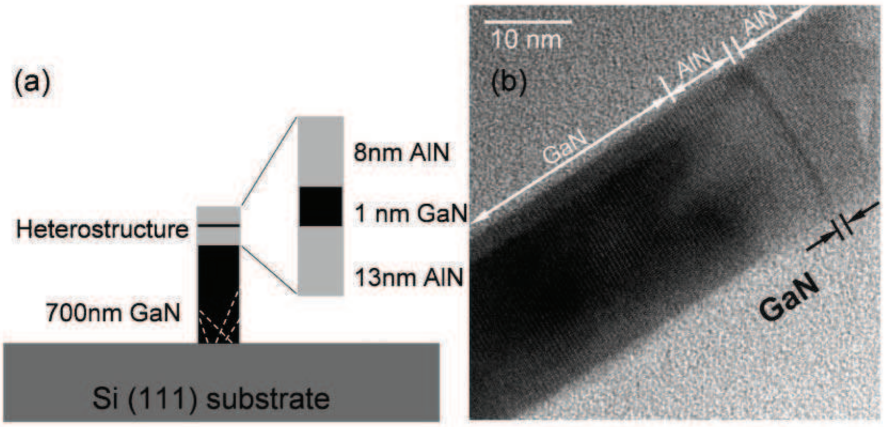

Figure 3.1: *(a) Schematic illustration of typical GaN/AlN inclusions on the top of a GaN nanowire grown on Si (111) substrate. The broken white lines schematically represent the propagation of substrate-induced defects which can relax through the nanowire surface before the dots are grown. (b) HRTEM image of a single GaN/AlN inclusion. The GaN "quantum dot" embedded in nanowire has a disk-like shape ∼ 1 nm thick and ∼ 30 nm wide surrounded by an AlN matrix [29].*

exploit a coincidence in the lattice parameters between the silicon (111) and the wurtzite GaN lattices [55] (see figure 3.2(a)) which favors, under N-rich conditions, the growth of wurtzite GaN nanowires with the *c* axis perpendicular to the substrate. We will show later in the chapter that this nanowire orientation is the crucial point which makes possible the carrier spin dynamics in this structures. The growth of GaN as nanowires allows for the reduction of the internal strain caused by the lattice mismatch (figure 3.1) and make it possible to achieve high crystal quality in III-N materials [30, 31]. A schematic representation of a nanowire-based nanostructure is reported in figure 3.1(a). Due to the large surface/volume ratio, surface relaxation of strains is allowed to occur before the structure of interest (AlN/GaN quantum dot in our case) is grown. This allows to overcome the limitations occurring in the case of SK quantum dots [27].

Figure 3.2(b) reports the temperature dependence of the PL decay time and integrated intensity as a function of the temperature measured by Renards *et al.* [29]. The PL decay time has a negligible variation as a function of the temperature, while the integrated PL intensity decreases of only a factor of two. These results are consistent with the very good quality that can be achieved in nanowire embedded nanostructures.

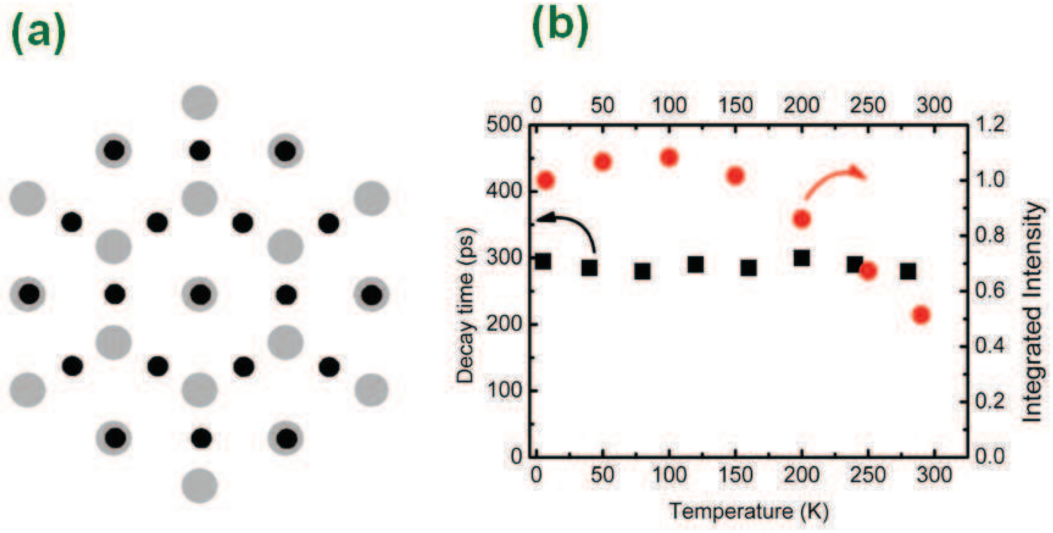

Figure 3.2: *(a) Schematic illustration of the Si (grey) and GaN (black) lattices in the coincidence orientation [55]. (b) Temperature dependence of the photoluminescence decay time and integrated intensity as afunciton of the temperature for an ensemble of GaN/AlN nanowire-embedded quatum dots [28].*

3.2 Spin properties of GaN based structures: state of the arts

Despite the strong potentialities in terms of control of the carrier spin in wide gap nitride semiconductors, only a few experimental investigations have been performed up to date in this system. Before presenting our experimental results, this section is devoted to a concise summary of the latest published works on the spin dynamics of GaN-based compounds with particular emphasis on the results concerning the GaN-based nanostructures.

3.2.1 Bulk GaN

As described in the previous sections, thanks to the weak spin-orbit couping and wide band-gap GaN represents a good candidate for long electron spin relaxation time. This has indeed been predicted by Krishnamurthy *et al.* by their comparative study of the electron spin relaxation time in bulk zinc-blende GaN [35, 36]. Their model shows that a three order of magnitude increase in the electron spin relaxation time is to be expected compared to GaAs mainly owing to the strongly reduced spin-orbit coupling energy. Beschoten *et al.* [8] have measured the electron spin relaxation time of n-doped wurtzite GaN by time-resolved Faraday rotation. They measured an electron spin coherence time $T_2^* \approx 20$ ns at T=20 K. More recently Buß *et al.* have extensively studied the electron spin relaxation time in both intrinsic and n-doped wurtzite and cubic samples [11–13]. They highlighted the role of the additional spin relaxation mechanism due to the intrinsic wurtzite structure inversion asymmetry which introduces k-linear terms in the D'yakonov-Perel (DP) conduction band spin splitting analogue to the Rashba effect. By time resolved Kerr rotation measurements they evidenced a room temperature electron spin relation time $\tau_s^{WZ} \approx 50$ ps in wurtzite structures (Fig 3.3 (a)) whereas $\tau_s^{ZB} \approx 500$ps in cubic GaN (Fig 3.3 (b)). Their interpretation, based on the DP mechanism as the major contribution to the electron spin relaxation time, is in good agreement with the experimental results. Buß *et al.* have also investigated the possibility to slow down the electron spin relaxation by localization on defects in Ga ion implanted samples [10] in an approach which closely resembles the results presented in the next chapter for creating paramagnetic centres in ion implanted GaAs. An increase up to a factor of 20 is observed for the localised electron spin relaxation time at 80 K for an increasing implantation dose.

Concerning the hole, its spin relaxation time has been experimentally measured in p-doped wurtzite GaN by the Kerr rotation technique [10]. The authors have measured the low temperature hole spin precession under an external magnetic field leading to a spin decoherence time $T_2^{h,*} \approx 120$ ps, considerably shorter than the corresponding value for the electron due to the strong valence band mixing for $\vec{k} \neq 0$. Several groups have reported on the spin relaxation time of the free exciton in wurtzite GaN. All experimental results agree with a sub-picosecond relaxation time [20–24], at least one order of magnitude shorter compared to other III-V semiconductors. Although the earlier interpretations of Ishiguro *et al.* [21] considered the Bir-Aronov-Pikus mechanism as the principal spin relation mechanism of excitons due to the strong electron-hole exchange interaction in wide-gap nitride materials, several groups agree on considering the Elliot-Yafet process as the main spin scattering mechanism due to the large defect density compared to GaAs.

However, D. Jena [25] theoretically predicted that at large dislocation densities charge transport will be degraded, while the spin relaxation time, dominated by D'yakonov-Perel mechanism, will conversely increase due to the enhanced motional narrowing effect.

3.2.2 Nanostructured GaN

A few experimental results have been published on the spin dynamics in wide-gap nitride quantum wells, essentially on InGaN/GaN -based structures. Exciton

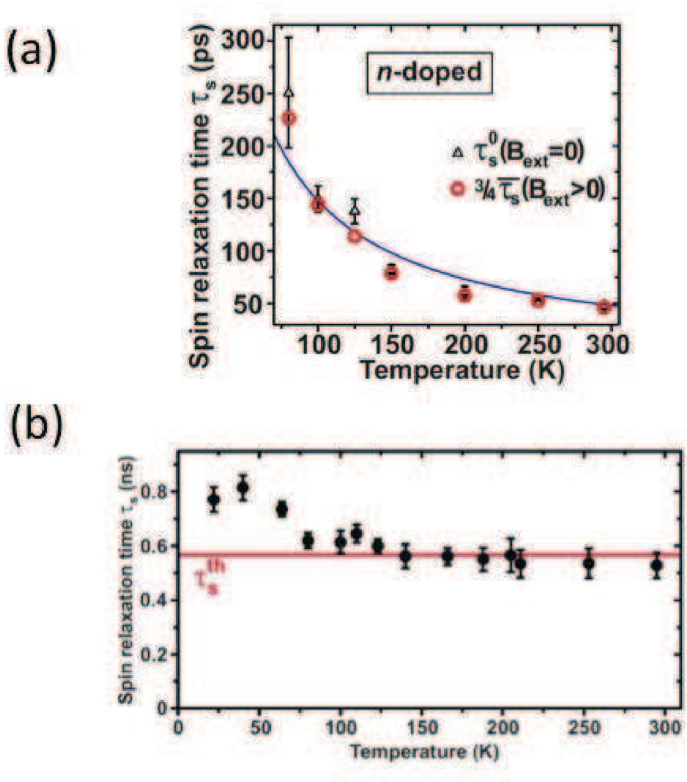

Figure 3.3: *Temperature dependence of the electron spin relaxation time in (a) wurtzite GaN. The different symbols indicates the spin relaxation time measured with and without an external magnetic field in Voigt geometry. The different values are due to the anisotropic nature of the Dyakonv-Perel spin relaxation mechanism intrinsic to the wurtzite structure [11]. (b) Cubic GaN [12]. The horizontal line corresponds to the calculated electron spin relaxation time based on the Dyakonv-Perel mechanism.*

spin relaxation times of the order of 100 ps have been for example measured by time resolved photoluminescence and differential reflectivity [37–39]. In [38] the authors underpin the role of the localisation induced by the introduction of In as the origin of the longer exciton spin relaxation time. The role of the strong piezoelectric field is however not discussed. The theoretical work of Harmon *et al.* [40] proposes instead an approach to control the electron spin relaxation in wurtzite GaN quantum wells identical to what experimentally proved by our group for (111) AlGaAs/GaAs [41]. The principle relies on the particular symmetry of the wurtzite structure for which the contributions to the conduction band spin splitting (confinement energy and electric field), at the origin of the DP electron spin relaxation mechanism, can be canceled in first approximation by a proper choice of the quantum well width and barrier offset [40].

Previous works in our group have investigated the exciton spin dynamics in SK wide-gap nitride quantum dots [18, 19]. As described in section (1.2.4) the exciton structure in quantum dots is influenced by the actual symmetry of the system [56]. A symmetry reduction manifests itself in an anisotropic electron-hole exchange interaction in the plane perpendicular to the growth axis due to the long range electron-hole Coulomb interaction at the origin of the longitudinal-transverse splitting of the exciton. In quantum dots this anisotropy induces a mixing of the degenerate bright exciton states (heavy hole exciton states in our case) to produce two new states of ”linear polarisation symmetry” and separated by an anisotropic exchange energy Δ_1. Lagarde *et al*. [18] have measured the optical alignment of the exciton in zinc-blende GaN/AlN dots up to room temperature, while Sénès *et al*. [19] have demonstrated the control of the exciton linear polarisation degree through the application of an external electrical bias in a wurtzite InGaN/GaN p-i-n QD structure.

Both works have highlighted the very long relaxation time of the exciton linear polarisation degree (greater than 10 ns) as measured under quasi-resonant excitation. Figure 3.4 reports the experimentally determined exciton linear polarisation degree as a function of the temperature in these works. A constant (during a time longer than the exciton life-time) exciton polarisation is measured at any temperature. This has been linked to the strength of the anisotropic exchange interaction which in turn results partly from the robustness of the exciton binding energy of wide-gap nitrides quantum dots (as we shall see later in this chapter) [26]. The exciton linear polarisation dynamics behavior contrasts with what usually measured in other QD systems [46] based on InAs, CdTe, or CdSe semiconductor materials. In the latter systems the linear polarisation decay time, albeit longer than the exciton lifetime for T=10 K, rapidly decreases when the temperature increases by a few tens of Kelvin.

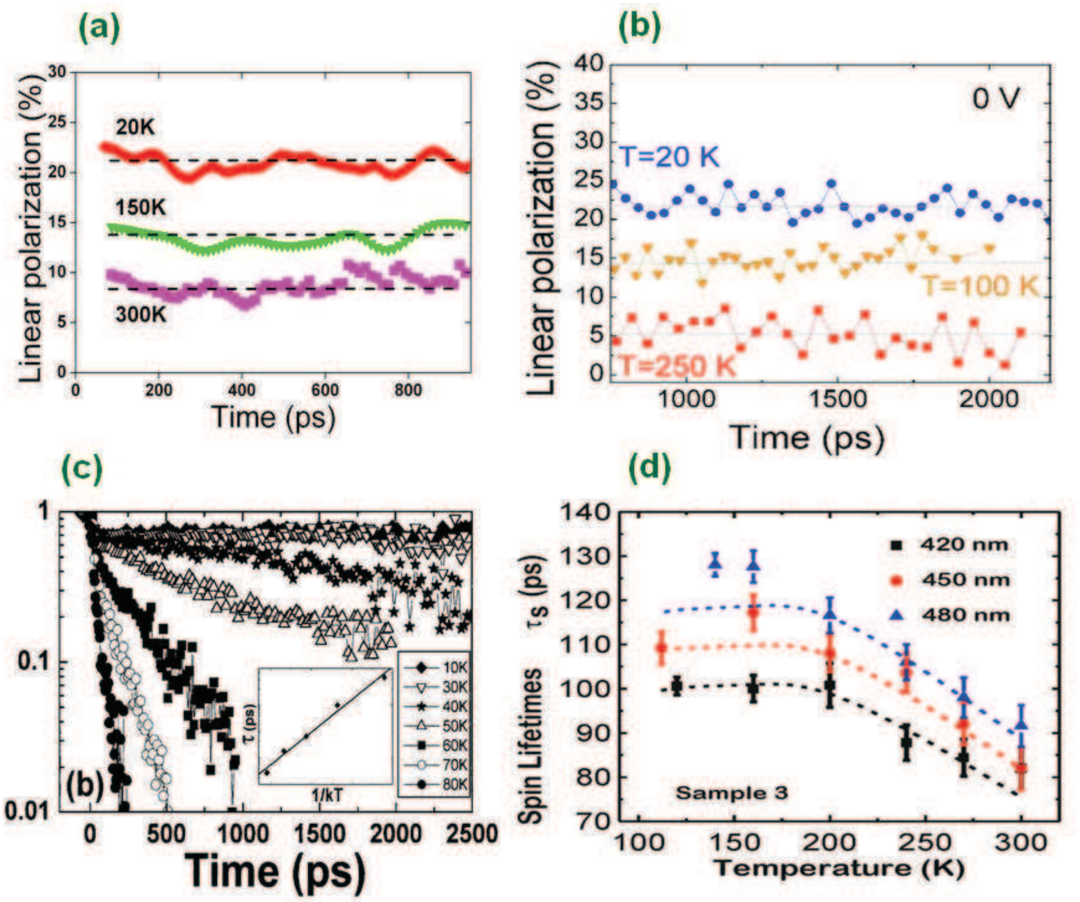

Figure 3.4: *The temperature dependence of the PL linear polarisation dynamics measured after a quasi-resonant linear excitation for (a) Zinc-blende GaN/AlN quantum dots [18]; (b) Wurtzite InGaN/GaN quantum dots embedded in a p-i-n structure [19]; (c) Zinc-blende InAs/GaAS quantum dots [46]. (d) Temperature dependence of the spin lifetimes in InGaN/GaN nanodisks [42].*

Nevertheless, for wide-gap nitride quantum dots, despite the quenching of the exciton polarisation is conserved up to room temperature, a decrease of the amplitude of the linear polarisation with increasing temperature is observed (Fig. 3.4 (a) and (b)). These thermally activated initial depolarisation processes are observed in both wurtzite and zinc-blende structures and do not affect the observed polarisation dynamics. Although the actual mechanism responsible for the decrease of the initial linear polarisation degree is still uncertain, the stability of the exciton polarisation dynamics indicates that the depolarisation processes cannot occur once the exciton lies in the ground states. Depolarisation processes occurring during the exciton formation and relaxation are therefore more likely to be at the origin of the observed temperature dependence.

Finally, Banerjee *et al.* [42] have more recently measured the spin relaxation dyanmics in InGaN quantum disks embedded in GaN quantum wires with different

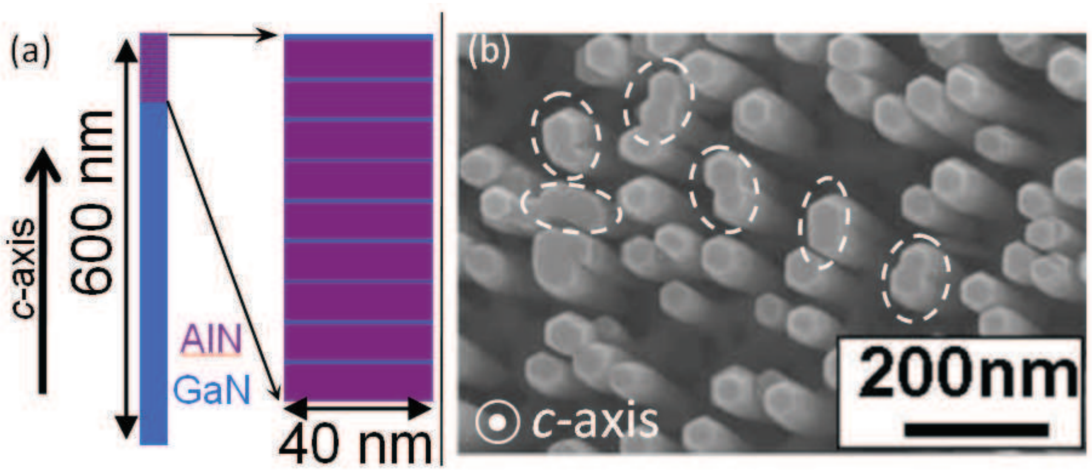

Figure 3.5: *(a) Schematic representation of a single nanowire. (b) Top view SEM image of the nanowires. The white dashed circles highlight some of the coalesced nanowires.*

In contents. The authors reported a circular polarisation degree of the photoluminescence of the order of 0.004. The origin of such a weak polarisation (electronic or excitonic) is however not detailed. These results show a spin relaxation time of the order of 90 ps which is very similar to what observed in quantum wells of the same material [38].

At the beginning of this thesis work no results had been published, to the best of our knowledge, on the exciton spin dynamics of GaN/AlN nanowire embedded quantum dots. The promising results obtained previously in the group on wide-gap nitride nanostructures and the possibility offered by the higher crystallographic quality of nanowires have been the decisive reason to the choice of the subject of this work.

3.3 Spin dynamics of nanowire-embedded GaN quantum dots

3.3.1 Sample and experimental configuration

The sample under study consists of an ensemble of GaN/AlN Quantum Dots embedded in ≈ 40 nm diameter nanowires containing 10 planes of ≈ 1 nm height GaN QDs with a nanowire density of $\approx 10^{10}\text{cm}^{-2}$ (figure 3.5). The whole nanowires are about 600 nm long, in which about 100 nm-height AlN/GaN heterostructures are grown on top of a 500 nm long GaN base. The nanowires are grown on a Si (111) substrate and the details of the growth conditions can be found in references

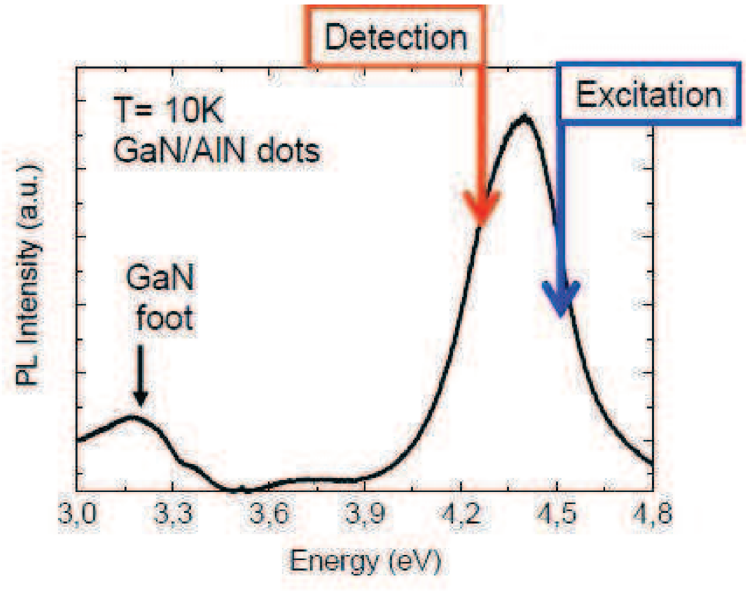

Figure 3.6: *The time integrated photoluminescence spectrum of the sample under non-resonant excitation. The arrows indicate schematically the condition of quasi-resonant excitation used in this work.*

[27–29]. The excitation source is provided by a mode-locked frequency-tripled Ti:Sa laser, with a tunable energy in the range 4.00-4.77 eV. The laser beam, propagating parallel to the nanowires growth axis - c axis - is focused onto the sample to a 50 μm diameter spot with a time averaged power in the range P_{exc}=0.1-1 mW.

Figure 3.6 reports the low temperature photoluminescence spectrum of the sample under non resonant excitation. Two main peaks can be distinguished. The high energy one, centred around 4.35 eV is assigned to the GaN/AlN nanostructures, whereas the signal arising from the GaN foot is centred at 3.15 eV. In order to study the exciton spin dynamics, quasi-resonant excitation of the nanostructures is employed. By quasi-resonant excitation we signify here that both the excitation and detection energies are set within the nanostructures non-resonant photoluminescence emission, as schematically represented in figure 3.6.

In order to clarify the experimental configurations used in this work, we introduce here two reference frames. We first define a fixed orthogonal Cartesian system $(\vec{e}_X, \vec{e}_Y, \vec{e}_Z)$ attached to the laboratory frame such that $\vec{e}_X$ and $\vec{e}_Y$ are perpendicular to the sample growth direction (the c axis), whereas $\vec{e}_Z$ is parallel to it. A second Cartesian orthogonal frame $(\vec{e}(\alpha), \vec{e}_\perp(\alpha), \vec{e}_Z)$ is created by rotating the previous frame by an angle α around the common $\vec{e}_Z$ axis. For α=0, $\vec{e}(\alpha) \equiv \vec{e}_X$ and $\vec{e}_\perp(\alpha) \equiv \vec{e}_Y$ (figure 3.7). The photoluminescence linear polarisation degree in the

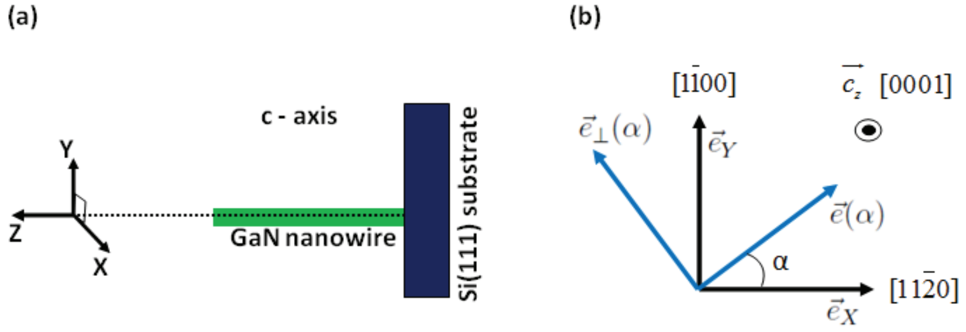

Figure 3.7: *Schematic representation of (a) the sample orientation and (b) the relation between frame* $(\vec{e}(\alpha), \vec{e}_\perp(\alpha))$ *and frame* $(\vec{e}_X, \vec{e}_Y)$. $\vec{e}_X$, $\vec{e}_Y$ *and* $\vec{e}_Z$ *are respectively taken parallel to the* $[11\bar{2}0]$, $[1\bar{1}00]$ *and* $[0001]$ *crystal directions.*

$(\vec{e}(\alpha), \vec{e}_\perp(\alpha), \vec{e}_Z)$ frame is then defined as:

$$P_{lin}(\alpha) = \frac{I^\alpha - I^{\alpha_\perp}}{I^\alpha + I^{\alpha_\perp}}, \tag{3.1}$$

where I^α and $I^{\alpha_\perp}$ denote respectively the linearly polarised PL intensity components along $\vec{e}(\alpha)$ and $\vec{e}_\perp(\alpha)$.

3.3.2 Exciton photoluminescence polarisation of GaN/AlN nanowire QDs: spectral dependence

Figure 3.8 (solid lines) illustrates the time-integrated components of the PL intensity co- (I^X) and cross-polarised (I^Y) with the quasi-resonant linear excitation set along $\vec{e}_X$ (π^X, E_{exc}=4.24 eV) at T=300 K and the corresponding linear polarisation degree (green circles) measured in the laboratory frame. A distinct PL linear polarisation degree is observed for any detection energy in the emission spectrum. The linear polarisation degree is higher ($P_{lin} \approx$ 15 %) when the detection energy is closer to excitation energy and it gradually decreases as the separation between excitation and detection increases. This trend is confirmed by the overall marked decrease of the PL linear polarisation degree after a π^Xexcitation of higher energy (E_{exc}=4.33 eV) as shown by the orange squares. For a linearly polarised laser excitation $E_{exc} \gtrsim$ 450meV above the detection, no PL linear polarisation is measured within the experimental uncertainties.

The PL linear polarisation degree measured along two orthogonal axis (X′,Y′) rotated by $\alpha=\pi/4$ with respect to a quasi resonant linear excitation parallel to the laboratory reference frame (π^X) is reported in figure 3.8 (b) (grey triangles). No linear polarisation degree is observed (${P_{lin}}^{\alpha=\pi/4} \leq 2$ % on the whole PL spectrum),

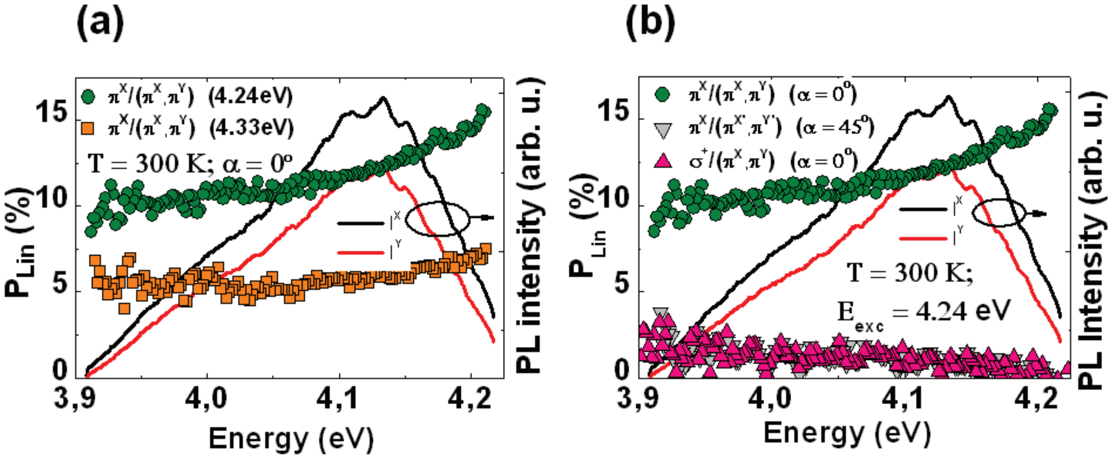

Figure 3.8: *The co- (I^X) and cross-polarised (I^Y) time integrated PL intensities (solid lines) under a π^X quasi-resonant excitation (E_{exc}=4.24 eV) at T=300 K and the corresponding PL linear polarisation degree (green circles) in both (a) and (b). (a) The orange squares reproduce the PL linear polarisation degrees measured for a higher excitation energy, E_{exc}=4.33 eV. (b) The grey downward triangles show the linear polarisation measured with a rotation angle $\alpha = 45^o$ of the detection frame. The pink upward triangles reproduce the linear polarisation measured in the same detection frame ($\alpha = 0^o$) but under circularly polarised excitation in quasi-resonant conditions. The superscripts in $I^{X/Y}$ ($I^{X'/Y'}$) indicate the polarisation directions of the PL intensities used to calculate the PL linear polarisation degree.*

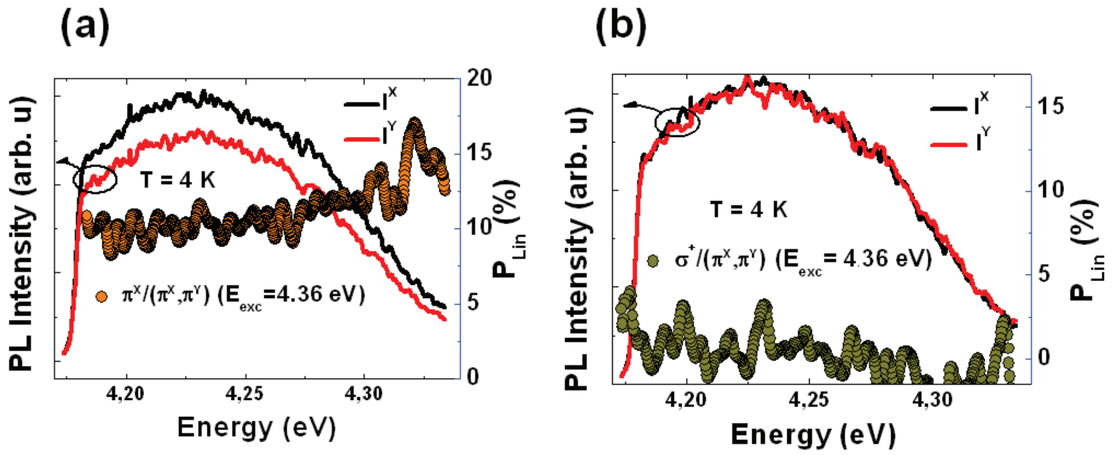

Figure 3.9: *(a) The co- (I^X) and cross-polarised (I^Y) time integrated PL intensities (solid lines) under a linearly polarised (π^X) quasi-resonant excitation (E_{exc}= 4.36 eV - λ_{exc} = 284 nm) at T= 4 K and the corresponding PL linear polarisation degree (orange circles). (b) The co- (I^X) and cross-polarised (I^Y) time integrated PL intensities (solid lines) following a circularly polarised (σ^+) quasi-resonant excitation (E_{exc}= 4.36 eV - λ_{exc} = 284 nm) at T= 4 K and corresponding PL linear polarisation degree (dark yellow circles).*

these observations suggest the existence of linear orthogonal excitonic states. In order to confirm this statement, we have measured the PL linear polarisation degree after a circular polarisation excitation of the same energy. Likewise, no linear polarisation degree is measured (Fig. 3.8(b)).

The same spectral and excitation polarisation dependence of the PL linear polarisation degree is observed at low temperature. As an example, we reproduce in figure 3.9 the PL spectra[1] and the linear polarisation degree of the PL measured at T=4 K under a linear (a) or circular (b) quasi-resonant excitation. From these low and room temperature data we can assert the following:

(i) A spectrally linear polarisation degree can be measured only under a quasi-resonant linear excitation parallel to the detection axis.

(ii) No linear or circular polarisation degree is measured after a circularly polarised excitation. This proves that the linear polarisation degree does not originate from a strain induced valence band mixing or a strong aspect ratio anisotropy, as observed in some InGaN quantum dots [43], or a thermal population distribution of the lowest state. In this case a linear polarisation degree should

---

[1] Note that the spectra are shadowed on the low energy side due to the masking slit at the streak camera entrance.

be measured for any polarisations or energies of the excitation.

(iii) The spectral dependence of the linear polarisation degree is in agreement with previous measurement in zinc-blende or wurtzite wide-gap nitride quantum dots grown by Stranski-Krastanov method [18, 19]. However, an important difference evidences from these measurements: The linear polarisation degree seems not to appreciably change as the temperature is raised. This represents a first marked difference compared to previous results on wide-gap nitride dots in our group, where at room temperature the linear polarisation degree of the photoluminescence reduced to approximately 50% of the low temperature value. We will come back to this point in the section concerning the dynamics of the exciton linear polarisation.

(iv) From the previous statements we can assert that the PL linear polarisation degree is compatible with the optical alignment of orthogonal excitonic states. The optical alignment of the exciton has been already reported for many III-V or II-VI bulk materials or heterostructures [46–50]. In QDs, the origin of the linear symmetry of the exciton eigenstates is generally attributed to the anisotropic electron-hole exchange splitting [51–53] originating from QD elongation and/or interface anisotropy. Here, the symmetry of the dots is generally C_{3v} [54] , so the interface anisotropy argument is not relevant. As detailed in chapter II, the anisotropic electron-hole exchange interaction lifts the degeneracy of the $\mid J_z = \pm 1\big\rangle$ bright excitons which are now separated by the anisotropic exchange interaction Δ_1. Recently Kindel *et al.* [53] reported values of $\Delta_1 \approx$7 meV, much larger than in any other semiconductor quantum dot system reported up to now. This value is typically a few tens of μeV in InAs quantum dots [45].

3.3.3 Exciton photoluminescence polarisation of GaN/AlN nanowire QDs: angular dependence

Previous results for III-N SK quantum dots reported definite directions for the orientation of the split exciton orthogonal eigenstates. These directions were linked to the symmetry of the semiconductor crystal for zinc-blende structures [18] (orientation along the $[110]/[1\bar{1}0]$ directions) and to a symmetry reduction probably due to a residual substrate anisotropy for wurtzite structures [19, 53] (orientation along a subset of $[1\bar{1}00]/[11\bar{2}0]$ directions). In order to identify (a) possible preferential orientation axis for the exciton linear eigenstates and (b) the relative orientation of the linearly polarised exciton states, we have proceed to an angular analysis of the

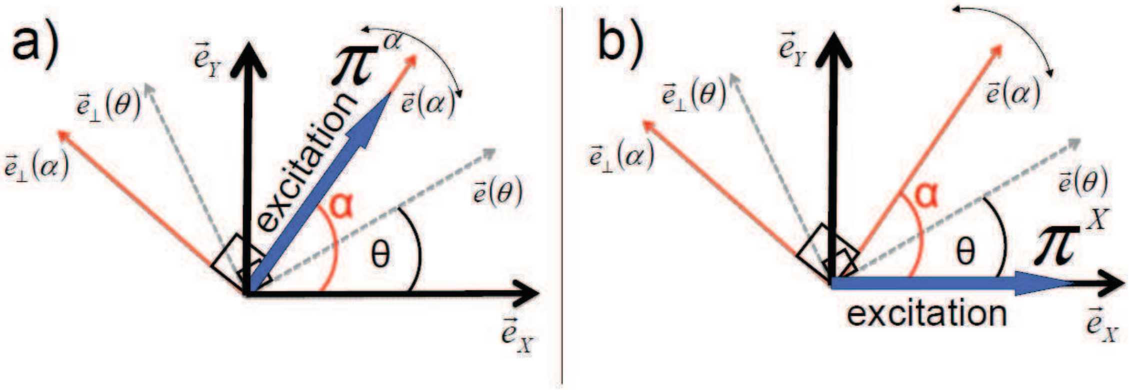

Figure 3.10: *a), b) : Geometry of experiment A and B, respectively. The blue vector presents the linear polarisation of the excitation light. The red orthogonal frame* $(\vec{e}(\alpha), \vec{e}_\perp(\alpha))$ *is the detection frame which is rotated by an angle* α *with respect to the laboratory frame* $(\vec{e}_X, \vec{e}_Y)$*. The orthogonal frame* $(\vec{e}(\theta), \vec{e}_\perp(\theta))$ *corresponds to the orthogonal eigenstates of a given class of exciton dipoles (see explanation in section 3.3.5).*

PL linear polarisation degree. This verification has been accomplished in two steps detailed here below.

3.3.3.1 Experiment A

In the first one, aimed at the determination of a possible preferential orientation axis of the exciton linear states, we measure the PL linear polarisation along two orthogonal axis $(\vec{e}(\alpha), \vec{e}_\perp(\alpha))$ as a function of a simultaneous in plane rotation of the excitation polarisation and detection linear polarisation frame with $\pi^\alpha \parallel \vec{e}(\alpha)$. This experimental configuration is schematically sketched in figure 3.10(a). Photoluminescence co-polarised with the linear exciting laser is always measured. Figure 3.11 shows, as an example, some of the measured PL linear polarisation degree for two temperatures T=7.5 K and T= 300 K. We have obtained quantitatively very similar results for an arbitrary rotation α of the excitation and detection frames around the crystallographic axis c.

This angular behaviour is compatible with the existence of different families of nanowire-embedded QDs characterised by linear orthogonal excitonic eigenstates. The slight difference observed in the linear polarisation degree (ΔP_{lin} ≈3%) measured for different values of the angle α can be attributed to slightly preferred

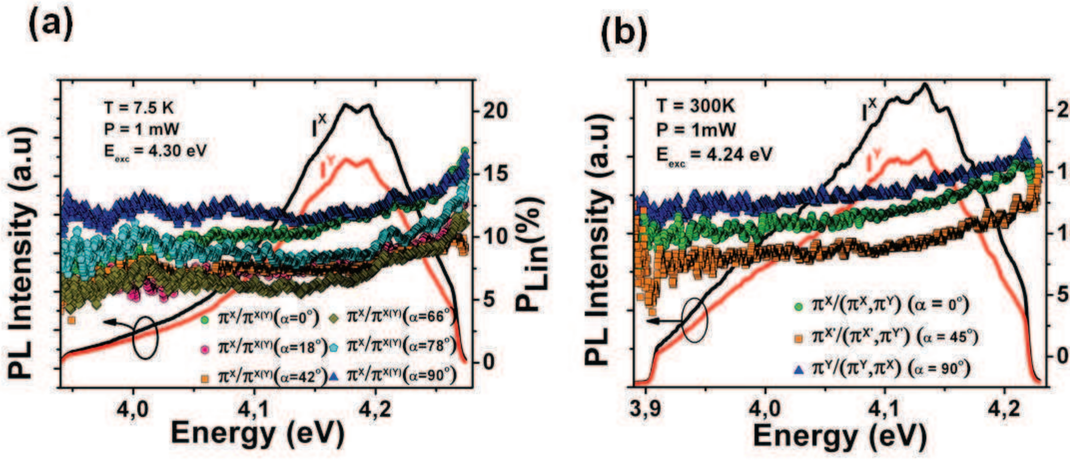

Figure 3.11: *The PL linear polarisation degree measured under quasi-resonant excitation after a simultaneous rotation of both the excitation and detection reference frames with different rotation angles* α *at (a) 7.5 K and (b) 300 K. (a)* $\alpha = 0^o$ *- green circles;* $\alpha = 18^o$ *- pink circles;* $\alpha = 42^o$ *- orange squares;* $\alpha = 66^o$ *- dark yellow rhombi;* $\alpha = 78^o$ *- cyan circles;* $\alpha = 90^o$ *- blue triangles. (b)* $\alpha = 0^o$ *- green circles;* $\alpha = 45^o$ *- orange squares;* $\alpha = 90^o$ *- blue triangles.* $\pi^{X(Y)}$ *indicate respectively a linearly (X or Y, with respect to the laboratory frame) polarised excitation. The superscripts in* $I^{X/Y}$ $(I^{X'/Y'})$ *indicate the polarisation directions of the PL intensities used to calculate the PL linear polarisation degree.*

orientations of the orthogonal linear exciton eigenstates in the sample plane or to a non-perfectly symmetrical oscillator strength for the light absorption in the dots excited states. As it will be clarified by the model developed in the final part of this chapter, if we neglect these minor polarisation differences, the dipole orientation of the linear orthogonal excitonic eigenstates is compatible with either an uniform distribution or a distribution following symmetry C_{3v} or higher (eq. 3.31 and subsequent discussion). This point constitutes a second marked difference with respect to the previously analysed wide gap nitrides dots. The origin of the angular distribution of the exciton eigenstates is still not clear. X-ray analysis performed on similarly grown nanowire-embedded QDs has revealed the same crystallographic orientation for the nanowires corresponding to an in-plane coincidence of the GaN and Si lattices [55]. Therefore, either an in-plane asymmetry due to imperfect hexagonal facets or the roughness fluctuations at the GaN/AlN interfaces [51], or again a coalescence of nanowires in pairs (see figure 3.5b) are likely at the origin of the observed random orientation of the linearly-polarised exciton eigenstates, whereas the arbitrary in-plane crystallographic orientation of the nanowires is ruled out [56].

3.3.3.2 Experiment B

In the second case, aimed at the determination of the relative orientation of the orthogonaly polarised exciton eigenstates, figure 3.10-b, we keep fixed the laser linear excitation along $\vec{e}_X$ and we measure the PL linear polarisation degree in the $(\vec{e}(\alpha), \vec{e}_\perp(\alpha))$ basis. We restrict α to the range $0 \leq \alpha < \pi/2$ since $P_{lin}(\alpha + \pi/2) =$ -$P_{lin}(\alpha)$. Figure 3.12(squares), reports the low temperature experimental data of the time integrated P_{lin} for an energy separation between the excitation and detection ΔE_{e-d}=45 meV (as already evinced in the previous experiments, the polarisation properties in these GaN QDs are very weakly temperature sensitive). Consistently with the prediction of orthogonal exciton linear states, the detected linear polarisation degree in this experiment configuration is anti-symmetrically distributed around 45° where, to a good approximation, it crosses zero. Again, the slight deviation for a perfectly zero polarisation at 45° can be ascribed to a week non-perfectly symmetrical oscillator strength for the quantum dot absorption. The solid line reports the simulated angular dependence of the linear polarisation degree of the exciton luminescence according to the experiment B as detailed in the final section of this chapter.

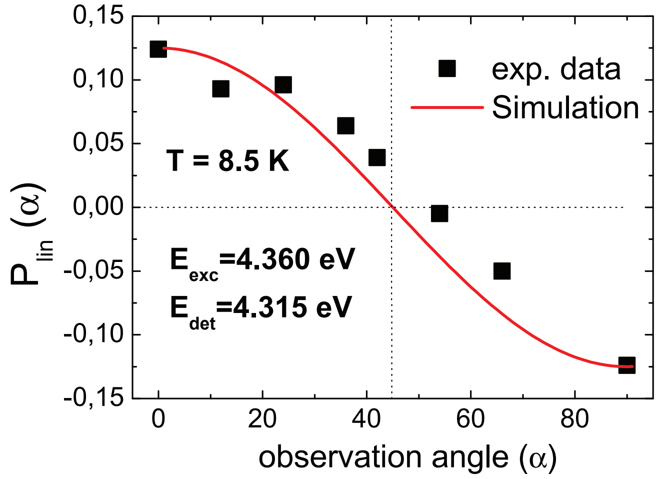

Figure 3.12: *The linear polarisation degree of the photoluminescence measured along the* $(\vec{e}(\alpha), \vec{e}_\perp(\alpha))$ *basis following a linear excitation along the* $\vec{e}_X$ *axis (experiment B, T=8.5 K). The red line is a fit to the data according to equation 3.31 (section 3.3.5).*

3.3.4 Exciton photoluminescence polarisation of GaN/AlN nanowire QDs: dynamics

3.3.4.1 Non depolarisation

Figure 3.13 presents the time evolution at room temperature of the co- and cross-polarised PL intensity components obtained after a quasi resonant linearly polarised excitation (E_{exc}= 4.24 eV, π^X) and the corresponding PL linear polarisation degree measured at two different detection energy regions. Note that at short times, the PL is dominated by the fast decay of scattered laser photons (greyed out in the graph). The short PL decay time ($\tau_{PL} \approx 1$ ns) of the exciton photoluminescence indicates the weak contribution of the Quantum Confined Stark Effect in this structure due to the QD small height. The very similar τ_{PL} observed for the I^X and I^Y components is the signature of the comparable oscillator strength of each orthogonal fundamental exciton state. The QD emission dynamics exhibits a polarisation degree which remains strictly constant in time, within our experimental accuracy, during the exciton lifetime for every wavelength within the PL spectrum.

Under a circularly polarised excitation, quantum beats at the angular frequency corresponding to the anisotropic exchange splitting Δ_1 should be observed in the PL polarisation dynamics. The absence of any measurable polarisation is attributed here to the exchange splitting energy statistical fluctuations among the QD ensemble. As we do not observe any beats for t>200 ps, we can infer that the standard

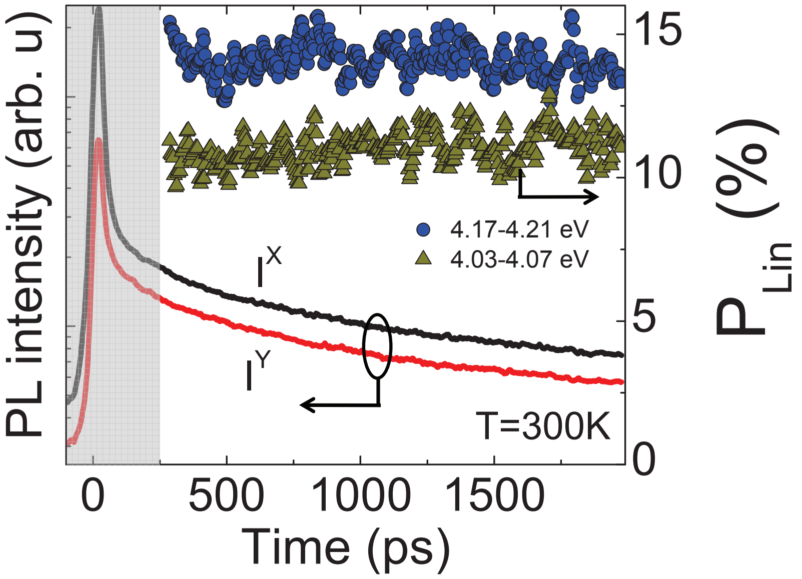

Figure 3.13: *Time evolution of the PL components co- (I^X) and counter-polarised (I^Y) with the linearly polarised quasi resonant excitation (E_{exc}=4.24 eV) and the corresponding linear polarisation degree measured at two different energies. The grey area represents the temporal region dominated by the laser scattered light. The spectra are spectrally integrated according to the caption in the figure.*

deviation of the anisotropic exchange interaction distribution is larger than 10 μeV, which is consistent with recent measurements on SK QDs [53] .

3.3.4.2 Temperature insensitivity

We have finally studied the PL polarisation dynamics as a function of the temperature. As the degree of the PL linear polarisation depends on the excitation-detection energy separation ΔE_{e-d}, to ensure the analysis of the same QD family, we have kept ΔE_{e-d} constant while varying the excitation energy following a simple Varshni law for the band gap temperature dependence:

$$E_g(T) = E_g(0) - \frac{\alpha T^2}{T + \beta}, \tag{3.2}$$

where α and β are the two Varshni parameters for GaN [16]. Figure 3.14 presents the low temperature (T=8.5 K) PL components co- (I^X) and cross-polarised (I^Y) with the linear excitation and the corresponding linear polarisation degree while the inset reproduces the value of the linear polarisation degree for all the measured temperatures up to room temperature. PL linear polarisation features very similar to those observed at 300 K are recorded for any temperature investigated. The very long spin relaxation time measured at low temperature are in agreement with the

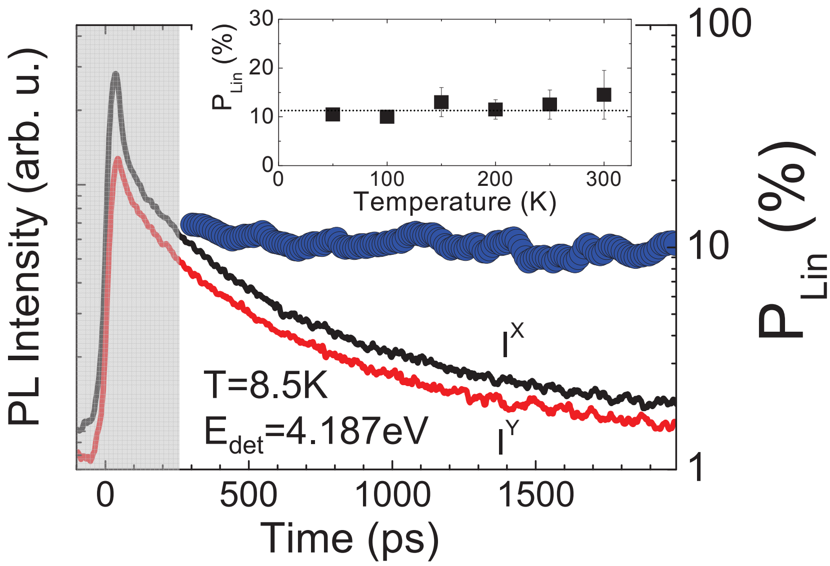

Figure 3.14: *Dynamics of the low temperature (T=8.5 K) PL components co- (I^X) and cross-polarised (I^Y) with the linearly polarised excitation and the corresponding linear polarisation degree. The grey area represents the temporal region dominated by the laser scattered light. Inset: the measured PL linear polarisation degree for all the temperatures investigated. The energy difference between excitation and detection has been kept constant at ΔE =133 meV, and the excitation energy has been varied according to the temperature variation of the QD gap in order to excite the same nanowires family.*

recent calculations of the polarised exciton relaxation rates in GaN QDs [57] with in-plane aspect-ratio close to 1. We can conclude that neither a temporal decay nor a decrease of the P_{lin} degree is observed at any temperature within our experimental uncertainties.

As mentioned in section 3.2.2, room temperature exciton optical alignment was recently evidenced in cubic GaN/AlN [18] and wurtzite InGaN/GaN [19] self assembled QDs, and in QD-like structures induced by In segregation in InGaN/GaN Quantum Wells [58]. In ref. [18, 19] despite a likewise time constant PL linear polarisation degree observed up to room temperature, a clear decrease ($\approx$ 50 %) of the amplitude of the linear polarisation was evidenced from T=10 K to T=300 K. An activation energy for the polarisation degree was determined, for instance, for zinc-blende GaN/AlN SK QDs [18], in the range 50-100 meV. The temperature insensitivity of the exciton alignment is therefore a distinctive property of these nanowire embedded GaN/AlN QDs which strikingly singles out the present findings from the preceding results.

The origin of the temperature robustness of the exciton alignment is still under investigation. Confinement effect comparable to SK GaN/AlN quantum dots are expected for this nanowires structure. This remarkable behavior has therefore to be linked to the peculiar structure of the nanowires. We tentatively ascribe the origin of the observed temperature stability to the higher structural quality of the nanowire embedded QDs compared to the SK structures. Different exciton-phonon interactions compared to SK dots could also play a non-negligible role thanks to the marked different structural configuration of the nanowires [57, 59].

3.3.5 Theoretical model

In this section we detail the model we have developed to account for the measured angular dependence of the PL linear polarisation degree in the nanowire embedded QDs as described by experiment A and B. We remind here the reference frame $\{\vec{e}_X, \vec{e}_Y\}$ (the laboratory frame) perpendicular to the growth axis and set $\vec{e}_X = \vec{e}(\alpha = 0)$ as the origin for measuring the angles.

3.3.5.1 Experiment A

We evaluate here the maximum PL linear polarisation degree measurable in the $\mathfrak{B}_\alpha = \{\vec{e}(\alpha), \vec{e}_\perp(\alpha)\}$ basis, following a quasi resonant excitation along $\vec{e}(\alpha)$ (experiment A - fig 3.10 (a)). We first postulate a random orientation of exciton dipoles corresponding to the orthogonal eigenstates identified by the $(\vec{e}(\theta), \vec{e}_\perp(\theta))$ basis for a given QD, with $0 \leq \theta < \pi$.

We then assume that during the energy relaxation the relative phase between the exciton states is *fully* preserved [2]. Assuming in addition that the oscillator strength of the two orthogonal exciton dipoles are roughly identical, the projection of the wavefunction on the bright excitonic states writes (see fig. 3.10a):

$$\mid \psi_{\theta,\omega_1}(t)\rangle_\theta = \Big(e^{i\omega_1 t/2}\cos(\alpha-\theta)\Big) \mid X_\theta\rangle + \Big(e^{-i\omega_1 t/2}\sin(\alpha-\theta)\Big) \mid Y_\theta\rangle, \tag{3.3}$$

where $|X_\theta\rangle$, $|Y_\theta\rangle$ are the linear bright exciton states and $\hbar\omega_1 = \Delta_1$ is the fine structure splitting of the exciton bright states due to the anisotropic exchange interaction (a global phase factor has been dropped for simplicity). θ represents here the direction of the exciton dipole $\mid X_\theta\rangle$ having the lowest energy. As the polarisation is measured in the $\mathfrak{B}_\alpha$ bases, we express the kets $\mid X_\theta\rangle$ and $\mid Y_\theta\rangle$ in the $\mathfrak{B}_\alpha$ basis by performing a $-(\theta-\alpha)$ rotation of the crystal along the $\vec{e}_z$ using the rotation operator:

$$\hat{\mathbf{R}}_{e_z}(-\theta+\alpha) = e^{i(\theta-\alpha)\frac{\hat{J}_z}{\hbar}},$$

---

[2] This is only partially true. As seen previously, a depolarisation process occurs during the relaxation process. This is discussed later in this chapter.

where $\hat{J}_z$ is the projection of the angular momentum operator on $\vec{e}_Z$. We therefore write :

$$\left\{ \begin{array}{l} |X_\alpha\rangle = e^{i(\theta-\alpha)\frac{\hat{J}_z}{\hbar}}|X_\theta\rangle \\ |Y_\alpha\rangle = e^{i(\theta-\alpha)\frac{\hat{J}_z}{\hbar}}|Y_\theta\rangle. \end{array} \right. \tag{3.4}$$

By using the canonical relations:

$$\left\{ \begin{array}{l} |X_\theta\rangle = \dfrac{1}{\sqrt{2}}\left(|1,-1\rangle_\theta - |1,+1\rangle_\theta\right) \\ |Y_\theta\rangle = -\dfrac{1}{i\sqrt{2}}\left(|1,-1\rangle_\theta + |1,+1\rangle_\theta\right) \end{array} \right. \Leftrightarrow \left\{ \begin{array}{l} |1,+1\rangle_\theta = -\dfrac{1}{\sqrt{2}}\left(|X_\theta\rangle + i|Y_\theta\rangle\right) \\ |1,-1\rangle_\theta = \dfrac{1}{\sqrt{2}}\left(|X_\theta\rangle - i|Y_\theta\rangle\right) \end{array} \right. , \tag{3.5}$$

we have:

$$\left\{ \begin{array}{l} |X_\alpha\rangle = \cos(\theta-\alpha)|X_\theta\rangle - \sin(\theta-\alpha)|Y_\theta\rangle \\ |Y_\alpha\rangle = \sin(\theta-\alpha)|X_\theta\rangle + \cos(\theta-\alpha)|Y_\theta\rangle, \end{array} \right.$$

and the inverse relations:

$$\left\{ \begin{array}{l} |X_\theta\rangle = \cos(\theta-\alpha)|X_\alpha\rangle + \sin(\theta-\alpha)|Y_\alpha\rangle \\ |Y_\theta\rangle = -\sin(\theta-\alpha)|X_\alpha\rangle + \cos(\theta-\alpha)|Y_\alpha\rangle. \end{array} \right. \tag{3.6}$$

From equations (3.3) and (3.6), we can rewrite the expression $|\ \psi_{\theta,\omega_1}(t)\rangle_\alpha$ in the $\mathfrak{B}_\alpha$ basis as:

$$\begin{aligned} |\ \psi_{\theta,\omega_1}(t)\rangle_\alpha = & \Big[e^{i\omega_1 t/2}\cos^2(\theta-\alpha) + e^{-i\omega_1 t/2}\sin^2(\theta-\alpha)\Big]\ |\ X_\alpha\rangle \\ & + \Big[e^{i\omega_1 t/2}\sin(\theta-\alpha)\cos(\theta-\alpha) - e^{-i\omega_1 t/2}\sin(\theta-\alpha)\cos(\theta-\alpha)\Big]\ |\ Y_\alpha\rangle. \end{aligned} \tag{3.7}$$

The restriction of the exciton density operator to the bright exciton states writes:

$$\tilde{\rho}^{\alpha}_{\theta,\omega_1}(t) = \Big|\tilde{\Psi}_{\theta,\omega_1}(t)\Big\rangle_{\alpha\alpha}\Big\langle\tilde{\Psi}_{\theta,\omega_1}(t)\Big|, \tag{3.8}$$

or introducing the matrix representation:

$$\begin{aligned} \tilde{\rho}^{\alpha}_{\theta,\omega_1}(t) = & \Big(\tilde{\rho}_{\theta,\omega_1}\Big)_{X_\alpha X_\alpha}\Big|X_\alpha\Big\rangle\Big\langle X_\alpha\Big| + \Big(\tilde{\rho}_{\theta,\omega_1}\Big)_{X_\alpha Y_\alpha}\Big|X_\alpha\Big\rangle\Big\langle Y_\alpha\Big| \\ & + \Big(\tilde{\rho}_{\theta,\omega_1}\Big)_{Y_\alpha X_\alpha}\Big|Y_\alpha\Big\rangle\Big\langle X_\alpha\Big| + \Big(\tilde{\rho}_{\theta,\omega_1}\Big)_{Y_\alpha Y_\alpha}\Big|Y_\alpha\Big\rangle\Big\langle Y_\alpha\Big|, \end{aligned}$$

where

$$\left\{ \begin{array}{l} \Big(\tilde{\rho}_{\theta,\omega_1}\Big)_{X_\alpha X_\alpha} = 1 - \dfrac{1}{4}\Big[1-\cos 4(\theta-\alpha)\Big]\Big[1-\cos(\omega_1 t)\Big] \\ \\ \Big(\tilde{\rho}_{\theta,\omega_1}\Big)_{Y_\alpha Y_\alpha} = \dfrac{1}{4}\Big[1-\cos 4(\theta-\alpha)\Big]\Big[1-\cos(\omega_1 t)\Big) \\ \\ \Big(\tilde{\rho}_{\theta,\omega_1}\Big)_{X_\alpha Y_\alpha} = \dfrac{1}{4}\sin 4(\theta-\alpha)\Big[1-\cos(\omega_1 t) - \dfrac{i}{2}\sin 2(\theta-\alpha)\sin(\omega_1 t) \\ \\ \Big(\tilde{\rho}_{\theta,\omega_1}\Big)_{Y_\alpha X_\alpha} = \Big(\tilde{\rho}_{\theta,\omega_1}\Big)^{*}_{X_\alpha Y_\alpha}. \end{array} \right. \tag{3.9}$$

Moreover,

$$\left(\tilde{\rho}_{\theta,\omega_1}\right)_{X_\alpha X_\alpha}\left(\tilde{\rho}_{\theta,\omega_1}\right)_{Y_\alpha Y_\alpha} = \mid \left(\tilde{\rho}_{\theta,\omega_1}\right)_{X_\alpha Y_\alpha} \mid^2 \tag{3.10}$$

according to the fact that $\left|\tilde{\Psi}_{\theta,\omega_1}(t)\right\rangle$ is a pure state. The density matrix of the quantum dot ensemble is then given, for $t > t_{relax}$, by:

$$\tilde{\rho}(t) = \int_0^\pi d\theta \int d\omega_1 \; g(\theta,\omega_1) \; \tilde{\rho}^\alpha_{\theta,\omega_1}(t). \tag{3.11}$$

We assume that there is no correlation between the fine structure splitting amplitude and the orientation θ of the excitonic dipoles, so that the probability distribution of the exciton dipoles θ and fine structure splitting energy $\hbar\omega_1$ can be written as $g(\theta,\omega_1) = g_0(\theta)g_1(\omega_1)$. We then model the angular distribution function $g_0(\theta)$ by a uniform law and the fine structure splitting distribution $g_1(\omega_1)$ by a Gaussian centered on $\bar{\omega}$ with standard deviation σ_ω, so that:

$$\begin{aligned} g_0(\theta) &= 1/\pi & (3.12) \\ g_1(\omega_1) &= \frac{1}{\sqrt{2\pi}\sigma_\omega} e^{-\frac{(\omega_1-\bar{\omega})^2}{2\sigma_\omega^2}}. & (3.13) \end{aligned}$$

By using the identity:

$$\int_{-\infty}^{+\infty} \frac{1}{\sqrt{2\pi}\sigma_\omega} e^{-\frac{(\omega-\bar{\omega})^2}{2\sigma_\omega^2}} e^{\mp i\omega t} \mathrm{d}\omega = e^{\pm i\bar{\omega}t} e^{-\frac{\sigma_\omega^2 t^2}{2}} \tag{3.14}$$

the density matrix for the exciton dipole ensemble oriented along θ writes:

$$\tilde{\rho}(t) = \int_{-\infty}^{+\infty} \mathrm{d}\omega g_1(\omega) \left|\tilde{\Psi}_{\theta,\omega}(t)\right\rangle_{\alpha\;\alpha}\left\langle\tilde{\Psi}_{\theta,\omega}(t)\right|$$

$$\begin{cases} \left(\tilde{\rho}_\theta(t)\right)_{X_\alpha X_\alpha} = 1 - \frac{1}{4}\left[1-\cos 4(\theta-\alpha)\right]\left[1 - e^{-\frac{\sigma_\omega^2 t^2}{2}}\cos\left(\bar{\omega}t\right)\right] \\ \\ \left(\tilde{\rho}_\theta(t)\right)_{Y_\alpha Y_\alpha} = \frac{1}{4}\left[1-\cos 4(\theta-\alpha)\right]\left[1 - e^{-\frac{\sigma_\omega^2 t^2}{2}}\cos\left(\bar{\omega}t\right)\right] \\ \\ \left(\tilde{\rho}_\theta(t)\right)_{X_\alpha Y_\alpha} = \frac{1}{4}\left[1-\sin 4(\theta-\alpha)\right]\left[1 - e^{-\frac{\sigma_\omega^2 t^2}{2}}\cos\left(\bar{\omega}t\right)\right] - \frac{i}{2}\sin 2(\theta-\alpha)e^{-\frac{\sigma_\omega^2 t^2}{2}}\sin\left(\bar{\omega}t\right) \\ \\ \left(\tilde{\rho}_\theta(t)\right)_{Y_\alpha X_\alpha} = \left(\tilde{\rho}_\theta(t)\right)^*_{X_\alpha Y_\alpha}. \end{cases}$$

Finally, the system density matrix is given by:

$$\tilde{\rho}(t) = \int_0^\pi d\theta g_0(\theta)\tilde{\rho}^\alpha_\theta(t) \tag{3.15}$$

$$\begin{cases} \left(\tilde{\rho}(t)\right)_{X_\alpha X_\alpha} = 1 - \frac{1}{4}\left[1 - e^{-\frac{\sigma_\omega^2 t^2}{2}}\cos(\bar{\omega}t)\right] \\ \\ \left(\tilde{\rho}(t)\right)_{Y_\alpha Y_\alpha} = \frac{1}{4}\left[1 - e^{-\frac{\sigma_\omega^2 t^2}{2}}\cos(\bar{\omega}t)\right] \\ \\ \left(\tilde{\rho}(t)\right)_{X_\alpha Y_\alpha} = \left(\tilde{\rho}(t)\right)_{Y_\alpha X_\alpha} = 0. \end{cases} \tag{3.16}$$

The final density matrix is therefore independent from the orientation α of the detection basis, and displays only the population terms.

Assuming that the radiative rate does not depend on θ and ω, the linear polarisation degree measured in the $\mathfrak{B}_\alpha$ basis is finally given by:

$$\begin{aligned} P_{lin}(\alpha) &= \frac{\Big(\tilde{\rho}(t)\Big)_{X_\alpha X_\alpha} - \Big(\tilde{\rho}(t)\Big)_{Y_\alpha Y_\alpha}}{\Big(\tilde{\rho}(t)\Big)_{X_\alpha X_\alpha} + \Big(\tilde{\rho}(t)\Big)_{Y_\alpha Y_\alpha}} \\ &= \frac{1}{2}\Big(1 + e^{-\frac{\sigma_\omega^2 t^2}{2}} \cos(\bar{\omega} t)\Big) \\ \text{and} \qquad P'_{lin}(\alpha) &= P_{circ}(\alpha) = 0, \qquad\qquad \forall \alpha \in [0, \pi] \end{aligned} \tag{3.17}$$

where we can see that the linear polarisation does not depend on the excitation angle α ($P'_{lin}(\alpha)$ is the linear polarisation measured in the $\mathfrak{B}_\alpha(\alpha = 45^o)$ basis). If $\sigma_\omega \lesssim \bar{\omega}$, we should observe damped oscillations of linear polarisation for $t \lesssim \sigma_\omega^{-1}$. In the opposite case $\bar{\omega} \lesssim \sigma_\omega$, $P_{lin}(t, \alpha)$ varies from 1 to 0.5 without oscillations. Following the assumption of no preferential orientation of the quantum dots no circular polarisation can be measured under circularly polarised excitation.
In our experiment, the investigated time range is $t >$200 ps and the condition t$\gg \sigma_\omega^{-1}$ consequently holds. The density matrix at $t_0 \approx 200$ ps writes:

$$\tilde{\rho}(t_0) = \begin{pmatrix} 3/4 & 0 \\ 0 & 1/4 \end{pmatrix}. \tag{3.18}$$

As we do not observe any linear polarisation relaxation during the exciton lifetime, the subsequent time evolution is given by

$$\tilde{\rho}(t) = \tilde{\rho}(t_0) e^{-t/\tau_{rad}}, \tag{3.19}$$

where we have added the exponential factor to take into account the exciton radiative recombination. The PL linear polarisation in the $\mathfrak{B}_\alpha$ basis is therefore $P_{lin}(t) = 1/2$ which is constant and independent of the laser linear polarisation direction.

Experimentally, we obtain $P_{lin}^{X/Y} \leq 0.15$ on the whole detection spectrum signifying that depolarisation mechanisms occur during the energy relaxation. In a more realistic approach we should consider that during the energy relaxation the relative phase between exciton states is only *partially* preserved. We characterize the coherence loss during the energy relaxation process by a phenomenological energy dependent coefficient $C\,(\Delta E_{e-d})$ so that $\tilde{\rho}(t_0)$ is replaced by:

$$\tilde{\rho}^{eff}(t_0) = \tilde{\rho}(t_0)\,(1 - C) + (C/2)\,\hat{\mathbb{I}} \qquad 0 \leq C \leq 1 \tag{3.20}$$

where $\hat{\mathbb{I}}$ is the identity matrix. The PL linear polarisation is then:

$$P_{lin}(\alpha, C) = \frac{1 - C}{2}. \tag{3.21}$$

Experimentally we observe in fig. 3.12 $P_{lin}\,(\alpha = 0)$=12.5% for a PL detection 45 meV below the excitation, implying C (45 meV)=0.75. Note that a similar depolarisation value was measured in InAs/GaAs quantum dots by comparing the PL polarisation degree obtained under strictly resonant excitation and quasi-resonant excitation conditions (one LO phonon above the ground exciton state [60]).

3.3.5.2 Experiment B

We now turn to the modeling of experiment B, where the excitation linear polarisation is kept fixed along the $\vec{e}_X$ direction while we rotate the observation basis $(\vec{e}(\alpha), \vec{e}_\perp(\alpha))$ by an arbitrary angle α (fig 3.10 (b)). The projection of the excitonic state on the bright state basis, just after the energy relaxation, is now given in the basis $\{\mid X_\alpha\rangle, \mid Y_\alpha\rangle\}$ by:

$$\begin{aligned} \mid \psi_{\theta,\omega_1}(t)\rangle_\alpha = &\Big[e^{i\omega_1 t/2}\cos(\theta)\cos(\theta-\alpha) + e^{-i\omega_1 t/2}\sin(\theta)\sin(\theta-\alpha)\Big] \mid X_\alpha\rangle + \\ &\Big[e^{i\omega_1 t/2}\cos(\theta)\sin(\theta-\alpha) - e^{-i\omega_1 t/2}\sin(\theta)\cos(\theta-\alpha)\Big] \mid Y_\alpha\rangle. \end{aligned} \tag{3.22}$$

The restriction of the density matrix to the bright exciton states for one quantum dot in the $\mathfrak{B}_\alpha$ basis is:

$$\begin{cases} \Big(\tilde{\rho}_{\theta,\omega_1}(t)\Big)_{X_\alpha X_\alpha} = \cos^2\alpha - \dfrac{1}{2}\sin 2\theta \sin 2(\theta-\alpha)\Big[1-\cos(\omega_1 t)\Big] \\ \Big(\tilde{\rho}_{\theta,\omega_1}(t)\Big)_{Y_\alpha Y_\alpha} = \sin^2\alpha + \dfrac{1}{2}\sin 2\theta \sin 2(\theta-\alpha)\Big[1-\cos(\omega_1 t)\Big] \\ \Big(\tilde{\rho}_{\theta,\omega_1}(t)\Big)_{X_\alpha Y_\alpha} = \dfrac{1}{2}\cos 2\theta \sin 2(\theta-\alpha) - \dfrac{1}{2}\sin 2\theta\Big[\cos(\omega_1 t)\cos 2(\theta-\alpha) + i\sin(\omega_1 t)\Big] \\ \Big(\tilde{\rho}_{\theta,\omega_1}(t)\Big)_{Y_\alpha X_\alpha} = \Big(\tilde{\rho}_{\theta,\omega_1}(t)\Big)^*_{XY}. \end{cases}$$

Assuming the same hypothesis on the distribution of the anisotropic exchange interaction and exciton eigenstate orientations we obtain:

$$\begin{cases} \Big(\tilde{\rho}(t)\Big)_{X_\alpha X_\alpha} = \dfrac{1}{2}[1+\cos 2\alpha] - \dfrac{1}{4}\cos 2\alpha\left[1 - e^{-\frac{\sigma_\omega^2 t^2}{2}}\cos(\bar{\omega}t)\right] \\ \Big(\tilde{\rho}(t)\Big)_{Y_\alpha Y_\alpha} = \dfrac{1}{2}[1-\cos 2\alpha] + \dfrac{1}{4}\cos 2\alpha\left[1 - e^{-\frac{\sigma_\omega^2 t^2}{2}}\cos(\bar{\omega}t)\right] \\ \Big(\tilde{\rho}(t)\Big)_{X_\alpha Y_\alpha} = -\dfrac{1}{4}\sin 2\alpha\left[1 + e^{-\frac{\sigma_\omega^2 t^2}{2}}\cos(\bar{\omega}t)\right] \\ \Big(\tilde{\rho}(t)\Big)_{Y_\alpha X_\alpha} = \Big(\tilde{\rho}(t)\Big)^*_{XY} = \Big(\tilde{\rho}(t)\Big)_{XY}. \end{cases} \tag{3.23}$$

The linear polarisation of the excitons is:

$$P_{lin}(\alpha) = \frac{1}{2}\cos(2\alpha)\left[1 + e^{-\frac{\sigma_\omega^2 t^2}{2}}\cos(\bar{\omega}t)\right] \tag{3.24}$$

and the linear diagonal polarisation describe in the base $\{\vec{e}(\alpha), \vec{e}_\perp(\alpha)\}$ is:

$$\begin{aligned} P'_{lin}(\alpha) &= 2\mathrm{Re}(\rho_{YX}(\alpha)) \\ &= -\frac{1}{2}\sin 2\alpha\left[1 + e^{-\frac{\sigma_\omega^2 t^2}{2}}\cos(\bar{\omega}t)\right] \\ &= P_{lin}\left(\alpha + \frac{\pi}{4}\right), \end{aligned} \tag{3.25}$$

while its circular polarisation:

$$P_{circ}(\alpha) = 2\mathrm{Im}(\rho_{YX}(\alpha)) = 0. \tag{3.26}$$

Similarly to the previous experiment modeling, for $t \gtrsim \sigma_\omega^{-1}$, we have:

$$P_{lin}(\alpha) = \frac{1}{2}\cos(2\alpha) \tag{3.27}$$

$$P'_{lin}(\alpha) = -\frac{1}{2}\sin(2\alpha) = P_{lin}\left(\alpha + \frac{\pi}{4}\right) \tag{3.28}$$

$$P_{circ}(\alpha) = 0. \tag{3.29}$$

Under the same assumption as previously detailed, for $t > 200$ ps ($t \gtrsim \sigma_\omega^{-1}$) we obtain:

$$\begin{aligned} \tilde{\rho}^{eff,\alpha}(t_0) &= \frac{1-C}{2}\begin{pmatrix} 1 + \frac{\cos(2\alpha)}{2} & -\frac{\sin(2\alpha)}{2} \\ -\frac{\sin(2\alpha)}{2} & 1 - \frac{\cos(2\alpha)}{2} \end{pmatrix} + \frac{C}{2}\hat{\mathbb{I}} \\ &= \frac{1}{2}\begin{pmatrix} 1 + \frac{1-C}{2}\cos(2\alpha) & -\frac{1-C}{2}\sin(2\alpha) \\ -\frac{1-C}{2}\sin(2\alpha) & 1 - \frac{1-C}{2}\cos(2\alpha) \end{pmatrix}. \end{aligned} \tag{3.30}$$

The PL linear polarisation is now given by:

$$P_{lin}(\alpha, C) = \frac{\cos(2\alpha)}{2}(1 - C). \tag{3.31}$$

Figure 3.12 presents the experimental data and the calculated curve according to equation (3.31) for $T = 8.5$ K and $\Delta_{e-d} = 45\ meV$, using the same depolarisation coefficient C=0.75 as in experiment A. The agreement between the experimental data and the calculation is satisfactory taking into account that neither an oscillator strength difference between the exciton eigenstates nor any anisotropy of the exciton states distribution in the sample plane have been considered. However, other distributions $g_0(\theta)$ of the exciton dipole orientation possessing C_{3v} or higher symmetry do not modify the results of the measured linear polarisation degree as described by equation 3.31. This prevent us from drawing definite conclusions on the actual distribution of the exciton dipole orientation in these ensemble measurements.

3.4 Conclusion

In conclusion, we have studied the optical orientation of the exciton spin in nanowire-embedded GaN/AlN Quantum Dots. We have observed the quenching of the exciton spin relaxation time and the temperature insensitivity of the exciton PL linear polarisation degree. These results contrast with the temperature decrease of the linear polarisation degree observed in other nitride-based QD systems [18, 19]. A careful investigation of the angular dependence of the PL linear polarisation has been conducted which reveals the presence of independent families of QDs with orthogonal exciton eigenstates with an orientation of their dipole compatible with either an uniform distribution or a distribution following symmetry C_{3v} or higher.

Bibliography

[1] S. Nakamura, T. Mukai, and M. Senoh, *Candela-class high-brightness InGaN/AlGaN double-heterostructure blue-light-emitting diodes*, Applied Physics Letters **64**, 1687 (1994).

[2] S. Nakamura, M. Senoh, S.-i. Nagahama, and N. Iwasa, *Room-temperature continuous-wave operation of InGaN multi-quantum-well structure laser diodes*, Applied Physics Letters **69**, 4056 (1996).

[3] S. Guha, N.A Bojarczuk, *Ultraviolet and violet GaN light emitting diodes on silicon*, Applied Physics Letters **72**, 415 (1998).

[4] J.W. Yang, A. Lunev, G. Simin, A. Chitnis, M. Shatalov, M.A. Khan, J.E. Van Nostrand, R. Gaska, *Selective area deposited blue GaN–InGaN multiple-quantum well light emitting diodes over silicon substrates*, Applied Physics Letters **76**, 273 (2000).

[5] E. Feltin, A. Castiglia, G. Cosendey, L. Sulmoni, J. Carlin, N. Grandjean, M. Rossetti, J. Dorsaz, V. Laino, M. Duelk, *Broadband blue superluminescent light-emitting diodes based on GaN*, et al., Applied Physics Letters **95**, 081107 (2009).

[6] G. Christmann, R. Butté, E. Feltin, J. Carlin, and N. Grandjean, *Room temperature polariton lasing in a GaN/AlGaN multiple quantum well microcavity*, Applied Physics Letters **93**, 051102 (2008).

[7] J. Wu, W. Walukiewicz, K. M. Yu, W. Shan, J. W. A. Iii, H. Lu, and W. J. Schaff, *Superior radiation resistance of $In_{1-x}Ga_xN$ alloys: Full-solar-spectrum photovoltaic material system*, Journal of Applied Physics **94**, 6477 (2003).

[8] B. Beschoten, E. Johnston-Halperin, D. K. Young, M. Poggio, J. E. Grimaldi, S. Keller, S. P. DenBaars, U. K. Mishra, E. L. Hu, and D. D. Awschalom, *Spin coherence and dephasing in GaN*, Physical Review B **63**, 121202 (2001).

[9] A. Tackeuchi, H. Otake, Y. Ogawa, T. Ushiyama, T. Fujita, F. Takano, and H. Akinaga, *Nanosecond excitonic spin relaxation in cubic GaN*, Applied Physics Letters **88**, 162114 (2006).

[10] J. H. Buß, J. Rudolph, T. Schupp, D. J. As, K. Lischka, and D. Hägele, *Long room-temperature electron spin lifetimes in highly doped cubic GaN*, Applied Physics Letters **97**, 062101 (2010a).

[11] J. H. Buß, J. Rudolph, F. Natali, F. Semond, and D. Hägele, *Temperature dependence of electron spin relaxation in bulk GaN*, Physical Review B **81**, 155216 (2010b).

[12] J. H. Buß, J. Rudolph, S. Shvarkov, H. Hardtdegen, A. D. Wieck, and D. Hagele, *Long electron spin coherence in ion-implanted GaN: The role of localization*, Applied Physics Letters **102**, 192102 (2013).

[13] J. H. Buß, J. Rudolph, F. Natali, F. Semond, and D. Hagele, *Anisotropic electron spin relaxation in bulk GaN*, Applied Physics Letters **95**, 192107 (2009).

[14] S. Nagahara, M. Arita, and Y. Arakawa, *No temperature dependence of spin relaxation in InGaN phase-separated quantum dots*, Applied Physics Letters **88**, 083101 (2006a).

[15] M. Dyakonov, *Spin Physics in Semiconductors*, (Springer, New York, 2008), 1st ed.

[16] I. Vurgaftman and J. R. Meyer, *Band parameters for nitrogen-containing semiconductors*, Journal of Applied Physics **94**, 3675 (2003).

[17] J. Y. Fu and M. W. Wu, *Spin-orbit coupling in bulk ZnO and GaN*, Journal of Applied Physics **104**, 093712 (2008).

[18] D. Lagarde, A. Balocchi, H. Carrère, P. Renucci, T. Amand, X. Marie, S. Founta, and H. Mariette, *Room-temperature optical orientation of the exciton spin in cubic GaN/AlN quantum dots*, Physical Review B **77**, 041304 (2008).

[19] M. Sénès, D. Lagarde, K. L. Smith, A. Balocchi, S. E. Hooper, T. Amand, J. Heffernan, and X. Marie, *Electrical control of the exciton spin in nitride semiconductor quantum dots*, Applied Physics Letters **94**, 223114 (2009).

[20] T. Kuroda, T. Yabushita, T. Kosuge, and A. Tackeuchi, K. Taniguchi, T. Chinone, and N. Horio, *Subpicosecond exciton spin relaxation in GaN*, Applied Physics Letters **85**, 3116 (2004).

[21] T. Ishiguro, Y. Toda, and S. Adachi, *Exciton spin relaxation in GaN observed by spin grating experiment*, Applied Physics Letters **90**, 011904 (2007).

[22] C. Brimont, M. Gallart, O. Crégut, B. Hönerlage, and P. Gilliot, *Experimental investigation of excitonic spin relaxation dynamics in GaN*, Physical Review B **77**, 125201 (2008).

[23] C. Brimont, M. Gallart, O. Cregut, B. Honerlage, P. Gilliot, D. Lagarde, A. Balocchi, T. Amand, X. Marie, S. Founta, and H. Mariette, *Optical and spin coherence of excitons in zinc-blende GaN*, Journal of Applied Physics **106**, 053514 (2009).

[24] Christelle Brimont, Mathieu Gallart, Atef Gadalla, Olivier Cregut, Bernd Honerlage, and Pierre Gilliot, *Dislocation density and band structure effects on spin dynamics in GaN*, Journal of Applied Physics **105**, 023502 (2009).

[25] Debdeep Jena, *Spin scattering by dislocations in III-V semiconductors*, Physical Review B **70**, 245203 (2004).

[26] S. V. Gupalov, E. L. Ivchenko, and A. V. Kavokin, *Fine structure of localized exciton levels in quantum wells*, Journal of Experimental and Theoretical Physics **86**, 388 (1998).

[27] R. Songmuang, O. Landré, and B. Daudin, *From nucleation to growth of catalyst-free GaN nanowires on thin AlN buffer layer*, Applied Physics Letters **91**, 251902 (2007).

[28] J. Renard, R. Songmuang, G. Tourbot, C. Bougerol, B. Daudin, and B. Gayral, *Evidence for quantum-confined Stark effect in GaN/AlN quantum dots in nanowires*, Physical Review B **80**, 121305 (2009).

[29] J. Renard, R. Songmuang, C. Bougerol, B. Daudin, and B. Gayral, *Exciton and biexciton luminescence from single GaN/AlN quantum dots in nanowires*, Nano Letters **8**, 2092 (2008).

[30] M.A. Sanchez-Garcia, E. Calleja, E. Monroy, F.J. Sanchez, F. Calle, E. Muñoz, R. Beresford, *The effect of the III/V ratio and substrate temperature on the morphology and properties of GaN- and AIN-layers grown by molecular beam epitaxy on Si(111)*, Journal of Crystal Growth **183**, 23-30 (1998).

[31] E. Calleja, M.A Sanchez-Garcia, F.J. Sanchez, F. Calle, F.B. Naranjo, E. Muñoz, *Luminescence properties and defects in GaN nanocolumns grown by molecular beam epitaxy*, Physical Review B **62**, 16826 (2000).

[32] Akihiko Kikuchi, Mizue Kawai, Makoto Tada and Katsumi Kishino, *InGaN/GaN Multiple quantum disk nanocolumn light-emitting diodes grown on (111) Si substrate*, Japanese Journal of Applied Physics **43**, L1524 (2004).

[33] Masaki Yoshizawa, Akihiko Kikuchi, Masashi Mori, Nobuhiko Fujita and Katsumi Kishino, *Growth of self-organized GaN nanostructures on* Al_2O_3 *(0001) by RF-radical source molecular beam epitaxy*, Japanese Journal of Applied Physics **36**, L459 (1997).

[34] X. J. Chen, B. Gayral, D. Sam-Giao, C. Bougerol, C. Durand, and J. Eymery, *Catalyst-free growth of high-optical quality GaN nanowires by metal-organic vapour phase epitaxy*, Applied Physics Letters **99**, 251910 (2011).

[35] Z. G. Yu , S. Krishnamurthy, Mark van Schilfgaarde and N. Newman, *Spin relaxation of electrons and holes in zinc-blende semiconductors*, Physical Review B **71**, 245312 (2005).

[36] Srinivasan Krishnamurthy, Mark van Schilfgaarde and Nathan Newman, *Spin lifetimes of electrons injected into GaAs and GaN*, Applied Physics Letters **83**, 1761 (2003).

[37] Seiji Nagahara, Munetaka Arita, and Yasuhiko Arakawa. *Long-lived electron spins in* $In_xGa_{1-x}N$ *multiquantum well*, Applied Physics Letters **86**, 242103 (2005).

[38] Seiji Nagahara, Munetaka Arita, and Yasuhiko Arakawa, *No temperature dependence of spin relaxation in InGaN phase-separated quantum dots*, Applied Physics Letters **88**, 083101 (2006).

[39] M. Julier, A. Vinattieri, M. Colocci, P. Lefebvre, B. Gil, D. Scalbert, C. A. Tran, r. F. Karlicek, Jr., and J.-P. Lascaray, *Slow spin relaxation observed in InGaN/GaN multiple quantum wells*, Physica Status Solidi (b) **216**, 341 (1999).

[40] N. J. Harmon, W. O. Putikka, and Robert Joynt, *Prediction of extremely long mobile electron spin lifetimes at room temperature in wurtzite semiconductor quantum wells*, Applied Physics Letters **98**, 073108 (2011).

[41] A. Balocchi, Q. H. Duong, P. Renucci, B. L. Liu, C. Fontaine, T. Amand, D. Lagarde, and X. Marie, *Full Electrical Control of the Electron spin relaxation in GaAs quantum wells*, Physical Review Letters **107**, 136604 (2011).

[42] Animesh Banerjee, Fatih Dogan, Junseok Heo, Aurelien Manchon, Wei Guo, and Pallab Bhattacharya, *Spin relaxation in InGaN quantum disks in GaN nanowires*, Nano Letters **11**, 5396 (2011).

[43] M. Winkelnkemper, R. Seguin, S. Rodt, A. Schiliwa, L. Reibmann, A. Strittmatter, A. Hoffmann, and D. Bimberg, *Polarized emission lines from A- and B-type excitonic complexes in single InGaN/GaN quantum dots*, Journal of Applied Physics Letters **101**, 113708 (2007).

[44] C. Y. Hu, K. Morita, H. Sanada, S. Matsuzaka, Y. Ohno, and H. Ohno, *Spin precession of holes in wurtzite GaN studied using the time-resolved Kerr rotation technique*, Physical Review B **72**, 121203(R) (2005).

[45] M. Bayer, A. Kuther, A. Forchel, A. Gorbunov, V. B. Timofeev, F. Schafer, J. O. Reithmaier, T. L. Reinecke, and S. N. Walck, *Electron and hole g-factors and exchange interaction from studies of the exciton fine structure in* $In_{0.60}Ga_{0.40}As$ *quantum dots.* Physical Review Letters, 82, 1748 (1999).

[46] M. Paillard, X. Marie, P. Renucci, T. Amand, A. Jbeli, and J. M. Gérard, *Spin Relaxation Quenching in Semiconductor Quantum Dots*, Physical Review Letters **86**, 1634 (2001).

[47] E. Tsitsishvili, R. v. Baltz, and H. Kalt, *Temperature dependence of polarization relaxation in semiconductor quantum dots*, Physical Review B **66**, 161405 (2002).

[48] A. Bonnot, R. Planel, and C. B. à la Guillaume, *Optical orientation of excitons in CdS*, Physical Review B **9**, 690 (1974).

[49] F. Meier and B. P. Zakharchenya, *Optical Orientation*, Elsevier Science Ltd (1984), ISBN 0444867414.

[50] T. Amand, X. Marie, P. Le Jeune, M. Brousseau, D. Robart, J. Barrau, and R. Planel, *Spin Quantum Beats of 2D Excitons*, Physical Review Letters **78**, 1355 (1997).

[51] D. Gammon, E. S. Snow, B. V. Shanabrook, D. S. Katzer, and D. Park, *Homogeneous Linewidths in the optical spectrum of a single Gallium Arsenide quantum dot*, Science **273**, 87 (1996).

[52] M. Bayer, G. Ortner, O. Stern, A. Kuther, A. A. Gorbunov, A. Forchel, P. Hawrylak, S. Fafard, K. Hinzer, T. L. Reinecke, *Fine structure of neu-*

tral and charged excitons in self-assembled In(Ga)As/(As)GaAs quantum dots, et al., Physical Review B **65**, 195315 (2002).

[53] C. Kindel, S. Kako, T. Kawano, H. Oishi, Y. Arakawa, G. Hönig, M. Winkelnkemper, A. Schliwa, A. Hoffmann, and D. Bimberg, *Exciton fine-structure splitting in GaN/AlN quantum dots*, Physical Review B **81**, 241309 (2010).

[54] P. Tronc, V. P. Smirnov, and K. S. Zhuravlev, *Symmetry of electron states and optical transitions in GaN/AlN hexagonal quantum dots*, Physica Status Solidi (b) **241**, 2938 (2004).

[55] L. Largeau, D. L. Dheeraj, M. Tchernycheva, G. E. Cirlin, and J. C. Harmand, *Facet and in-plane crystallographic orientations of GaN nanowires grown on Si(111)*, Nanotechnology **19**, 155704 (2008).

[56] E. L. Ivchenko, *Fine structure of excitonic levels in semiconductor nanostructures*, Physica Status Solidi (a) **164**, 487 (1997).

[57] H. Tong and M. W. Wu, *Theory of excitons in cubic III-V semiconductor GaAs, InAs and GaN quantum dots: fine structure and spin relaxation*, Physical Review B **83**, 235323 (2011).

[58] S. Nagahara, M. Arita, and Y. Arakawa, *No temperature dependence of spin relaxation in InGaN phase-separated quantum dots*, Applied Physics Letters **88**, 083101 (2006b).

[59] Y. Yin and M. W. Wu, *Electron spin relaxation induced by confined phonons in nanowire-based quantum dots*, Journal of Applied Physics **108**, 063711 (2010).

[60] M. Sénès, B. Urbaszek, X. Marie, T. Amand, J. Tribollet, F. Bernardot, C. Testelin, M. Chamarro, and J.M. Gérard, *Exciton spin manipulation in InAs/GaAs quantum dots: Exchange interaction and magnetic field effects*, Physical Review B **71**, 115334 (2005).

Chapter 4

Spin-dependent recombination effect in Ga implanted InGaAs

Contents

4.1 Spin dependent recombination effect 87

4.1.1 The Spin dependent recombination mechanism 87

4.1.2 Manifestation of Spin Dependent Recombination in (In)GaAsN 90

4.1.3 Origin of the deep paramagnetic centres 93

4.2 Ion implanted semiconductor InGaAs for SDR-based devices 94

4.2.1 Why ion implanted InGaAs 94

4.2.2 Sample 95

4.3 Spin dynamics of InGaAs ion implanted 95

4.3.1 Evidence of the Spin Dependent Recombination 98

4.3.2 Ion implantation dose dependence 100

4.3.3 Magnetic field effects 101

4.4 Conclusion 103

Bibliography 105

In the previous chapter we have shown that a substantial quenching of the spin relaxation mechanism of carriers in semiconductors can be achieved in wide-gap nitride nanostructures. In this chapter a different approach is adopted to achieve the same goal. This consists in the engineering of paramagnetic defects. Whereas in nanostructures it is the reduction of the dimensionality which is at the base of the quenching of the exciton spin relaxation mechanism, here it is the spin dependent recombination of electrons on paramagnetic defects which is at the heart of the mechanism.

The dependence of the recombination time on the relative spin orientation of carriers on paramagnetic centres in semiconductors, namely the spin dependent recombination (SDR), has been known for over 40 years in different materials. It is however in dilute nitride GaAsN that the SDR manifests itself with record high values at room temperature in photoluminescence and photoconductivity experiments, suggesting practical applications of the SDR as a spin filter in dilute nitrides. The demonstration by optically detected magnetic resonance (ODMR) spectroscopy that it is nitrogen-induced Ga interstitial defects which is at the origin of the SDR, has opened up the possibilities to design new SDR active compounds.

In this chapter we propose a novel methodology based on the ion implantation of gallium atoms to create deep paramagnetic centres in nitrogen-free semiconductors to overcome the limitation of the dilute nitride approach. We will first concisely review the SDR mechanism and its optical manifestations in dilute nitride semiconductors (In)GaAsN. We will then introduce our approach to the selective creation of paramagnetic centres and present its advantages in terms of spatial resolution, wavelength emission and efficiency control. The optimum implantation conditions for the most efficient SDR are then determined by the analysis of different ion doses spanning four orders of magnitude. Finally, we will present the effect on the SDR efficiency of the application of a weak external magnetic field to the sample and some preliminary conclusions which suggest the appearance of paramagnetic centre nuclear spin polarisation.

4.1 Spin dependent recombination effect

The Spin Dependent Recombination (SDR) in semiconductors, *i.e.* the dependence of the recombination time on the relative spin orientation of photogenerated carriers on paramagnetic centres, has been known for over 50 years since the optically detected magnetic resonance (ODMR) experiments performed on Al_2O_3 [1]. It has been subsequently observed in a variety of materials: in amorphous or crystalline silicon [2–5], in silicon p-n junctions [6–8], GaAlAs [10] and GaAs [11]. It is however only recently that the attention has focused on the observation of the SDR in (Al)(In)GaAs-based dilute nitride materials due to the measurement of high record values at room temperature in photoluminescence and photoconductivity experiments [13–26].

4.1.1 The Spin dependent recombination mechanism

The mechanism of SDR effect originates from the Pauli Exclusion Principle. The key point is the existence of deep paramagnetic centres with an energy level in the semiconductor gap, *i.e.* defect centres possesses a single electron of randomly oriented spin at thermodynamic equilibrium. The deep centres spin polarisation ($P_{Centres}$) is therefore defined $P_{Centres} = \frac{N_+ - N_-}{N_+ + N_-}$ where N_+/N_- are the numbers of electron with spin up/down in the centres. At thermodynamic equilibrium $P_{Centres} = 0$. The SDR theoretical model was initially developed by Weisbuch and Lampel in GaAlAs [10]. It can be schematically depicted as in figure 1 and explained as follows.

(i) We first suppose that we excite spin polarised electrons from the valence band (VB) to the conduction band (CB) thanks to a circularly polarised laser excitation (σ^+, figure 4.1a). It is assumed here that the excitation creates 100% CB spin polarisation for the sake of simplicity (as could be done *e.g.* in a sample under uniaxial strain).

(ii) Due to the Pauli exclusion principle, the capture of a CB electron on the centres is dependent on the relative spin orientation of the free and deep centre resident electrons: if the photogenerated and centre's electrons have parallel spins the capture is forbidden (it is generally assumed that the triplet levels are not bound). On the contrary, if their relative spins are anti-parallel, the capture resulting in the formation of a spin singlet is very efficient, typically on the order of a few picoseconds. The electron capture process is therefore *spin dependent*.

(iii) After the capture, the deep centres can annihilate one of the electrons of either spin direction through a recombination with an unpolarised valence band hole (the hole spin relaxation time is very fast, of the order of 1 ps[1].This recombination is thus *spin independent* and it leaves the centre again with a single resident electron.

(iv) Since the free-electron capture on the centre is spin-dependent but the recombination process of the trapped electrons on the centre is spin-independent, this leads to a dynamic polarisation of the centres with the same sign as the photogenerated electron spins (fig 4.1c), *i.e.* $P_{Centres} \times P_{free} > 0$.

(v) Once the centres are fully spin polarised, no more CB electrons can be captured, provided that the centre polarisation is preserved during the CB electron spin lifetime. In this regime the system operates as a spin filter: a spin-flipped electron is immediately captured by the spin polarised deep centres and a high spin polarisation of the CB electrons is maintained.

The situation is however completely different if the sample is excited by a linearly polarised excitation (fig 4.1d). Now, no CB spin polarisation can be created as an equal number of spin-up and spin-down electrons is created. These unpolarised free electrons can be all captured by the unpolarised deep centres with equal probability and no centre spin polarisation can be achieved (figure 4.1e and f).

It is clear that the SDR strongly affects the density and polarisation of CB electrons and therefore influences the photoconductivity [2–7,20,24] and photoluminescence [10,11,13,16–19,21,25] properties of the materials. A stronger intensity and polarisation is expected for the band-to-band photoluminescence under a circularly polarised excitation compared to a linearly polarised one. A convenient parameter to characterise the SDR effect is the Spin Dependent Recombination Ratio defined as:

$$\mathrm{SDR_r} = \frac{I^+}{I^X} \tag{4.1}$$

where I^+ and I^X indicate respectively the total photoluminescence (or photoconductivity) intensities recorded under a circularly and linearly polarised excitation of the same irradiance. In the absence of the SDR mechanism, $\mathrm{SDR_r} = 1$ whereas in its presence $\mathrm{SDR_r} > 1$. In the following section we will briefly review some the experimental evidences of the SDR by photoluminescence spectroscopy.

---

[1] Because of the very large of effective mass of holes, the fourfold degeneracy of the valence band in $\vec{k} = \vec{0}$ and the large spin-orbit coupling in III-V semiconductors, the hole spin relaxation time is much shorter than the electron's [9,12,13].

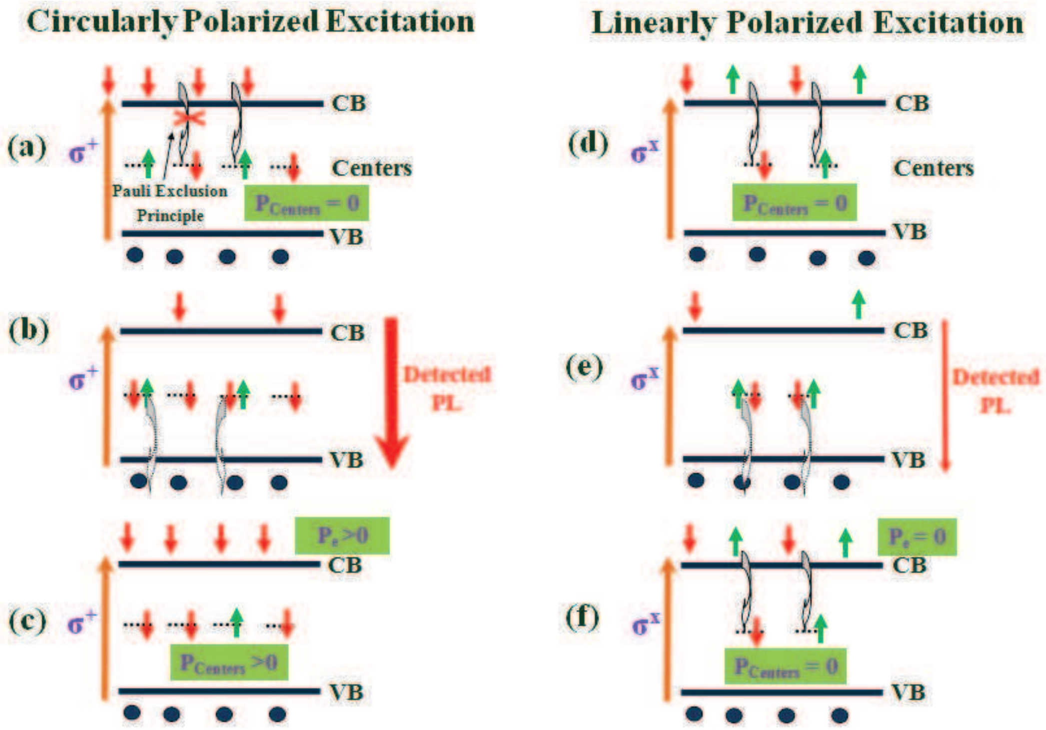

Figure 4.1: *Schematic representation of the SDR mechanism under circular (left panel) and linear (right panel) excitations. Figure a (d) correspond to the state at* $t = 0$ *just after optical excitation, figure b (e) represent the state after the capture of free electrons on deep paramagnetic centres, and figure c (f) correspond to the state after few circles of capture of free electrons in the CB and recombination of electrons in the centres with holes in the VB. To simplify, we assume here that the polarisation of the photogenerated electrons in the CB under circularly polarised excitation is 100%.*

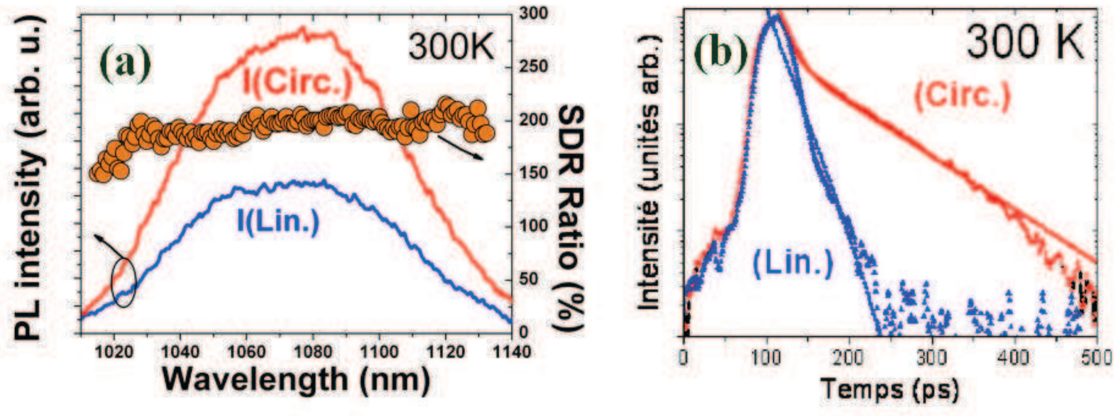

Figure 4.2: *(a) The time-integrated total PL intensity of dilute nitride semiconductor* $GaAs_{1-y}N_y$ *(y = 2.1 %) under circularly (red line)/linearly (blue line) polarised excitations and the corresponding SDR ratio (orange circles) for* P_{exc} *= 20 mW, T= 300 K. (b) The corresponding time evolution of total PL intensities [17].*

4.1.2 Manifestation of Spin Dependent Recombination in (In)GaAsN

4.1.2.1 The enhancement of PL Intensity and carrier life time

The most remarkable manifestations of the SDR-based effect in dilute nitride is the very large enhancements of the PL intensity and carrier life time under circularly polarised excitation as compared to under linearly polarised excitation even at room temperature. As explained in the previous section, this is due to the fact that under a circularly polarised excitation, the deep paramagnetic centres can be dynamically spin-polarised blocking any further capture of CB electrons. Contrary to a linearly polarised excitation where the CB electron lifetime is controlled by the efficient defect capture, a higher density of spin polarised electron can be maintained in the CB under a circularly polarised one.

Figure 4.2 reports the time integrated (left) and dynamics (right) of the PL intensities under a circular and linear excitations of the same power (P_{exc}=20 mW) measured on a $GaAs_{0.979}N_{0.021}$ epilayer at room temperature [17]. We observe a factor of two increase of the total PL intensity and a fourfold increase of the PL decay time (from $\tau_{PL} \approx 20$ ps to $\tau_{PL} \approx 85$ ps) by changing the excitation polarisation from linear to circular. Quantitatively very similar results have been obtained in several dilute nitride epilayers with different nitrogen concentrations [21] and in (In)GaAsN/GaAs quantum wells [16, 25].

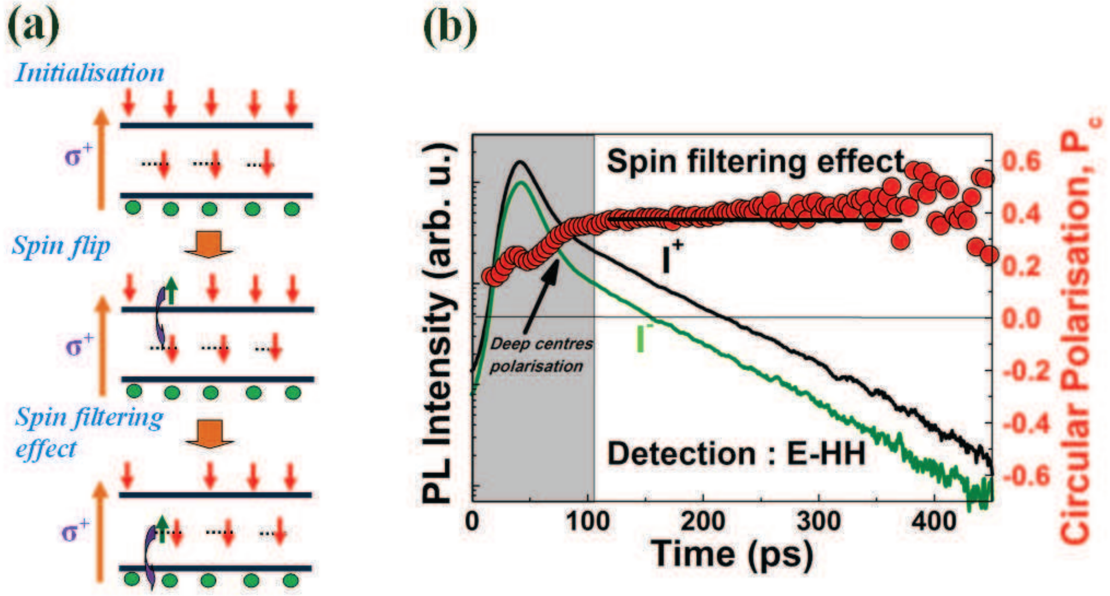

Figure 4.3: *(a) The schematic mechanism of the spin filtering effect. After being polarised (Fig. 4.1c), the deep paramagnetic centres act as a spin filter which maintains the high CB electron spin polarisation. (b)The time evolution of the co- and counter-polarised components of the PL intensity after a circularly polarised excitation and the corresponding circular polarisation degree in* $GaAs_{1-y}N_y$ *(*y *= 2.1 %) at 300 K,* P_{exc}*= 20 mW. The spin filtering effect is clearly observed [17].*

4.1.2.2 Spin filtering effect

The SDR effect does not only control the PL decay time but it can also be exploited as a CB electron spin filter to produce or maintain a high CB electron spin polarisation. Again, under a circularly polarised excitation and once the deep paramagnetic centres are spin-polarised, if a CB electron for any reason flips its spin to the opposite orientation, it will be immediately captured by the spin-polarised deep centres. This capture therefore maintains a high spin polarisation in the CB, only the total PL intensity is affected - this is the Spin filtering effect. The schematic mechanism of the spin filtering process is shown in figure 4.3(a).

It is possible to trace in time the dynamical spin polarisation of the paramagnetic centres and the subsequent spin filtering effect by time resolved PL spectroscopy. Figure 4.3(b) reports the dynamics of the co- and counter-polarised photoluminescence intensities under a circularly polarised excitation and the corresponding circular polarisation degree measured at room temperature. During the first tens of picoseconds, the circular polarisation degree of the PL, reflecting the CB electron spin polarisation, gradually increases as the centres becomes spin polarised. A stable PL circular polarisation is then obtained, $P_C = 40\%$, greater than its initial value. The apparent electron spin lifetime τ_s^* ($\sim$ 2 ns) is here much longer than the PL lifetime ($\tau_{PL} \sim$ 100 ps), and the electron spin life time under weak excitation power ($\tau_s^* \sim$ 100 ps - see next section).

4.1.2.3 Power dependence

To observe the spin filtering effect it is necessary that the density n_e^{CB} of the photogenerated CB electrons to be greater than the paramagnetic centre one n_e^{PC}; it would be otherwise impossible to achieve complete deep centres spin polarisation[2]. The remaining unpolarised centres would operate as spin-insensitive non-radiative traps for the CB electrons. No difference in terms of band-to-band PL intensity and lifetime would be observed under a circular or linear excitation and no spin filtering effect would be visible. This lead to a strong power dependence of the SDR effect. The experimental evidences are reported in figures 4.4(a) and (b). Figure 4.4(a) reports the low temperature power dependence of the PL circular polarisation dynamics under a circularly polarised excitation. As long as $n_e^{CB} < n_e^{PC}$ (P_{exc} <5mW for this sample), the decay time $\tau_s \approx$100 ps of the PL circular polarisation degrees is well explained in term of the D'Yakonov-Perel mechanism and is consistent with the electron spin relaxation time typically measured in GaAs and other III-V compounds [2, 27, 28]. As the photogenerated carrier density increases, the spin filtering regime is progressively reached. The maximum P_C is attained for $P_{exc} = 30$ mW. At this excitation power, a stable P_C is observed reflecting the efficacy of the spin filtering effect of the paramagnetic centres. The strong power dependence of the SDR effect is also observed by measuring the evolution of the SDR ratio as a function of the excitation power (Fig 4.4(b)). Consistently with what observed in figure 4.4(b), firstly the SDR ratio increases dramatically to its maximum value ($SDR_r \sim 500\%$) for $P_{exc} \approx 30mW$. It then decreases slowly for higher excitation powers. At low excitation powers (P_{exc} <30 mW), the photogenerated electron concentration in the CB is not enough to polarise all the deep paramagnetic centres ($n_e^{CB} < n_e^{PC}$). The slight decrease of the SDR$_r$ for higher excitation powers correspond to the condition $n_e^{CB} > n_e^{PC}$: the excess CB electrons cannot be efficiently spin filtered by an insufficient density of paramagnetic centres. In this case, the electrons recombine through non-SDR processes (bimolecular, non-paramagnetic centres,...).

---

[2] Here we also assume that: the capture time is very short compared to the radiation time and the electron spin life time in the CB ($\tau_{capture} \ll \tau_{rad}$, τ_s^{cond}); and the trapped electron spin life time is longer than the radiation time ($\tau_s^{trap} \gtrsim \tau_{rad}$).

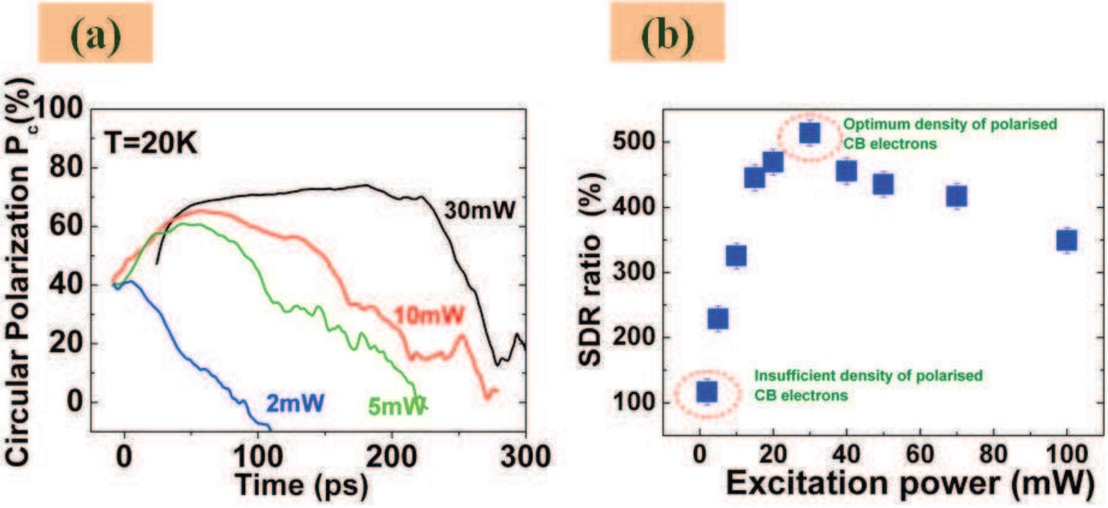

Figure 4.4: *The power dependence (a) of the photoluminescence circular polarisation dynamics and (b) of the SDR ratio in* $GaAs_{1-y}N_y$ *(*y *= 2.1 %) at* T *= 20 K [21].*

4.1.3 Origin of the deep paramagnetic centres

The Spin Dependent Recombination in dilute nitride has been actively investigated during the past decade. The crucial role of the nitrogen incorporation in (Al)(In)GaAs epilayers or quantum well has been underpinned by all authors. For example Lombez *et.al.* [16] observed a 20-fold increase of the CB electron spin relaxation time in nitrogen-containing InGaAsN/GaAs quantum well compared to nitrogen free structures. Zhao *et.al.* [21] observed a correlation between the optimum excitation power for observing the maximum SDR_r and the nitrogen concentration in the range from 0.76 % to 2.6 %. It is however only very recently [23] that the nature of the paramagnetic centres has been clarified by our group in collaboration with the group of Prof. W. Chen in the University of Linköping, Sweden. By using Optically Detected Magnetic Resonant experiments (Fig. 4.5) it has been demonstrated that it is actually nitrogen-induced gallium self-interstitial Ga^{2+} that plays the role of the deep paramagnetic centre.

The knowledge of the origin of the deep paramagnetic centres offers a unique possibility of tailoring the spin filtering effect: the defect engineering approach. The key point behind this approach is the possibility of systematically controlling the density and position of the paramagnetic centres by an "ad-hoc" insertion of gallium interstitial defects in (Al)(In)GaAs compound without the need of nitrogen. This approach constitutes the central result of this chapter. The motivation and the experimental evidence behind this novel approach will be developed in the following sections.

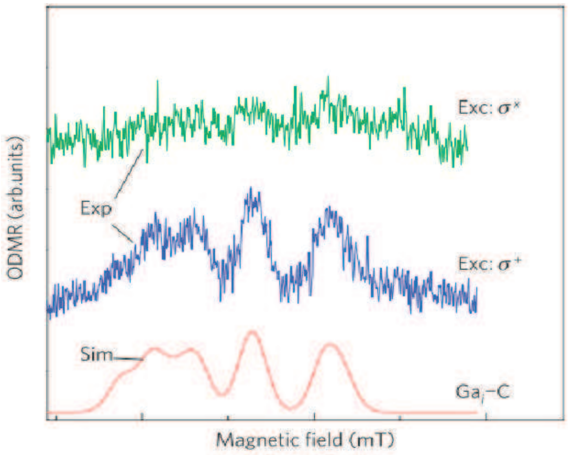

Figure 4.5: *The optically detected magnetic resonance (ODMR) spectra obtained by monitoring the total intensity of the band-to-band PL from a* $GaN_{0.021}As_{0.979}$ *epilayer, obtained at 3K under linear* (σ^X) *and circular* (σ^+) *excitation at 850 nm. A simulated ODMR spectrum of the* Ga_i *defect (denoted by* Ga_i-C*) is also shown. The excellent correspondence between the experimental and simulated spectra confirms the origin of the paramagnetic centres [23].*

4.2 Ion implanted semiconductor InGaAs for SDR-based devices

4.2.1 Why ion implanted InGaAs

Dilute nitride InGaAsN materials have been mainly investigated for the realization of devices for the telecommunication spectral windows ($\lambda \approx 1.3$ and 1.55 μm) [31–33] thanks to their widely adjustable band gap. However, the presence of N induces not only paramagnetic centres but an ensemble of other defects and clusters which largely decrease the mobility of the CB electrons, and moreover strongly affects the CB electron population due to their efficient capture capacities. The large density of the N-induces defects is a clear disadvantage for optoelectronic applications of dilute nitride semiconductors [34,37]. For the purpose of realising a practical spin filtering device it is desirable, on one side, to dissociate the SDR efficiency from the photoluminescence (PL) emission wavelength and, on the other side, to be able to selectively create spin filtering active regions with specific in-plane spatial resolution. The aim of this work is to put forward a new methodology to create deep paramagnetic centres bypassing the need of N insertion in (In)GaAs compounds. To this aim, the ion implantation of gallium ion is proposed as a novel technique to create Ga^{2+} interstitial paramagnetic defects in nitrogen-free InGaAs epilayers. This method avoids the giant band-bowing characteristic of the dilute nitrides and allows the creation of SDR active regions with arbitrary patterns and efficiency by controlling the implantation conditions. As it relies on the post-growth creation of interstitial paramagnetic centres, this technique is, in principle, transferable to other (In,Al)GaAs compounds allowing for the independent tuning of the emission wavelength and SDR efficiency.

4.2.2 Sample

Square number	Ga^{2+} Ion dose (cm^{-2})
1	$1.8 \cdot 10^{12}$
2	$4.5 \cdot 10^{11}$
3	$7.25 \cdot 10^{10}$
4	$1.8 \cdot 10^{10}$
5	$4.5 \cdot 10^{9}$
6	$7.25 \cdot 10^{8}$
7	$1.8 \cdot 10^{8}$

Table 4.1: *The Ga^{2+} ion surface doses used to implant the sample.*

The sample under study was grown by molecular beam epitaxy (MBE) on a semi-insulating (001)-oriented GaAs substrate. The structure of the sample is shown in the figure 4.6 (a). A 50 nm-thick $In_{0.09}Ga_{0.91}As$ active layer was grown on top of 100 nm $Al_{0.25}Ga_{0.75}As$ barrier and 10 nm GaAs spacing layers. The sample was then covered by a 5 nm thick GaAs cap layer. Seven different 200 μm side square regions were uniformly implanted, using a 35 keV focused ion beam probe transporting 3 pA. The digital scanning speed, dwell times, and pixel-to-pixel distance were adjusted to provide surface doses ranging from $1.8 \cdot 10^8$ ion/cm^2 to $1.8 \cdot 10^{12}$ ion/cm^2 (table 4.1). The acceleration energy of the Ga ions and the InGaAs layer distance from the surface were chosen in order to selectively create the deep paramagnetic centres only in the InGaAs part while maintaining good optical qualities. The growth and implantation were performed by J-C. Harmand and collaborators at LPN, CNRS, Marcoussis, France.

4.3 Spin dynamics of InGaAs ion implanted

Time- and polarisation-resolved spectroscopy was again employed to evidence the SDR phenomena at low temperature in the implanted InGaAs layers. The

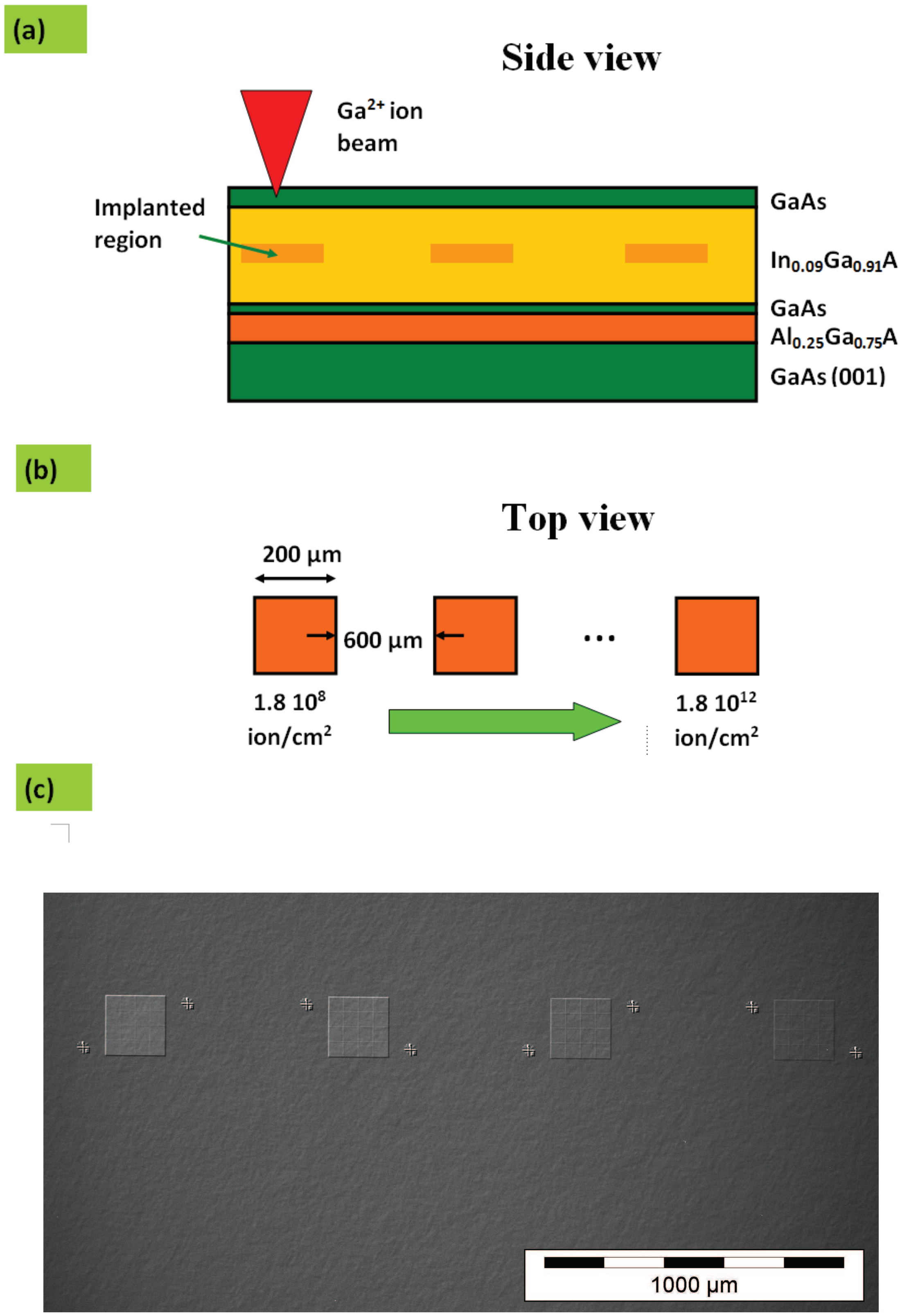

Figure 4.6: *(a) Side view - the sample structure grown on a GaAs substrate. (b)Top view - the schematic configuration of squares with different implanted ion doses and (c) SEM image of four of the seven squares.*

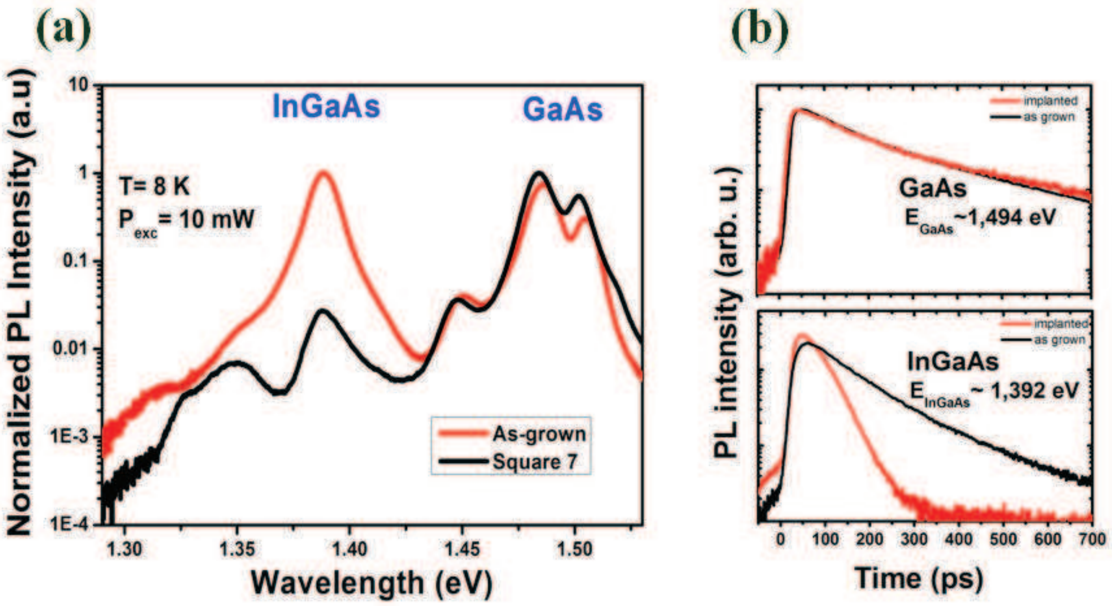

Figure 4.7: *(a) The normalised time integrated PL intensities of as-grown (non implanted) and implanted (square 7) samples under a circularly polarised excitation at* $T = 8$ *K and* $P_{exc} = 10$ *mW. The spectra components of GaAs and InGaAs are noted. (b) The normalised time evolution of PL intensities originating from GaAs and InGaAs in as-grown (black line) and implanted (red line) samples at low temperature.*

excitation beam, propagating parallel to the growth axis, was focused to a 30 μm spot diameter and the excitation energy was set to 1.57 eV ($\sim$ 790 nm) - higher than energy bandgap of GaAs (E_g=1.52 eV at 0K [30]) and InGaAs. This energy was chosen to induce absorption in both the GaAs spacing layer and in the implanted InGaAs regions in order to evidence the selectivity of the ion implantation. An average power ranging from 1 to 30 mW was used.

It has been possible to measure a PL signal from all the squares except for those implanted with highest doses ($1.8 \cdot 10^{12}$ cm^{-2} and $4.5 \cdot 10^{11}$, squares 1 and 2) for which the ion-induced damages were too important to observe a clear luminescence. As an example, figure 4.7(a) reports the normalised time integrated PL intensity measured on the as-grown and implanted samples (square 7) at low temperature. The respective PL spectra contain features related both to the GaAs and InGaAs layers. The spectral feature in the 1.43 eV to 1.53 eV region origins from the GaAs layer. The main peak centred at about 1.48 eV ($\sim$ 837 nm) is identified as resulting from the near band edge and defect-related emission from GaAs. The spectral feature centered at $\sim$1.385 eV is unambiguously assigned to the luminescence emitted by the InGaAs layer. The small peak at $\sim$ 1.35 eV is tentatively assigned to the longitudinal optical phonon replica of the main peak of InGaAs ($E_{LO} \sim 34$ meV [35]).

By comparing the relative intensities of the GaAs and InGaAs spectral features in the as-grown and implanted samples (figure 4.7(a)) and the relative PL lifetime τ_{PL} (figure 4.7 (b)), we can evidence that, as predicted, the implantation has affected almost exclusively the InGaAs-related emission.

4.3.1 Evidence of the Spin Dependent Recombination

We present here the results obtained on the sample implanted with $4.5 \cdot 10^9$ cm^{-2} ion density at T=25 K. The temperature was chosen in order to maintain a strong PL intensity. Qualitatively, similar results were obtained on all the other implanted regions except, as previously stated, for the two highest doses for which the ion-induced damages were too important to observe a clear luminescence. Figure 4.8 reports the time integrated PL intensities under circular (σ^+) and linear (σ^X) excitations of the implanted region and the corresponding SDR ratio (circles) at $T = 25$ K and $P_{exc} = 10$ mW. The figure 4.8 reproduces additionally the SDR ratio (squares) of the as-grown sample. A much stronger PL intensity is measured under a circularly polarised excitation compared to a linearly polarised one, corresponding to a Spin Dependent Recombination ratio SDR$_r$ = 240 %. This PL intensity enhancement under circularly polarised excitation is absent (SDR = 100% within the experimental uncertainties) from the GaAs and un-implanted InGaAs (squares) related emissions. The measured SDR value is consistent with what was reported for dilute nitride (In)GaAsN systems. These results provide a twofold confirmation:

(i) The feasibility of the ion implantation to create paramagnetic centres in nitrogen-free materials;

(ii) This technique can provide a vertical and horizontal spatial selectivity.

Figure 4.9 reports the temporal evolution of PL intensity under a circularly (black line)/linearly (gray line) polarised excitation and the corresponding SDR ratio (red circles) for the same experimental conditions, measured at the peak of the PL intensity related to the InGaAs layer. A rapid increase of the SDR ratio is observed reaching values as high as 380% as the spin filtering regime is progressively reached in the first picoseconds after the excitation. The subsequent SDR decline reveals the onset of an insufficient CB population and defect spin polarisation necessary to sustain the process due to the band-to-band recombination. The ensemble of these observations is consistent with the creation of paramagnetic centres by Ga ion implantation.

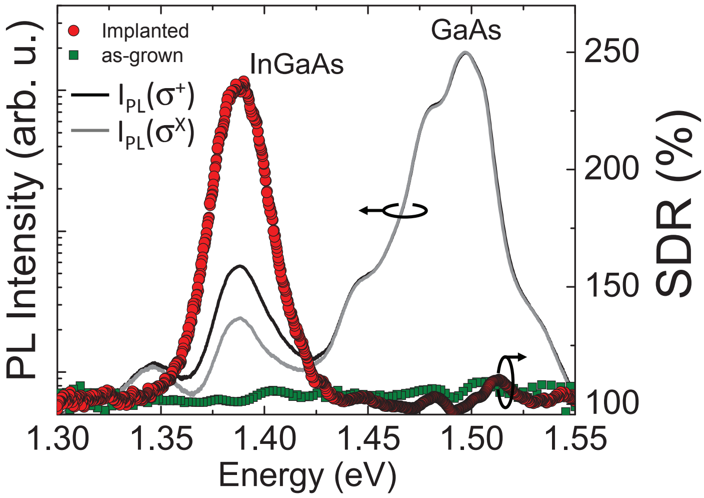

Figure 4.8: *The time integrated PL intensities of the sample with ion dose* $4.5 \cdot 10^9$ cm^{-2} *under circular (black line) and linear (grey line) excitation and the corresponding SDR ratios (red circles) at* $T = 25K$ *and* $P_{exc} = 10mW$. *The green squares represent the SDR ratio observed for the as-grown sample.*

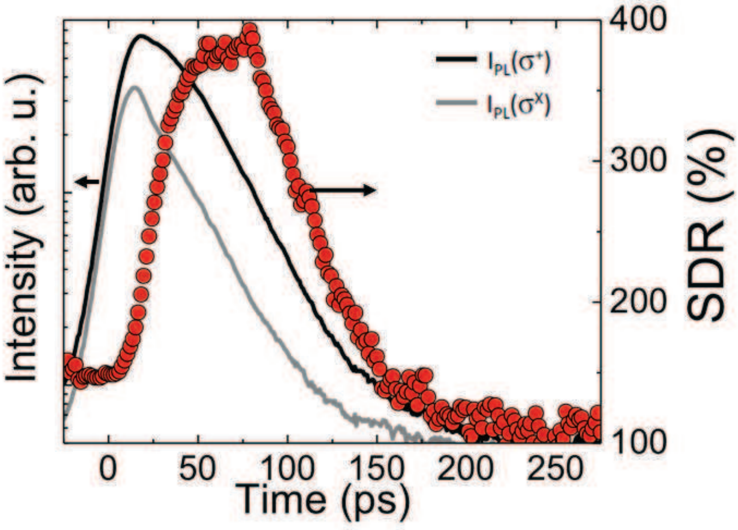

Figure 4.9: *The time evolution of PL intensity under circularly (black line)/linearly (gray line) polarised excitation and the dynamics of the corresponding SDR ratio (red circles).*

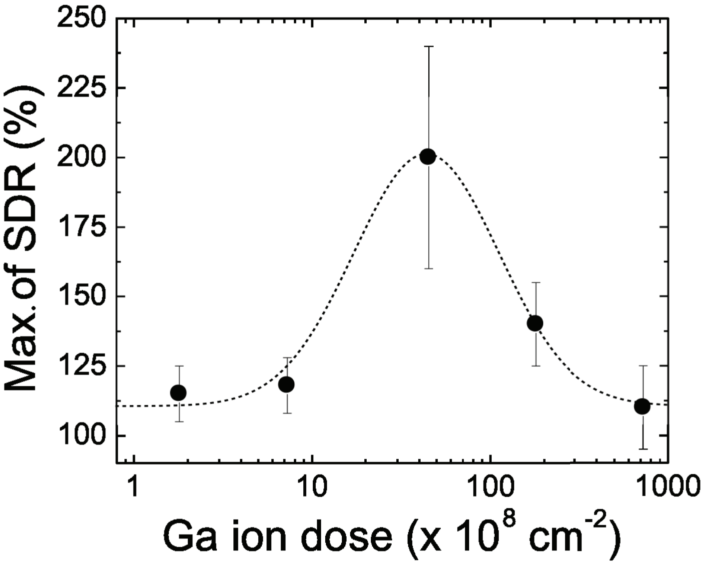

Figure 4.10: *The evolution of the maximum SDR ratio as a function of the implantation dose. For each dose, the error bars are deduced from the inhomogeneity of the measured SDR ratio as observed in the same implanted square regions. The Ga ion dose which produces the highest SDR ratio is* $5 \cdot 10^9$ *ion/cm*$^{-2}$.

4.3.2 Ion implantation dose dependence

The aim of this work is to create deep paramagnetic centres by gallium ion implantation and therefore propose a new technique to produce spin filtering materials based on the SDR effect. An important question is how the ion implantation process impact the SDR-based effect in the sample. Figure 4.10 reports the maximum SDR ratio measured at the optimum optical excitation power as a function of the implantation dose. For each dose, the error bars are deduced from the inhomogeneity of the measured SDR ratio as observed in the same implanted square region. The Ga^{2+} ion dose which produces the highest SDR ratio is $5 \cdot 10^9$ cm^{-2}. At lower doses, the ion implantation creates too few deep paramagnetic centres, and the spin dependent recombination takes a very small part in the recombination process. At higher doses, the competition between the paramagnetic centres and other ion-induced defects progressively reduces the SDR effect. This is confirmed by the important degradation of the PL intensity for doses above 10^{10} cm^{-2}. Indeed a complete disappearance of any measurable PL signal is obtained at the two highest implantation doses ($4.5 \cdot 10^{11}, 1.8 \cdot 10^{12}$ cm^{-2}) used in this work.

Taking into consideration the optimum density of Ga ions ($5 \cdot 10^9$ cm^{-2}) determined here and assuming for simplicity 100% efficiency for the creation of Ga^{2+}

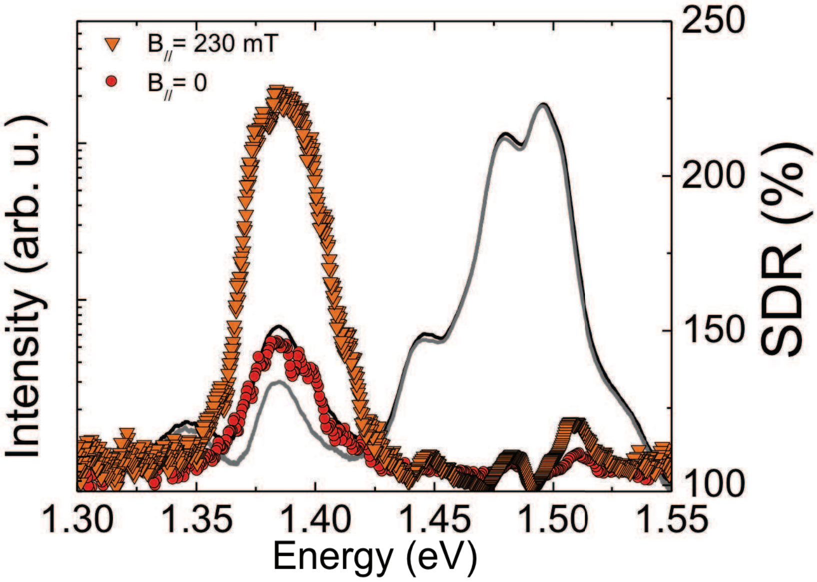

Figure 4.11: *The photoluminescence spectra of square 5 (ion implanted* $4.5.10^9$ */cm^{-2}) under circular (σ^+)/linear(σ^x) excitations ($P_{exc} = 5mW, T = 25K$) and corresponding SDR ratios with ($B_{\|} = 230mT$) and without external magnetic field in Faraday geometry.*

interstitial by focused ion beam in the 50 nm thick InGaAs layer, we can estimate that the density of paramagnetic centres created is in the order of 10^{15} cm^{-3} which corresponds to the same order of magnitude as the one deduced in previous works on dilute nitrides [17, 19]. This strengthen the assignment of the nature of the paramagnetic centres to Ga^{2+} interstitials.

4.3.3 Magnetic field effects

To further support the proof of a successful creation of paramagnetic defects in our sample, we investigated the effect of an external magnetic field in Faraday geometry (magnetic field parallel to the propagating direction of the incident light) on the SDR ratio. Figure 4.11 shows the time integrated PL intensity spectra and the corresponding SDR ratio (orange triangles) under the application of a Faraday magnetic field $B_{ext} = 230$ mT under a circularly and a linearly polarised excitation for the $4.5 \cdot 10^9$ cm^{-2} ion density sample. The red circles correspond to the observed SDR ratio under zero external magnetic field, with otherwise unchanged experimental conditions. The SDR increases significantly from 140% to 220% under an external magnetic field $B_{ext} = 230$ mT. The observed increase in the SDR ratio is entirely due to an enhancement of the PL intensity under circular excitation as

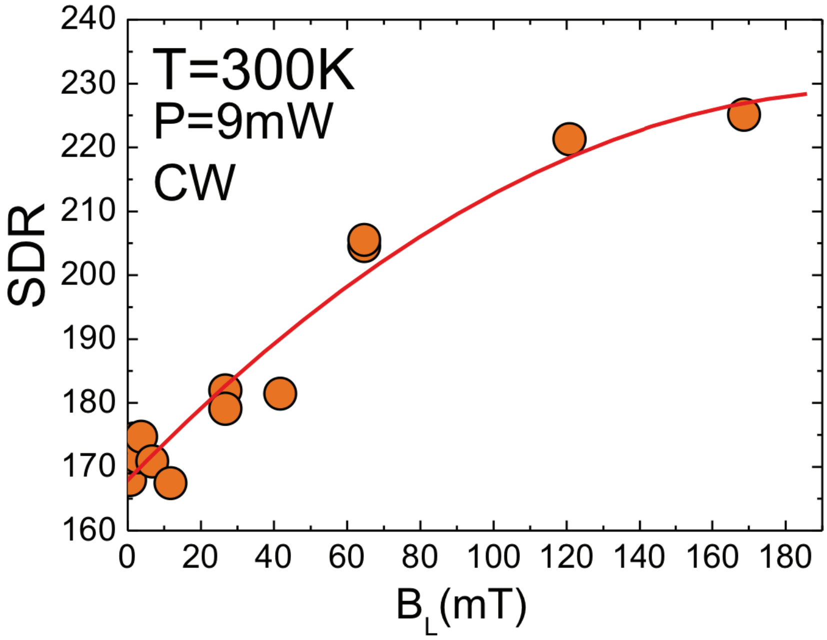

Figure 4.12: *The evolution of the SDR ratio as a function of the external magnetic field in Faraday geometry at room temperature for a* $GaAs_{0.993}N_{0.007}$ *sample.*

the PL intensity under a linearly polarised excitation remains unchanged. This observation suggests that the external magnetic field leads to an improvement of the spin filtering mechanism.

Earlier, the work of D. Paget *et al.* in semi-insulating and p-doped GaAs [11] and more recent experiments of V. K. Kalevich *et al.* in dilute nitride GaAsN epilayers [18, 19] have investigated the increased efficiency of the SDR effect under a weak external magnetic field (100 mT). The authors attributed the observed enhancement of the spin filtering effect to the suppression of the spin relaxation of the deep paramagnetic centres. This suppression was interpreted in terms of the spin orientation by hyperfine interaction of the nuclei surrounding the deep centres leading to the dynamical nuclear polarisation at room temperature.

We put forward another explanation: The paramagnetic electron and Ga nuclear spin are strong coupled by hyperfine interaction, leading to mixed electron-nuclear spin states [41]. When the magnetic field increases, a decoupling occurs as soon as the electron Zeeman effect overcomes the hyperfine interaction. This lead to an increase of the nuclear spin polarisation (see figure 4.12 for a $GaAs_{0.993}N_{0.007}$ sample where the effect was evidenced in our group) and simultaneously to an increase of the SDR effect.

4.4 Conclusion

From these results, it seems plausible to propose an alternative methodology to create spin dependent recombination regions in N-free semiconductors. Our method uses ion beam implantation of Ga^{2+} ions to create deep paramagnetic centres in selected regions in an InGaAs epilayer. We have successfully observed a SDR effect with SDR ratios as high as 240% at low temperature.

The enhancement of the SDR ratio produced by a weak external magnetic field in Faraday geometry has confirmed the role of the deep paramagnetic centre. The external magnetic field helps polarise the deep paramagnetic centres by decoupling the nuclear and trapped electron spins, and finally enhances the spin filtering properties. This result put forward the use of ion implanted GaAs-based materials as a model system for robust and long-lived spin memories in the form of nuclear spin polarisation.

These results, relying on the post-growth creation of Ga interstitial defects could be transferred to other Ga-based compounds allowing for the independent adjustment of the PL wavelength and SDR efficiency. The possibility of producing SDR active regions with arbitrary patterns by adjusting the implantation conditions could offer another degree of freedom for the design of possible spintronic devices relying on the spin filtering properties of deep paramagnetic defects.

Bibliography

[1] S. Geschwind, R. J. Collins, and A. L. Schawlow, *Optical detection of paramagnetic resonance in an excited state of* Cr^{3+} *in* Al_2O_3, Physics Review Letter **3** 545 (1959).

[2] Daniel J. Lepine, *Spin dependent recombination on silicon surface*, Physical Review B, **6**, 436 (1972).

[3] I. Solomon, D. Biegelsen and J. C. Knights, *Spin-dependent photoconductivity in n-type and p-type amorphous silicon.* Solid state communications **22**, 505 (1997).

[4] T. Wosinski and T. Figielski, *Spin-dependent recombination at dislocations in Silicon*, Physica status solidi (b) **71**, K73 (1975).

[5] T. Wosinski, T. Figielski, and A. Makosa, *Spin-dependent photoconductivity spectrum of dislocated silicon*, Physica status solidi (a) **37**, K57 (1976).

[6] I. Solomon, *Spin-dependent recombination in a silicon p-n junction*, Solid State Communications **20**, 215 (1976).

[7] D. Kaplan and M. Pepper, *Spin dependent surface recombination in silicon p-n junction: the effect of irradiation*, Solid State Communications **34**, 803 (1980).

[8] O. V. Tretyak, O. I. Kozonushchenko, K. V. Krivokhizha, A. S. Revenko, *Spin-dependent current in silicon p-n junction diodes*, Semiconductor Physics, Quantum Electronics & Optoelectronics **13**, 95 (2010).

[9] D. J. Hilton, C.L. Tang, *Optical orientation and femtosecond relaxation of spin-polarized holes in GaAs*, Physical Review Letter **89**, 146601 (2002).

[10] C. Weisbuch and G. Lampel, *Spin-dependent recombination and optical spin orientation in semiconductors*, Solid state communications, **14**, 141 (1974).

[11] Daniel Paget, *Optical-pumping study spin-dependent recombination in GaAs*, Physical review B, **30**, 931 (1984).

[12] B. Baylac, T. Amand, X. Marie, B. Dareys, M. Brousseau, G. Bacquet, V. Thierry-Mieg, *Hole spin relaxation in n-modulation quantum wells*, Solid State Communications, **93** 57 (1995).

[13] V. K. Kalevich, E. L. Ivchenko, M. M. Afanasiev, A. Yu. shiryaev, A. Yu. Egorov, V. M. Ustinov, B. Pal, and Y. Masumoto, *Spin-dependent recombination in GaAsN solid solutions*, Journal of Experimental and Theoretical Physics Letters **82**, 455 (2005).

[14] V. K. Kalevich, A. Yu. Shiryaev, E. L. Ivchenko, A. Yu. Egorov, L. Lombez, D. Lagarde, X. Marie, T. Amand, *Spin-dependent electron dynamics and recombination in* $GaAs_{1-x}N_x$ *alloys at room temperature*, Journal of Experimental and Theoretical Physics Letters **85**, 174 (2007).

[15] V. K. Kalevich, A. Yu. Shiryaev, E. L. Ivchenko, M. M. Afanasiev, A. Yu. Egorov, V. M. Ustinov, Y. Masumoto, *Hanle effect and spin-dependent recombination at deep centers in GaAsN*, Physica B **404**, 4929 (2009).

[16] L. Lombez, P.-F. Braun, H. Carrère, B. Urbaszek, P. Renucci, T. Amand, X. Marie, J. C. Harmand, and V. K. Kalevich, *Spin dynamics in dilute nitride semiconductors at room temperature.* Applied Physics Letters **87**, 252115 (2005).

[17] D. Lagarde, L. Lombez, X. Marie, A. Balocchi, T. Amand, V. K. Kalevich, A. Shiryaev, E. Ivchenko, and A. Egorov, *Electron spin dynamics in GaAsN and InGaAsN structures*, Physica status solidi (a) **204**, 208 (2007).

[18] V. K. Kalevich, M. M. Afanasiev, A. Yu. Shiryaev, and A. Yu. Egorov, *Amplification of spin-filtering effect by magnetic field in GaAsN alloys.* Physical Review B **85**, 035205 (2012).

[19] V. K. Kalevich, M. M. Afanasiev, A. Yu. Shiryaev, and A. Yu. Egorov, *Optical orientation of nuclei in Nitrogen alloys GaAsN at Room Temperature.* Journal of Experimental and Theoretical Physics Letters **96**, No 9, 567 (2012).

[20] F. Zhao, A. Balocchi, A. Kunold, J. Carrey, H. Carrère, T. Amand, N. Ben Abdallah, J. C. Harmand, and X. Marie, *Spin-dependent photoconductivity in nonmagnetic semiconductors at room temperature*, Applied Physics Letters **95**, 241104 (2009).

[21] F Zhao, A Balocchi, G Truong, T Amand, Z Marie, X J Wang, I A Buyanova, W M Chen and J C Harmand, *Electron spin control in dilute nitride semiconductors*, Journal of Physics: Condensed matter **21**, 174211 (2009).

[22] Fan Zhao, *Spin-dependent recombination in nitride dilute semiconductors*, PhD thesis, INSA Toulouse 2010.

[23] X. J.Wang, I. A. Buyanova, F. Zhao, D. Lagarde, A. Balocchi, X. Marie, C.W. Tu, J. C. Harmand and W. M. Chen, *Room-temperature defect-engineered spin filter based on a non-magnetic semiconductor*. Nature materials **8**, 198 (2009).

[24] A. Kunold, A. Balocchi, F. Zhao, T. Amand, N. Ben Abdallah, J. C. Harmand, and X. Marie, *Giant spin-dependent photo-conductivity in GaAsN dilute nitride semiconductor*, Physical Review B **83**, 165202 (2011).

[25] Y. Puttisong, X. J. Wang, I. A. Buyanova, H. Carrere, F. Zhao, A. Balocchi, X. Marie, C. W. Tu, and W. M. Chen, *Electron spin filtering by thin GaNAs/GaAs multiquantum wells*, Applied Physics Letters **96** 052104 (2010).

[26] E. L. Ivchenko, V. K. Kalevich, A. Yu. Shiryaev, M. M. Afansiev and Y. Masumoto, *Optical orientation and spin-dependent recombination in GaAsN alloys under continuous-wave pumping*, Journal of Physics: Condensed Matter **22** 465804 (2010).

[27] Thomas F. Boggess, J. T. Olesberg, C. Yu, Michael E. Flatté, and Wayne H. Lau, *Room-temperature electron spin relaxation in bulk InAs*, Applied Physics Letters, **77** 1333 (2000).

[28] A. V. Kimel, F. Bentivegna, V. N. Gridnev, V. V. Pavlov, R. V. Pisarev, and Th. Rasing, *Room-temperature ultrafast carrier and spin dynamics in GaAs probed by the photoinduced magneto-optical Kerr effect*, Physical Review B, **63** 235201 (2001).

[29] X.Marie, D. Lagarde, V. Kalevich, T. Amand, *Dilute III-V nitride semiconductors and Material Systems*, Chapter 11, Springer series in materials science **105**, Ayse Erol (editor) (2008).

[30] C. Kittel, *Introduction to Solid State Physics* p. 185, 6th Ed., New York:John Wiley (1986).

[31] Masahiko Kondow, Kazuhisa Uomi, Atsuko Niwa, Takeshi Kitatani, Seiji Watahiki and Yoshiaki Yazawa, *GaInNAs: A novel material for long-wavelength-range Laser diodes with excellent high-temperature performance*,Japanese Journal of Applied Physics **35**, 1273 (1996)

[32] Masahiko Kondow, Takeshi Kitatani, Shin'ichi Nakatsuka, Michael C. Larson, Kouji Nakahara, Yoshiaki Yazawa, Makoto Okai, and Kazuhisa Uomi,

GaInNAs: A novel material for long-wavelength semiconductor lasers, IEEE Journal of selected topics in Quantum electronics, Vol **3**, No 3 (1997).

[33] Masahiko Kondow, Takeshi Kitatani, Kouji Nakahara, Toshiaki Tanaka, *A 1.3-μm GaInNAs Laser diode with a lifetime of over 1000 hours*, Japanese Journal of Applied Physics **38**, L1355 (1999).

[34] S. Mazzucato and R. J. Potter, *Dilute III-V nitride semiconductors and Material Systems*, Chapter 7, Springer series in materials science **105**, Ayse Erol (editor) (2008).

[35] D. Sicault, R. Teissier, F. Pardo and J.-L. Pelouard, *Experimental study of hot-electron inelastic scattering rate in p-type InGaAs*, Physical Review B, **6**, 121301R (2002).

[36] P. R. Chalker, T. J. Bullough, M. Gass, S. Thomas and T. B. Joyce, *The microstructural influence of nitrogen incorporation in dilute nitride semiconductors*, Journal of Physics: Condensed Matter **16**, S3161 (2004).

[37] H. E. Porteanu, O. Loginenko and F. Koch, *The dual role of nitrogen as alloying and confining element in GaAs-based dilute nitride semeconductors*, Journal of applied physics, **107**, 033714 (2010).

[38] E P O'Reilly, A Lindsay, P J Klar, A Polimeni and M Capizzi, *Trends in electronic structure of dilute nitride alloys*, Semiconductor science and technology **24**, 033001 (1999).

[39] Markus Weyers, Michio Sato and Hiroaki Ando, *Red shift of photoluminescence and absorption in dilute GaAsN alloy layers*, Japanese Journal of Applied Physics **31**, 853 (1992).

[40] J Wu, W Shan and W Walukiewicz, *Band anticrossing in highly mismatched III–V semiconductor alloys*, Semiconductor Science and Technology **17**, 860 (2002).

[41] Y. Puttisong, X. J. Wang, I. A. Buyanova, and W. M. Chen, *Effect of hyperfine-induced spin mixing on the defect-enabled spin blockade and spin filtering in GaNAs*, Physical Review B **87**, 125202 (2013).

Conclusions

This thesis work has focused on the study of the spin dynamics in semiconductor structures based on GaN and InGaAs. The key motivation behind it is the identification of semiconductor systems capable of maintaining a very long carrier spin polarisation. Two approaches have been investigated here: quantum confinement of carriers in quantum dots and the engineering of paramagnetic defects.

For the first approach, we have studied the optical orientation of the exciton spin in nanowire-embedded GaN/AlN quantum dots. We have observed the quenching of the exciton spin relaxation time and the temperature insensitivity of the exciton PL linear polarization degree. These results contrast with the temperature decrease of the linear polarization degree observed in other nitride-based QD systems. We have also investigated the angular dependence of the PL linear polarization. This analysis reveals the presence of independent families of QDs with orthogonal exciton eigenstates. We have finally developed a density matrix method to account for the experimental observations showing that the measured angular dependence is compatible with a distribution following symmetry C_{3v} or higher symmetry of the exciton dipole orientations or even a uniform distribution (C_∞).

The temperature insensitivity of the exciton spin in wide gap nanowire-embedded quantum dots could be thus proposed as a plausible candidate for possible spintronics-based processing. Nevertheless, these first demonstrations surely require further investigations both on theoretical and experimental levels.

In the second part of this thesis, we have demonstrated that active spin dependent recombination regions can be selectively created in N-free InGaAs epilayers by focus ion beam implantation of Ga ions. We have evidenced a sizable SDR-driven effect reaching values as high as 240% at low temperature, i.e. of the same typical order of magnitude as the one observed in dilute nitrides. We have determined the optimum implantation conditions for the most efficient SDR by the systematic analysis of different ion doses spanning four orders of magnitude. Moreover, we have also evidenced the influence of a weak external magnetic field on the SDR efficacy.

The material spin filtering properties are considerably enhanced thanks to the decoupling of the electron and nuclear spins in the paramagnetic centres under weak external magnetic field.

This puts forward the use of ion implanted GaAs-based material as a model system for robust and long-lived spin memories in the form of nuclear spin polarization. This demonstration, relying on the post-growth creation of Ga interstitial defects, could be transferred to other Ga-based compounds allowing for the independent adjustment of PL wavelength and SDR efficiency. The possibility of producing SDR active regions with arbitrary patterns by adjusting the implantation conditions could offer another degree of freedom for the design of possible spintronic devices relying on the spin filtering properties of deep paramagnetic defects, such as e.g. spin repeaters, or implanted layers for increasing the efficiency of the injection in spin LED devices.

Résumé de la thèse en français

Une thèse de doctorat de l'INSA rédigée en anglais doit comporter un résumé détaillé en français ; celui-ci est présenté ci-dessous. Le lecteur pourra se référer aux figures et références présentées dans les différents chapitres du manuscrit.

Introduction

L'utilisation du spin à la place de la charge dans les semiconducteurs est à la base de nombreuses propositions de recherche visant à réaliser de nouveaux dispositifs mariant les possibilités technologiques de la micro- et nano-électronique aux améliorations potentielles qui seraient apportées par la spintronique, comme une augmentation de la vitesse de manipulation des données et une diminution de la consommation électrique. Même si une utilisation pratique de dispositifs semiconducteurs basés sur l'électronique de spin est encore lointaine, les possibilités offertes en terme d'ingénierie de bande et de contrôle de la conductivité confèrent aux matériaux semiconducteurs un rôle clef dans le domaine de la spintronique.
Malgré les progrès rapides et importants dans le domaine, plusieurs verrous fondamentaux et technologiques doivent être encore surmontés. Par exemple, le stockage et la manipulation sous la forme d'un spin nécessitent que ce dernier puisse être conservé pendant un temps suffisamment long, et préférablement à température ambiante. L'injection, le transport et le filtrage de spin ont encore à l'heure actuelle une efficacité limitée et fonctionnent principalement à basse température ou sous champ magnétique.
Différentes approches ont été développées et proposées par la communauté scientifique pour aborder ces problèmes. Parmi les plus efficaces citons: (i) le confinement des porteurs dans les trois directions de l'espace dans des objets de taille nanométrique tels que les boîtes quantiques (In)GaAs, CdTe, ou plus récemment dans les matériaux à grand gap tel que GaN, ce dernier permettant le maintien d'une polarisation de spin stable à température ambiante. (ii) La deuxième approche repose plutôt sur l'ingénierie des défauts dans les semi-conducteurs: donneurs, accepteurs ou encore centres paramagnétiques profonds. Les atomes de phosphore dans

le silicium, le centres N-V dans le diamant ou encore le gallium interstitiel dans les nitrures dilués ne sont que quelques exemples. Dans cette seconde approche, l'adressage d'un ensemble d'états de spin est d'ailleurs possible du fait de l'identité physique de chacun des défauts, ce qui simplifie grandement la tâche expérimentale.
Ce travail représente une contribution à ces deux approches. D'un côté, grâce aux progrès récents dans la croissance de nano-structures à grand gap à base de GaN et aux résultats prometteurs obtenus dans ces composés dans les travaux précédents du groupe, nous avons étudié les propriétés de spin dans des boîtes quantiques GaN/AlN insérées dans des nanofils de GaN. Ce travail a été mené en collaboration avec l'équipe INAC/SP2M du CEA et en particuliuer avec B. Gayral et J. Renard. De l'autre côté, en s'inspirant des exceptionnelles propriétés de filtrage de spin des centres paramagnétiques dans les nitrures dilués, nous proposons ici un prototype de filtre de spin basé sur l'implantation de centres paramagnétiques dans des couches massives de InGaAs. Le but de ce travail a été le développement d'un procédé de création de ces défauts qui puisse surmonter les inconvénients inhérents à l'insertion d'azote dans les semiconducteurs de type GaAs : a) la dépendance de l'efficacité du filtrage de spin avec de l'énergie de photoluminescence, b) l'impossibilité de créer des zones actives avec des motifs spécifiques. Cette partie de mon travail de thèse a été possible notamment grâce à la collaboration avec J.C. Harmand, E. Galopin, J. Gierak, E. Bourhis du LPN à Marcoussis.
Ce travail de thèse s'inscrit dans la continuité des travaux précédents menés dans le groupe. Les premiers résultats sur l'alignement optique du spin de l'exciton dans les matériaux à grand gap avaient été obtenus par D. Lagarde sur des boîtes quantiques GaN/AlN auto-organisées en phase cubique. Pendant cette thèse, la stabilité temporelle de la polarisation linéaire de la photoluminescence sous excitation quasi-résonante avait été mise en évidence jusqu'à température ambiante, malgré une décroissance sensible de son amplitude avec la température. Certaines questions restaient toutefois ouvertes:

(i) l'orientation de spin n'est-elle possible que dans des structures cubiques, donc sans champ piézo-électrique ?

(ii) Quelle est l'influence de la haute densité de défauts due à la structure cubique, phase non stable, dans les nitrures?

(iii) Quelle est l'influence de l'orientation cristallographique sur l'alignement optique des excitons dans les structures wurtzite?

L'étude des propriétés de spin dans les nitrures dilués a été le sujet de deux précédents travaux dans notre groupe. Dans un premier temps, grâce aux travaux réalisé en collaboration avec Vladimir Kalevich de l'Institut Ioffe de St-Petersbourg (Russie), les propriétés de spin surprenantes de GaAsN ont été interprétées par un effet spectaculaire de Recombinaison Dépendante du Spin (SDR) des électrons de conduction sur des centres paramagnétiques apparus dans le matériau du fait de l'introduction de l'azote. Notons que cet effet de SDR a été découvert et interprété il y plus de 30 ans à l'Ecole Polytechnique de Paris par J. Lepine dans le Silicium, C. Weisbuch et G. Lampel dans AlGaAs et D. Paget dans GaAs. Ces résultats préliminaires sur la recombinaison dépendante du spin dans GaAsN ont été présentés dans le chapitre III de la thèse de L. Lombez. Dans un deuxième temps, grâce à une collaboration avec W. Chen de l'université de Linköping, F. Zhao avait, entre autre, mis en évidence la nature des centres paramagnétiques: il s'agit en effet de défauts liés à la présence de gallium interstitiel plutôt qu'à l'azote lui-même qui sont à l'origine de la recombinaison dépendante du spin. De même, certaines questions méritaient d'être approfondies, notamment:

- (i) Peut-on créer un centre paramagnétique sans recours à l'utilisation de l'azote?
- (ii) Dans ce cas, les effets de recombinaison dépendants du spin sont-ils comparables aux résultats dans les nitrures dilués?
- (iii) Peut-on définir sélectivement avec une bonne résolution spatiale des zones actives en SDR?

Mon travail de thèse résumé brièvement ci-dessous a permis d'apporter des éléments de réponse à ces différents points.

Chapitre I

Introduction aux propriétés électroniques et optiques des structures semiconductrices

Nous présentons dans ce premier chapitre une introduction à la physique des structures semiconductrices de differentes dimensionalités (massif, puits et boîtes quantiques). Nous mettrons en avant les particularités des structures III-V. Nous discuterons dans la première partie de ce chapitre de la structure électronique au centre de la zone de Brillouin de ces systèmes dans les cas où les semiconducteurs cristallisent dans la phase blende de zinc ou wurtzite. Nous présentons brièvement les propriétés électroniques des semiconducteurs massifs, des puits quantiques et des boîtes quantiques auto-organisées. Nous décrivons également les propriétés de base des excitons (paire électron-trou en interaction coulombienne) qui, dans le cas de GaN, jouent un rôle fondamental dans l'interprétation des expériences, même à température ambiante. Nous détaillons ensuite le principe du pompage optique orienté qui découle de l'interaction de ces systèmes avec une onde électromagnétique. Nous verrons que les règles de sélection optique vont permettre de relier la polarisation de la lumière à la polarisation en spin des porteurs photogénérés. Ceci constitue le point de départ des expériences de spectroscopie optique qui seront présentées dans ce manuscrit. Enfin, nous évoquerons les principaux mécanismes de relaxation de spin dans les structures semiconductrices.

Chapitre II

Équipements expérimentaux

Pour les études de spectroscopie de photoluminescence présentées dans ce mémoire, nous avons utilisé une chaîne constituée d'un laser solide Vanadate:Nd^{3+} doublé en fréquence (intracavité) qui sert de pompe à un oscillateur Titane-Saphir (Ti:Sa) impulsionnel.

Le laser Titane-Saphir à modes bloqués

Ce laser est un oscillateur Titane-Saphir impulsionnel dont le milieu amplificateur solide est un cristal de saphir dopé au titane (Al_2O_3 :Ti). Nous pouvons l'accorder en longueur d'onde sur un domaine spectral allant de 680 nm jusqu'à 990 nm en mode impulsionnel et nous pouvons le faire fonctionner dans deux configurations différentes qui génèrent des impulsions limitées par transformée de Fourier respectivement picosecondes ($\approx$ 1.5 ps) et sub-picosecondes ($\approx$ 100 fs). Au cours de ma thèse, seul le mode picoseconde a été utilisé. Ce laser peut également être utilisé en mode continu (cw). En régime impulsionnel, ce laser est un laser à modes bloqués (mode-locking en anglais) qui utilise l'auto-modulation de phase et l'effet Kerr dans le cristal de saphir dopé au titane. Afin d'obtenir des impulsions courtes récurrentes, les modes longitudinaux de la cavité du Ti :Sa sont synchronisées. La synchronisation est elle-même obtenue par l'effet Kerr optique dans le cristal de Saphir dopé au titane. Afin de compenser la dispersion de la vitesse de groupe, étape nécessaire pour obtenir des impulsions, le laser utilise en mode picoseconde un interféromètre de Gires-Tournois. La fréquence de répétition du laser Ti :Sa est de 80 Mhz et sa puissance moyenne suivant la longueur d'onde varie dans la gamme 0,4-2 Watts (ce qui correspond à une énergie par impulsion de 5 à 25 nJ).

Le doubleur-tripleur de fréquence

L'excitation des transitions optiques inter-bandes dans les semiconducteurs à grande énergie de bande interdite de type GaN requiert l'utilisation de sources d'excitation dont la longueur d'onde se trouve dans l'UV proche, c'est-à-dire entre 280 nm et 380 nm. De plus, l'accordabilité en longueur d'onde de ces sources est un point clé pour nos expériences de pompage optique orienté. C'est pourquoi nous avons utilisé les propriétés des cristaux de LBO et de BBO dont les susceptibilités non linéaires du second ordre importantes permettent de doubler ou tripler la fréquence du faisceau issu du laser Ti :Sa. Ainsi, nous pouvons obtenir des impulsions laser dont la longueur d'onde est accordable dans les gammes détaillées dans le Tableau 2.2. Notre dispositif de doublage/triplage de fréquence est le système commercial GWU-FHG Flexible Harmonic Generator de la société Spectra Physics dont le fonctionnement est schématisé sur la Figure 2.4.

Spectroscopie de Photoluminescence résolue en temps

Le dispositif expérimental d'étude de photoluminescence résolue en temps exposé dans cette thèse se base sur une caméra à balayage de fente ("streak camera" en anglais) fonctionnant en mode synchronisé, à photocathode S1 refroidie (Hamamatsu C5680) pour les expériences dans l'infrarouge, et à photocathode S20 pour les expériences dans l'ultraviolet. Le principe du dispositif expérimental est très simple : l'échantillon est excité par des impulsions issues du laser Ti:Sa, et le signal de photoluminescence est dispersé dans un monochromateur puis envoyé dans la caméra à balayage de fente. La lumière à analyser entre par la fente de la caméra et arrive sur une photocathode, générant ainsi un flux d'électrons qui va être ensuite accéléré par un champ électrique dans un tube sous vide. Dans ce tube, les électrons sont déviés par une paire d'électrodes à laquelle est appliquée une tension sinusoïdale calée en phase par rapport au laser Ti :Sa (une photodiode rapide détectant les impulsions périodiques du laser Ti :Sa est employée à cet usage). Les électrons arrivent ensuite sur une galette à micro-canaux où leur nombre est multiplié avant de frapper un écran de phosphore. L'image de l'écran de phosphore est collectée et intégrée par une caméra CCD. Les images collectées sont corrigées par le bruit de la photocathode, par sa sensibilité et dans le domaine temporel. La caméra étant précédée par un monochromateur qui disperse la lumière horizontalement, les images obtenues sont donc en deux dimensions : horizontalement nous avons la dépendance de l'intensité de la photoluminescence en fonction de la longueur d'onde et verticalement sa dépendance en fonction du temps. Un code des couleurs représente l'intensité de la photoluminescence.

Mesures de la polarisation

Afin de connaître les dynamiques de spin des porteurs dans nos structures, nous utilisons la polarisation de la lumière. Dans un premier temps, il faut pouvoir faire varier la polarisation de la lumière excitatrice. Pour cela, nous disposons d'un compensateur de Soleil-Babinet. Ensuite, pour étudier la polarisation de la photoluminescence, nous disposons de lames demi onde et quart d'onde pour détecter respectivement les composantes de polarisation linéaires et circulaires du signal. L'orientation des axes de ces lames permet de transformer la composante de la photoluminescence en lumière de polarisation linéaire horizontale. Dans le dispositif expérimental de la caméra à balayage de fente, nous utilisons un cube polariseur placé après les lames biréfringentes sur le trajet du faisceau optique. Les taux de polarisation circulaire et linéaire se définissent ainsi :

$$P_c = \frac{I^+ - I^-}{I^+ + I^-}$$

et

$$P_c = \frac{I^X - I^Y}{I^X + I^Y}$$

avec I^+, I^-, I^X, I^Y les intensités des deux composantes de la lumière polarisées circulairement et linéairement, respectivement.

PL stationnaire et champs magnétiques

Afin de mettre en évidence certaines des caractéristiques spécifiques de la recombinaison dépendante du spin dans nitrures dilués, il n'est pas nécessaire de résoudre en temps la PL. Une photodiode silicium (Thorlabs FDS1010) couplée à un filtre spectral remplace le système composé par le monochromateur et la caméra à balayage de fente. Afin d'améliorer la sensibilité du système une technique d'amplification à détection synchrone a été utilisée.

Certaines de ces mesures ont été effectuées sous champ magnétique de faible intensité (<500 mT) en géométrie Faraday (direction du champ magnétique parallèle aux spin des porteurs photogénérés. Un aimant permanent (650 mT) placé derrière l'échantillon a été utilisé pour fournir le champ nécessaire en ajustant la distance aimant-échantillon.

Chapitre III

Dynamique de spin des nanostructures de GaN insérées dans des nanofils

Nous résumons ici les résultats de spectroscopie de photoluminescence présentés dans le chapitre 3 de ce manuscrit.

Depuis une décennie, les semiconducteurs à base de GaN sont considérées comme des matériaux prometteurs pour de possibles applications à la spintronique en raison de leur couplage spin-orbite faible, de la grande énergie de liaison de l'exciton et de la possibilité de réaliser des nanostructures. Des démonstrations de leur fort potentiel, notamment le blocage de la relaxation de la polarisation en spin de l'exciton pendant sa durée de vie radiative dans de nanostructures auto-assemblées de GaN/AlN cubiques et InGaN/GaN wurtzites, ont été réalisés dans notre groupe et décrite dans la thèse de D. Lagarde, soutenue au LPCNO. En dépit de ces manifestations, la forte densité de défauts et de dislocations, en raison du manque de substrats appropriés, affectent encore la croissance de ces matériaux qui entravent leurs propriétés optiques et de spin lorsque la température augmente. Récemment, les succès obtenus dans la réalisation des boîtes quantiques de GaN/AlN insérées dans des nanofils de GaN ont fourni une alternative valable aux nanostructures auto-assemblées permettant l'étude des propriétés de spin des excitons dans un nouveau système avec moins de dislocations et autres défauts proches de l'emplacement de la boîte quantique. Les meilleures propriétés optiques et les caractéristiques de polarisation des excitons améliorées prévues pour ce système ont été les principales motivations de ce travail. Grâce à une collaboration avec B. Gayral du CEA/Institut Néel à Grenoble, nous avons étudié dans ce travail des nanostructure AIN/GaN insérées dans des nanofils fabriqués par épitaxie par jets moléculaire assistée par plasma sans catalyseur. Cette technique exploite une coïncidence dans les paramètres de maille entre le silicium (111) et le GaN wurtzite qui favorise, dans des conditions riches en azote, la croissance de nanofils avec l'axe $\vec{c}$ perpendiculaire au substrat. Cette orientation des nanofils est le point crucial qui rend possible la polarisation en spin des porteurs dans des structures.

Relaxation de spin dans GaN

Plusieurs travaux expérimentaux dans des couches de GaN massif dopées ont désormais montré que la relaxation de spin de l'électron peut effectivement atteindre des valeurs de quelques dizaines de nanosecondes, en accord avec les travaux théoriques de Krishnamurthy. Ces travaux on été menés aussi bien dans des structures wurtzite que blende de zinc. Différentes équipes ont cependant mis en évidence l'influence de la symétrie wurtzite sur la relaxation du spin de l'électron. Cette symétrie est en effet à l'origine de termes de relaxation supplémentaires de type Rashba par rapport à la symmetrie blende de zinc. Le rôle de la grande densité de défauts a été aussi indiqué comme être à l'origine des mécanismes de relaxation de spin de l'électron de type Elliot-Yafet. Quant à l'exciton, la communauté scientifique s'accorde sur une relaxation de spin extrêmement rapide (typiquement de l'ordre ou inférieure à la picoseconde) à cause de la forte interaction d'échange électron-trou. Ce scénario est toutefois radicalement changé dans les nanostructures. Dans les travaux de thèse de Delphine Lagarde, une polarisation en spin de l'exciton, stable sur quelques dizaines de nanosecondes, avait été mesurée jusqu'à température ambiante pour des nanostrucutres GaN/AlN blende de zinc et InGaN/GaN wurtzite sous excitation quasi resonante. Néanmoins, une diminution de l'amplitude de la polarisation de l'exciton en fonction de la température a été observée. Ces processus de relaxation, activés thermiquement, sont observés aussi bien dans les systèmes wurtzite que blende de zinc.

Dans ce travail, nous avons étudié un échantillon constitué d'un ensemble de boîtes quantiques de GaN/AlN insérées dans des nanofils de 40 nm de diamètre et de densité $10^{10}\mathrm{cm}^{-2}$, contenant environs 10 boîtes quantiques de 1 à 2 nm d'épaisseur. Afin d'étudier la dynamique de spin des excitons, nous avons excité l'échantillon avec des impulsions polarisées linéairement, de façon quasi-résonante. Cela signifie que les énergies d'excitation et de détection sont fixées dans la plage d'émission spectrale de l'ensemble des boîtes quantiques. Nous avons choisi une excitation polarisée linéairement car, comme décrit dans le chapitre 2, une réduction de la symétrie dans les nanostructures se manifeste par une anisotropie de l'interaction d'échange électron-trou dans le plan perpendiculaire à l'axe de croissance. Dans les boîtes quantiques, cette anisotropie induit un mélange des états excitoniques brillants circulaires pour produire deux nouveaux états à symétrie linéaire et séparés par une énergie appelée Δ_1.

Dépendance spectrale

Nous avons d'abord mis en evidence la presence d'une polarisation linaire de la photoluminesncece sous une excitation linaire quasi-résonante. Nous notons que la PL est toujours polarisée linéairement parallèlement à l'axe de polarisation de l'excitation et ce pour toute énergie de détection. Cependant, nous observons que le degré de polarisation diminue lorsqu'on s'éloigne de l'excitation. Pour une excitation laser d'énergie supérieure à 450 meV au-dessus de la détection, aucune polarisation n'est observée. Aucun degré de polarisation linéaire est mesurée le long de deux axes orthogonaux tournés de 45° par rapport à la direction de polarisation de l'excitation, suggérant l'existence d'états excitoniques orthogonaux. Cette affirmation est confirmée par l'absence de toute polarisation de la photoluminescence soit linéaire soit circulaire après une excitation circulaire. De ces observations expérimentales, nous pouvons conclure que: (i) Un degré de polarisation linéaire ne peut être mesuré que sous une excitation linéaire quasi-résonnante parallèle à l'axe de détection. (ii) Aucun degré de polarisation linéaire ou circulaire n'est mesuré après une excitation polarisée circulairement. Cela prouve que le degré de polarisation linéaire n'est pas dû au mélange de bandes excitoniques comme observé sur certains nano-structures à base d'InGaN. Dans ce cas, un degré de polarisation linéaire doit être mesuré pour toute polarisation ou pour toute énergie d'excitation . (iii) La dépendance spectrale du degré de polarisation linéaire est en accord avec les mesures précédemment effectuées sur les nano-structures GaN auto-assemblées. Cependant, le degré de polarisation linéaire ne semble pas être modifié avec la température, à différence de ce qui est observé dans les nano-structures auto-assemblées pour lesquelles le degré de polarisation linéaire de la photoluminescence diminue d'environ 50% entre 10K et la température ambiante. D'après les observations précédentes, nous pouvons affirmer que la polarisation linéaire de la PL est compatible avec l'alignement optique d'états excitoniques orthogonaux.

Dépendance angulaire

Les résultats précédents effectués sur des nano-structures blende de zinc ou wurtzite ont révélés des directions privilégiées pour l'orientation des états propres excitoniques linéaires (orientations respectivement le long de [110]/[$1\bar{1}0$] et [$1\bar{1}00$]/[$11\bar{2}0$]). Afin d'identifier de possibles orientations préférentielles et de vérifier l'orthogonalité des états excitoniques, nous avons procédé à deux types d'expériences, décrites ci-dessous:

Expérience A

Dans cette expérience, nous mesurons le degré de polarisation linéaire de la PL le long de deux axes orthogonaux, l'orientation étant maintenue parallèle à l'un d'entre eux, en fonction de l'angle de rotation de la polarisation d'excitation. Une PL co-polarisée avec l'excitation est mesurée pour toute angle de rotation. Ce comportement angulaire est compatible avec l'existence de différentes familles de boîtes quantiques de nanofils caractérisées par des états excitoniques orthogonaux à symetrie ”linéaire”. Ce point constitue une différence supplémentaire par rapport aux nano-structures auto-assemblées. L’origine de la distribution angulaire des états propres de l’exciton n’est pas encore claire. L’analyse aux rayons X réalisée sur des échantillons similaires a révélé la même orientation cristallographique pour les nanofils correspondant à une coïncidence dans le plan entre la maille du GaN et Si (111). Par conséquent, soit une asymétrie dans le plan due par exemple aux facettes hexagonales imparfaites, soit les fluctuations dues à des rugosités aux interfaces GaN/AIN sont probablement à l’origine de l’orientation aléatoire des états propres de l’exciton, plutôt qu’une orientation cristallographique aléatoire des nanofils.

Expérience B

Dans cette expérience, nous avons fixé la direction de la polarisation linéaire de l’excitation et nous avons mesuré le degré de polarisation linéaire de la PL selon deux axes orthogonaux dont le premier fait un angle α variable avec l’excitation. En accord avec la prédiction d’états linéaires et orthogonaux des excitons, le degré de polarisation linéaire détecté dans cette expérience est distribué de façon anti-symetrique par rapport à α=45°.

Afin de rendre compte des observations expérimentales, nous avons développé un modèle théorique basé sur la matrice densité dans l’hypothèse d’états excitoniques linéaires et orthogonaux. Le bon accord trouvé entre expérience et théorie a nous permis de valider notre modèle et de déterminer la classe de symétrie des états propres excitoniques compatibles avec les observations.

Etude de la dynamique de la polarisation

Nous avons enfin étudié la dynamique de polarisation en fonction de la température. Comme le degré de polarisation linéaire de la PL dépend la séparation entre excitation et détection, nous avons gardé cette valeur constante, tout en faisant varier l’énergie d’excitation selon la loi de Varshni afin d’observer toujours la même famille de boîtes. Un blocage de la relaxation de spin est observé à toute température et le degré de polarisation de la PL reste sensiblement constant jusqu’à température ambiante. Nous pouvons conclure que dans ce système nous n’observons ni une dépendance temporelle ni en température du degré de la polarisation en spin de l’exciton. L’origine de cette robustesse n’est pas encore bien expliquée. Nous avons attribué provisoirement l’origine de cette stabilité en température à la qualité structurelle supérieure des nanofils par rapport à celles des nano-structures auto-assemblées.

Chapitre IV

Recombinaisone dépendant du spin dans InGaAs implanté

Nous résumons ici les résultats de spectroscopie de photoluminescence présentés dans le chapitre 4 de ce manuscrit.

La recombinaison dépendante du spin (*Spin Dependent Recombination*, SDR en anglais) sur des centres paramagnétiques dans les semiconducteurs est connue depuis plus de 40 ans dans différents matériaux. C'est toutefois dans les nitrures dilués de type GaAsN que la SDR se manifeste avec des valeurs record, même à température ambiante, dans des expériences de photoluminescence aussi bien que de photoconductivité. La découverte, par spectroscopie ODMR, de la nature du centre paramagnétique à l'origine de la SDR dans GaAsN, à savoir le défaut gallium interstitiel et non pas l'azote, a ouvert des possibilités de conception de nouveaux dispositifs basés sur l'effet SDR sans introduction d'azote, souvent à l'origine de plusieurs défauts non-radiatifs. Dans ce chapitre, nous proposons une nouvelle méthodologie basée sur l'implantation d'ions de gallium afin de créer des centres profonds paramagnétiques dans les semiconducteurs avec une résolution spatiale, et ce sans insertion d'azote afin de pouvoir surmonter la limitation de l'approche des nitrures dilués.

Mécanisme et mise en évidence de la Recombinaison Dépendante du Spin

Le mécanisme de récombinaison dépendante du spin (SDR) trouve son origine dans le principe d'exclusion de Pauli. Le point clé est l'existence, dans la bande interdite du semiconducteur, de centres profonds paramagnétiques, c'est à dire centres possédant, à l'équilibre thermodynamique, un seul électron avec une orientation de spin quelconque. Le modèle théorique de la SDR a été initialement développé par Weisbuch et Lampel dans GaAlAs. Il peut être représenté schématiquement comme dans la figure 4.1 et expliqué simplement comme suit :

(i) On suppose d'abord que l'on excite des électrons de la bande de valence vers la bande de conduction par une lumière polarisée circulairement (figure 4.1a).

On suppose par simplicité que l'excitation crée 100 % de polarisation en spin dans la bande de conducion (BC).

(ii) En raison du principe d'exclusion de Pauli, la capture d'électrons de la BC sur les centres dépend de l'orientation du spin des électrons par rapport à celle des électrons résidents dans le centre paramagnetique: si les spins sont parallèles, la capture est interdite (on suppose généralement que les niveaux triplets ne sont pas liés). Au contraire, si leurs spin sont anti-parallèles, la capture pour former un singulet est très efficace, typiquement de l'ordre de quelques picosecondes. Le processus de capture d'électrons dépend donc de leurs spins.

(iii) Après la capture, les centres paramagnétiques peuvent recombiner un des électrons du singulet avec un trou de la bande de valence, ce dernier étant non polarisé (le temps de relaxation de spin trou est très rapide, de l'ordre de 1 ps). Cette recombinaison est donc indépendante du spin et laisse le centre à nouveau avec un seul électron.

(iv) Comme la capture d'électrons libres sur les centres est dépendante du spin et que la recombinaison des électrons piégés avec un trou est indépendante du spin, les électrons des centres vont progressivement se polariser en spin après quelques cycles d'excitation/recombinaison. Nous sommes en présence d'une situation de polarisation dynamique des centres paramagnétiques; le spin des électrons de ces centres est co-polarisé avec celui des électrons photogénérés (figure 4.1c).

Une manifestation spectaculaire de la Recombinaison Dépendante du Spin est obtenue en réalisant une expérience simple de spectroscopie de photoluminescence stationnaire en excitant l'échantillon avec de la lumière polarisée circulairement (σ^+) ou linéairement (σ^X), les autres paramètres de l'expérience restant strictement identiques (longueur d'onde d'excitation du laser, puissance d'excitation, etc...). Nous observons alors que l'intensité de la photoluminescence est supérieure pour une excitation circulaire comparée à celle mesurée pour une excitation linéaire. Pour quantifier ce rapport, on introduit le coefficient SDR qui est simplement donné par : $SDR = I^+/I^X$ où I^+ est l'intensité totale de photoluminescence après une excitation polarisée circulairement et I^X l'intensité totale de photoluminescence après une excitation polarisée linéairement. Des rapport R pouvant atteindre 200% à T=300 K dans un échantillon de $\mathrm{GaAs}_{1-y}\mathrm{N}_y$ avec une fraction d'azote y=0.021 ont été mesurés dans notre groupe (figure 4.2a). Après une excitation polarisée circulairement, les centres paramagnétiques vont se polariser de manière dynamique et aucune capture d'électrons par les centres ne sera plus possible (puisqu'ils ont le même spin) ; ces électrons vont alors recombiner de manière radiative avec les trous photogénérés. Par contre, après une excitation polarisée linéairement (photogénération de la même densité d'électrons de spin +1/2 que d'électrons de spin -1/2), les centres paramagnétiques vont rester non polarisés et donc la capture sur ces centres va être plus favorable que la recombinaison radiative. Ceci explique que lorsque l'on détecte la transition interbande (Bande de Conduction – Bande de Valence), l'intensité de la photoluminescence est plus forte pour une excitation polarisée circulairement que pour une excitation polarisée linéairement. Le fait que l'on observe ces effets pour des températures variant de 10 à 300 K montrent que ces centres paramagnétiques sont profonds. Ces effets sont également mis en évidence par une expérience de photoluminescence résolue en temps (figure 4.2b). Comme attendu, le déclin de la PL sous excitation circulaire est sensiblement plus long par rapport à celui attendu sous excitation linéaire. En effet, dans ce dernier cas, le temps de déclin de la PL est dominé par la capture sur les centres paramagnétiques. Cette capture est en revanche fortement limitée grâce au phénomène de polarisation dynamique des centres paramagnétiques sous excitation circulaire.

La SDR est aussi à l'origine du mécanisme de filtrage de spin dynamique des électron de la bande de conduction. En effet, en initialisant le système avec une lumière caractérisée par une polarisation circulaire, et une fois la polarisation dynamique du spin des centres obtenue, tout electron ayant subi un retournement de spin, sera rapidement capturé par le centre. On observe donc un temps "apparent" de relaxation de spin de l'électron dans la bande de conduction qui devient bien supérieur au temps de déclin de la photoluminescence (figure 4.3). La SDR a une dépendance importante de la puissance d'excitation (figure 4.4). A très faible puissance d'excitation, nous mesurons R≈100 % (pas d'effet SDR) comme attendu. En effet, si la densité d'électrons photogénérés polarisés en spin est très faible devant la densité de centres paramagnétiques, la polarisation dynamique des centres ne se produit pas de façon appréciable. Pour un échantillon avec y=2.1% d'azote, un optimum d'effet SDR est obtenu pour une puissance d'excitation de 30 mW, ce qui correspond typiquement à une densité de porteurs photogénérés de l'ordre de 10^{17} cm^{-3}. Ceci donne une estimation assez grossière de la densité des centres paramagnétiques. Lorsque la puissance d'excitation augmente davantage, nous avons observé une légère diminution du rapport SDR ; la modélisation de l'effet de recombinaison dépendante du spin montre que cet effet est lié au fait que les électrons photogénérés deviennent trop nombreux et que les canaux de recombinaison non-radiatifs sur des centres non paramagnétiques doivent être pris en compte.

Recombinaison dépendant du spin dans InGaAs implanté

Grâce à la connaissance de la nature des centres paramagnétiques par ODMR, à savoir les atomes interstitiels de Ga, comme presenté dans la thèse de F. Zhao dans notre groupe (figure 4.5), nous avons ici étudié la possibilité de créer, par implantation ionique d'atomes de gallium, des défauts interstitiels paramagnétiques dans une couche de InGaAs. Le but est double: d'une part il s'agit de démontrer la faisabilité en terme de SDR pour pouvoir s'affranchir de l'utilisation de l'azote, d'autre part nous voulons créer sélectivement des zones actives en SDR avec une importante résolution spatiale. Grâce à une collaboration avec J-C. Harmand et collaborateurs du LPN à Marcoussis, nous avons ainsi étudié un échantillon de $In_{0.09}Ga_{0.91}As$ de 50 nm d'épaisseur épitaxié sur une couche de GaAs. Une couche de protection finale de GaAs de 5 nm a été utilisée aussi pour préserver la couche d'InGaAs de l'air. Sept différentes doses d'atomes de gallium sur 4 ordres de grandeurs (voir tableau 4.1) ont été utilisées pour l'implantation afin d'étudier son effet sur l'efficacité de la SDR. Les différents paramètres d'implantation (énergie, distance pixel à pixel, temps de balayage) ont été choisis afin d'obtenir une implantation homogène sur des carrés de 200 μm de coté à une profondeur correspondant à la couche de InGaAs. Nous avons préalablement vérifié l'effet de l'implantation sur les propriétés optiques des échantillons. Nous avons observé une bonne intensité de luminescence sur tous les échantillons sauf pour les deux doses d'implantation les plus fortes, pour lesquelles les défauts non radiatifs induits ne permettent pas l'observation d'un signal de luminescence. Afin de s'assurer que l'implantation est efficace et bien obtenue seulement dans la couche de InGaAs, nous avons démontré les points suivants: (i) l'intensité de PL n'est affectée que dans la zone spectrale relative à InGaAs. En figure 4.7b nous montrons en effet que le temps de déclin dû au GaAs est pratiquement inchangé après implantation. Pour InGaAs, nous observons par contre une diminution qui reste toutefois bien mesurable. (ii) Nous avons aussi démontré que l'on obtient bien un effet SDR exclusivement dans les zones implantées (figure 4.8) et (iii) que l'effet SDR n'est présent que dans la région spectrale d'émission relative à l'InGaAs et non pas dans celle de GaAs. (iv) Nous constatons aussi que les valeurs de SDR obtenues sont tout à fait comparables à celles observées dans les nitrures dilués. Ces observations nous permettent d'affirmer que l'implantation ionique est un outil approprié pour produire des centres paramagnétiques dans InGaAs avec une résolution spatiale à la fois horizontale et verticale.

Nous avons aussi mesuré la dynamique de l'effet SDR. Cette mesure permet d'évaluer le temps necessaire à l'instauration de la polarisaiton dynamique en spin des centres paramagnetiques. La figure 4.9 montre qu'environ une trentaine de picosecondes sont suffisantes pour atteindre un taux SDR de 380% . Ce taux diminue ensuite à cause de la recombinaison des porteurs dans la bande de conduction, qui ne peuvent plus finalement assurer le maintien de la polarisation dynamique.

Dépendance de la dose d'implantation

Une question importante est de déterminer l'influence de la dose d'implantation sur l'efficacité de l'effet SDR. Pour cela, nous avons étudié une série de 7 zones avec des doses d'implantation variables sur 4 ordres de grandeur. Comme montré en figure 4.10, un maximum d'efficacité de l'effet SDR est obtenu pour une dose autour de $5{\cdot}10^9$cm^{-2}. A des doses plus faibles, l'implantation ionique crée un nombre de centres paramagnétiques insuffisants pour l'observation de l'effet. A des doses plus élevées, nous attribuons la diminution de la SDR à une augmentation de défauts non paramagnétiques qui entrent en compétition avec la recombinaison sur les centres paramagnétiques, ce qui entraîne la diminution de l'efficacité de l'effet SDR. Prenant en considération la densité optimale d'ions Ga déterminée ici et en supposant, pour simplifier, 100% d'efficacité de création de défauts paramagnétiques par implantation dans la couche d'InGaAs d'épaisseur de 50 nm, on peut estimer que la densité de centres paramagnétiques créés est de l'ordre de 10^{15} cm^{-3}, ce qui est en bon accord avec les travaux antérieurs sur les nitrures dilués.

Influence d'un champ magnétique longitudinal

Afin de renforcer la conclusion de la création de défauts paramagnétiques dans notre échantillon, nous avons étudié l'effet d'un champ magnétique externe en géométrie Faraday (champ magnétique parallèle à la direction de propagation de la lumière incidente) sur la SDR. Sur la figure 4.12, nous montrons les spectres de PL intégrés temporellement sous excitation circulaire et linéaire et le taux SDR respectifs sous l'influence d'un champ magnétique B_{ext} = 230 mT pour l'échantillon avec la dose d'implantation optimale. L'effet SDR augmente significativement de 140% à 220% . L'augmentation observée est entièrement due à une amélioration de l'intensité PL sous excitation circulaire: l'intensité PL sous une excitation polarisée linéairement reste inchangée. Cette observation suggère que le champ magnétique extérieur conduit à une l'amélioration du mécanisme de filtrage de spin. Par analogie avec des récentes observations par V. Kalevich *et al.* ainsi que de notre groupe et celles plus anciennes de D. Paget, nous interprétons cette amélioration comme due à l'écrantage de l'interaction hyperfine dans les centres paramagnétiques entre le spin de l'électron et le spin nucléaire par le champ magnétique.

Conclusions

Ce travail de thèse a porté sur l'étude de la dynamique de spin dans des structures semi-conductrices à base de GaN et InGaAs. La principale motivation a été l'identification de systèmes capables de maintenir en temps une très longue polarisation de spin des porteurs. Deux approches ont été étudiées ici : (i)le confinement quantique des porteurs dans des boîtes quantiques et (ii) l'ingénierie des défauts paramagnétiques.

Pour la première approche, nous avons étudié la polarisation de spin de l'exciton dans des boîtes quantiques GaN/AlN insérées dans de nanofils de GaN. Nous avons observé le blocage de la relaxation de spin de l'exciton et son insensibilité à la température. Nous avons également étudié la dépendance angulaire de la polarisation linéaire de la photoluminescence. Cette analyse révèle la présence de familles indépendantes de boîtes quantiques avec des états propres excitoniques orthogonaux . Nous avons enfin développé un modèle basé sur la matrice densité pour décrire les observations expérimentales montrant que la dépendance angulaire mesurée est compatible avec soit une distribution uniforme des dipôles des excitons, soit une répartition suivant une symétrie C_{3v} ou d'ordre supérieur. L'insensibilité de la relaxation de spin de l'exciton à la température nous permet de proposer ce système comme candidat plausible pour des applications en spintronique. Néanmoins, ces observations nécessitent certainement des approfondissements à la fois théoriques et expérimentaux.

Dans la deuxième partie de cette thèse, nous avons démontré que des régions actives en recombinaison dépendante du spin peuvent être créées de manière sélective dans des couches épitaxiées de InGaAs par implantation ionique d'ions Ga. Nous avons mis en évidence un taux de SDR important atteignant 240% à basse température, c'est à dire du même ordre de grandeur que celui typiquement observé dans les nitrures dilués. Nous avons déterminé les conditions d'implantation optimales pour maximiser le taux de SDR grâce à l'analyse systématique des zones implantées avec des doses ioniques sur quatre ordres de grandeur. Nous avons également mis en évidence l'influence d'un champ magnétique faible sur le taux de SDR. La propriété de filtrage de spin du matériau est considérablement améliorée grâce au découplage des spins nucléaires et électroniques dans les centres paramagnétiques par le champ externe. Cette technique de création de défauts paramagnétiques pourrait être transférée à d'autres systèmes permettant un ajustement indépendant de la longueur d'onde et de l'efficacité de l'effet SDR. La possibilité de produire des régions actives en SDR avec des motifs arbitraires en ajustant les conditions d'implantation, pourrait fournir un autre degré de liberté pour la conception de dispositifs spintroniques comme par exemple des répéteurs de spin, ou sous forme de couches pour accroître l'efficacité d'injection de spin dans des dispositifs spin-LED.